IMAGING THREE-DIMENSIONAL SINGLE MOLECULE DYNAMICS IN ITS CELLULAR CONTEXT

A Dissertation

by

DONGYOUNG KIM

Submitted to the Office of Graduate and Professional Studies of
Texas A&M University
in partial fulfillment of the requirements for the degree of

DOCTOR OF PHILOSOPHY

Chair of Committee,	Raimund J. Ober
Committee Members,	E. Sally Ward
	Andreea Trache
	Alvin T. Yeh
Head of Department,	Anthony Guiseppi-Elie

December 2016

Major Subject: Biomedical Engineering

ABSTRACT

Three-dimensional single molecule microscopy enables the study of dynamic processes in living cells at the level of individual molecules. Multifocal plane microscopy (MUM) is an example of such a modality and has been shown to be capable of capturing the rapid subcellular trafficking of single molecules in thick samples by simultaneously imaging distinct focal planes within the sample. Regardless of the specific modality, however, the obtained 3D trajectories of single molecules often do not fully reveal the biological significance of the observed dynamics. This is because the missing cellular context is often also needed in order to properly understand the events observed at the molecular level. We introduce the remote focusing-MUM (rMUM) modality, which enables 3D single molecule imaging with the simultaneous z-stack imaging of the surrounding cellular structures. Using rMUM, we demonstrate the 3D tracking of prostate-specific membrane antigen (PSMA) with a PSMA-specific antibody in a prostate cancer cell. PSMA is an important biomarker for prostate cancer cells. As such, it is a common target for antibody-based therapies. For example, of particular interest is the use of PSMA-specific antibodies that are conjugated with a toxin that kills prostate cancer cells. We analyze here the pathways of PSMA-specific antibodies, from prior to their first binding to PSMA at the plasma membrane to their arrival at, and continued movement in, sorting endosomes. By making possible the observation of single molecule dynamics within the relevant cellular context, rMUM allows, in our current application, the identification and analysis of different stages of the PSMA-specific antibody trafficking pathway.

DEDICATION

To my father and mother.

ACKNOWLEDGEMENTS

I am tremendously fortunate to have had the opportunity to work with Professors Raimund J. Ober and E. Sally Ward on the ideas in this dissertation. I would like to express my special appreciation to them for their precious advice and constant support and appreciate them for giving me the opportunity to work in their laboratory. I would also like to thank Professor Andreea Trache and Professor Alvin T. Yeh for serving as my committee members and giving me their heartfelt encouragement.

I am grateful to all former and current members of Drs. Raimund J. Ober and E. Sally Ward's laboratory. I would like to thank Dr. Sripad Ram for helping me to get started with microscopy and cell biology experiments. I especially appreciate his generous answers to my one hundred questions everyday. I would also like to acknowledge Dr. Jerry Chao and Anish V. Abraham for their valuable support on software and computer simulations. Special thanks to Drs. Siva Devanaboyina, Ed Cohen, Jayakumar Poovassery, Pankaj Bansal, Priyanka Khare, Ran Li, Zita Schneider, Dilip Challa and Rafal Swiercz for their collaboration. Special thanks also go to all my student colleagues, Sungyong You, Wooseok Kim, David Kim, Milad Rafiee Vahid, Jeffrey Kang, Sreevidhya Ramakrishnan and Ramraj Velmurugan, who have been a source of great support during my projects.

Finally, I must express my sincere gratitude to my family for providing me with unfailing support and continuous encouragement throughout years of study. This accomplishment would not have been possible without them. Thank you.

CONTRIBUTORS AND FUNDING SOURCES

Contributors

This work was supported by a dissertation committee consisting of Professors Raimund J. Ober, Andreea Trache and Alvin T. Yeh of the Department of Biomedical Engineering, and Professor E. Sally Ward of the Department of Molecular and Cellular Medicine and the Department of Microbial Pathogenesis and Immunology.

The analyses presented in Section 3 were performed in part by Sungyong You and Wooseok Kim of the Department of Biomedical Engineering. Antibodies used in Section 3 were provided by Dr. Siva Devanaboyina of the Department of Molecular and Cellular Medicine. Data analysis methods described in Section 2 were devised in part by Dr. Sripad Ram and Dr. Ed Cohen.

All other work conducted for the dissertation was completed independently by the student.

Funding Sources

The study was supported in parts by a grant by National Institutes of Health (NIH) to my advisor Professor Raimund J. Ober.

TABLE OF CONTENTS

Page

LIST OF FIGURES

FIGURE Page

1. INTRODUCTION

The optical microscope is a tool that examines specimens at high magnification. It has been a standard instrument in biological research. The microscope allows us to investigate many details of cellular structure and events that would not be possible to see with the human eye. The invention of the first optical microscope took place three centuries ago. Recent advances in technology development in many fields have reinvented the optical microscope. The development of glass, lens and coating technology reduces optical aberration as well as improves transmittance of the light significantly. The recent inventions of highly sensitive detectors such as photomultiplier tubes (PMT), charge-coupled devices (CCD), and scientific complementary metal-oxide semiconductors (sCMOS), light sources like light amplification by stimulated emission of radiation (LASER) and light-emitting diode (LED), and computer automation have revolutionized the capability and accessibility of the optical microscope. Furthermore, the development of fluorescence markers such as fluorescent proteins (FPs), organic dyes and quantum dots permits the observation of proteins in living cells, and furthermore, at the single molecule level [1, 2, 3].

The fluorescence microscopy technique is widely used for the study of cellular structures and trafficking. Here the specific targets in the sample are fluorescently labeled. In particular, such a labeling can be carried out by using a fusion construct of a fluorescent protein. The classical fluorescence microscopy requires detection often of hundreds of fluorescence protein molecules. Classical fluorescence detection This detection involves thousands of fluorescence protein molecules. Therefore, the detection represents the averaged fluorescence activities of the sample, and this may hide relevant biological information such as heterogeneity of protein interactions.

Single molecule microscopy removes the averaging effect by looking at the individual molecules; this allows for the study of fine details of molecular dynamics [4, 5, 6, 7].

1.1 Single molecule microscopy

Over the last two decades of developments, single molecule microscopy has become a superior technique for studying specimens at the nanoscale. The initial single molecule experiment was performed by Moerner *et al.* in the late 1980s [8]. Here, the energy absorption was measured in a solid. The next year, Orrit and Bernard measured fluorescence emission from a single molecule [9], followed by Betzig and Chichester who took the measurement at room temperature [10]. Along with this evolution, current single molecule experiments are carried out within biological specimens.

A single molecule microscopy experiment is typically performed by observing an individual "fluorescence molecule" that labels the biomolecule of interest. The fluorescence molecule is illuminated with a specific wavelength of light. The absorption of light induces the fluorescence activities, and the molecule emits photons with a longer wavelength than the illumination. The fluorescence molecule is selected for the single molecule experiment using the following considerations [11, 12]:

1. Brightness
2. Photostability
3. Absorption and emission wavelength
4. Toxicity, for live cell imaging experiments
5. Accessibility

The fluorescence molecule for a single molecule experiment should be bright, i.e., high quantum yield (QY) and high extinction coefficient (EC). Although there are approaches available to identify the single molecule at an extremely low signal-to-noise ratio (SNR) [13], it is always better to have a high SNR for the accurate detection of the single molecule [14, 15]. Photostability refers to the stable emission of photons of the fluorescence molecule without disruption. The molecule can lose its fluorescence activity, resulting in no emission of a photon; this is called "photobleaching." Absorption and emission wavelengths of the fluorescence molecule are another consideration. Biological specimens tend to absorb ultraviolet (UV) light and emit photons; this is called "autofluorescence." Autofluorescence contributes to the background signal, and the single molecule may not be detected due to the low SNR. Light, and in particular UV light can damage the living cell; this is called "phototoxicity." A fluorescence molecule with near-infrared (IR) absorption and emission may be considered to avoid both autofluorescence and phototoxicity problems. In live cell experiments, the fluorescence molecule as a biomarker must not be toxic to the biological specimen and should be readily available for coupling to the target molecule.

Four major types of fluorescence molecules are available for single molecule experiments: chemical dyes, organic dyes, fluorescence protein and nanoparticles (e.g., quantum dots, gold or silver nanoparticles, and polymers). Chemical or organic dyes are widely used for fluorescence microscopy. The single molecule super-resolution microscopy technique for fixed cells relies on these dye molecules. These dyes, however, are not recommended for single molecule tracking experiments within living cells, because they are typically dim and photobleach easily. Also, for many biological problems the dyes cannot label directly. The use of fluorescence proteins can overcome this issue by labeling proteins of interest in a highly specific manner. The green fluorescent protein (GFP) is isolated from the jellyfish *Aequorea victoria* [16]. GFP can be fused to the protein of interest using deoxyribonucleic acid (DNA) cloning techniques. This provides an excellent specific fluorescent label to the target molecule in living cells. Variant mutants of GFP are available; the first single molecule super-resolution microscopy experiment was carried out using photoactivatable-GFP (PA-GFP) [17]. Nanoparticles can be used as a fluorescence marker as well. A quantum dot (QD), for instance, is a tiny semiconducting particle that is bright and photostable (no photobleaching) with various emission selections [18, 19, 20]. A QD is about 1 to 5 nm in size, and the emission wavelength depends on its size, i.e., smaller QDs emits shorter wavelengths of light. QDs, however, is a semiconductor made of heavy metals like cadmium selenide (CdSe) and zinc sulfide (ZnS), which are toxic to living cells.

1.2 Techniques for single molecule imaging

Single molecule imaging has been demonstrated using many different microscope configurations. Examples include widefield, confocal and total internal reflection fluorescence microscopy.

Single molecule imaging with widefield microscopes needs to be carefully configured to have the highest possible SNR. High-sensitivity detectors such as cooled CCD, electron multiplier CCD (EMCCD) or sCMOS camera are required. Modern back-illuminated EMCCD cameras can detect and count single photons with 90% quantum efficiency (QE) and less than 1 electron effective read noise [21, 22]. The recent development of sCMOS also allows high sensitivity imaging with high frame rate and large field of view and has been demonstrated for single molecule imaging [23]. In addition to the detectors, the emission filter needs to be well optimized to have high SNR. The sample has to be prepared with clean and flat coverslips. Immersion medium and imaging medium should have very low autofluorescence.

Total internal reflection fluorescence microscopy (TIRFM) is a favorite among single molecule microscopy techniques and, in fact, the initial single molecule imaging experiments within living cells were carried out using TIRFM [24, 25, 26, 27]. TIRFM uses the total internal reflection of the excitation light, and this forms a thin layer of illumination right above the coverslip. Since the illumination is only taking place across a 200 nm thin volume, background from out of focus is dramatically reduced compared to the widefield microscope. This increases SNR significantly; therefore, TIRFM is capable of single molecule imaging. Also, TIRFM enables cellular membrane protein studies at the single molecule level.

The confocal microscope is also utilized for single molecule imaging. Confocal microscopy is achieved by illuminating the sample with focused light, which represents a diffraction-limited volume. The fluorescence signal from the small volume illumination is collected using a photomultiplier tube. A confocal microscopy image is obtained by moving the focused beam across the specimen. Confocal imaging can be time consuming, as the beam scans through the region of interest. However, the scanning rate can be pretty high, from kilohertz to megahertz. Using this rapid sampling rate with a sophisticated feedback system, single molecule imaging using the confocal microscope was demonstrated by circling the beam around a single molecule [28, 29]. This, however, is limited to imaging one or at the most a few single molecule at a time.

1.3 Challenges in single molecule microscopy

In the last two decades of developments in single molecule microscopy, single molecule imaging has been demonstrated with fixed and living cells. Here we discuss single molecule imaging specifically in living cells. The cell is a structural and functional biological unit of living organisms and has been studied extensively in cell biology. In particular, eukaryotic cells are organized with complex organelles with rapid metabolic activities, and their structural and functional mechanisms have not yet been fully understood. These cells form three dimensional (3D) structures and, therefore, their functional activities such as protein interactions occur in three dimensions as well. Single molecule microscopy offers optimal tools to study the individual molecular activities at the nanoscale. However, there are several technical issues. Single molecule microscopy has been mainly optimized for two-dimensional or shallow three-dimensional single molecule imaging. Also, while we are imaging the single molecule dynamics, no or only limited contextual information is available.

1.3.1 Three-dimensional single molecule imaging

Early single molecule microscopy techniques were mainly focused on two-dimensional single molecule imaging. The use of TIRFM, which illuminates samples in a thin layer above the coverslip, significantly improves the signal-to-noise ratio that is needed for single molecule imaging. Consequently, many single molecule studies have been performed using TIRFM systems. However, this permits single molecule imaging only at the cell membrane that is above the coverslip. There is a need for three-dimensional single molecule imaging techniques. Several three-dimensional single molecule microscopy techniques have been introduced. The confocal microscopy approach has been adapted to 3D single molecule detection [28, 29]. This is carried out by circling the confocal beam around the single molecule, using a complicated feedback system. Although the confocal approach has been successfully demonstrated for single molecule tracking, only a limited number of molecules (typically, one) can be tracked per imaging experiment. Besides, the feedback system is implemented by moving the specimen with an XYZ piezo stage, which may interfere with the single molecule dynamics. Engineered point spread function (PSF) has been used for 3D single molecule imaging with widefield microscopy configuration. Three-dimensional information is encoded into the shape of a defocused image. Astigmatic PSF [30, 31] and double-helix PSF [32, 33] exemplify such a modality. The problem of the PSF engineering approach is that axial coverage is highly limited, i.e., up to 3 µm, whereas the living cells are as thick as 10 µm. Multifocal plane microscopy (MUM) is an ideal solution [34, 35, 36]. MUM is a widefield microscopy modality that simultaneously images distinct focal planes within the cell sample. Three-dimensional single molecule imaging using MUM has been demonstrated with living cells that are 10 µm thick [35].

1.3.2 Single molecule and its context

One important goal of single molecule microscopy is to study single molecule dynamics and interactions with surrounding proteins and cellular structures. Multicolor single molecule imaging [37, 38, 39] and single molecule Förster resonance energy transfer (FRET) exemplify protein-protein interaction studies using single molecule microscopy [40, 41, 42]. FRET experiments were demonstrated using two-dimensional single molecule microscopy techniques, although some of the most important molecular interactions in living cells are in the three-dimensional space. In particular, cellular trafficking in living cells involves highly dynamic activities and interactions with organelles.

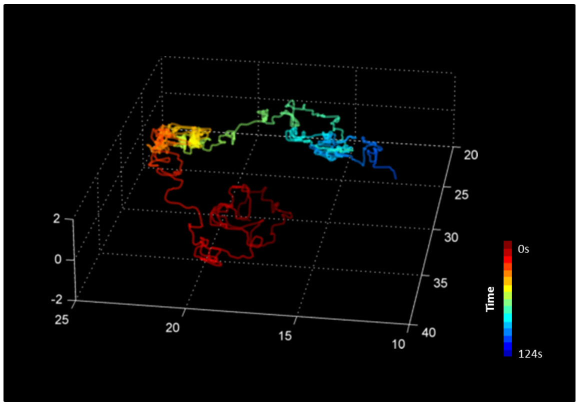

Figure 1.1: The 3D single molecule trajectory of a quantum dot labeled antibody in a live prostate cancer cell.

Figure 1.1 shows a 3D single molecule trajectory of a quantum dot labeled antibody in a live prostate cancer cell. The trajectory was acquired using the four-plane MUM setup. The trajectory is pseudo colored in time, i.e., red to blue as t=0 to 124 s. The antibody molecule moves around with complex diffusion dynamics in 3D. The trajectory is composed of complex diffusion dynamics; however, having only the single molecule trajectory without the context information of the cellular structure limits the understanding of its dynamics. For instance, when the single molecule suddenly changes its diffusive dynamics from directional motion to constrained motion, we cannot know where this antibody molecule is located such as in the plasma membrane or in endosomal compartments. The biological implication of such dynamics may change dramatically depending on which cellular structure the antibody molecule interacts with. Therefore, having 3D cellular structures with the 3D single molecule trajectory is necessary for understanding their dynamics properly.

1.4 Overview of the dissertation

Here we introduce a novel microscopy modality that carries out 3D single molecule tracking in thick cellular samples and, simultaneously, takes images of 3D cellular structures that are in the context of the single molecule dynamics. It includes the design and the construction of such a microscope system with the development of software packages to process and analyze the data.

The organization of the dissertation is as follows. Section 2 introduces remote-focusing multifocal plane microscopy (rMUM). rMUM is a multi-dimensional microscopic imaging approach that provides 3D single-molecule trajectories with the 3D cellular structures that the single molecule interacts with. Here, the detailed design and construction of the rMUM setup are described. rMUM essentially consists of two modules, the r- and the MUM-module. Single molecule images are obtained from the MUM-module, and three-dimensional locations of the molecules are estimated with high accuracy. Cellular structure images are acquired from the r-module. Those images from the r- and the MUM-module need to be spatially and temporally registered. Analysis of rMUM data is a major challenge. rMUM data analysis methods are developed to understand contextual molecular dynamics and are validated with simulations. The visualization approaches for rMUM data are discussed.

Section 3 discusses trafficking of prostate specific membrane antigens (PSMAs) in prostate cancer cells. The study is mainly carried out using the rMUM system developed in Section 2. PSMA is a specific prostate cancer cell marker. Although PSMA has been targeted for cancer treatment [43, 44], its mechanism of trafficking is little known, especially at the single molecule level. Here we reveal the detailed trafficking of PSMA in prostate cancer cells from the cell exterior to the lysosome. PSMA on the prostate cancer cell membrane undergoes endocytosis and is arranged in the sorting endosome. Depending on specific situations, PSMA is either recycled out or degraded in lysosomes. These processes can only properly be understood when both the single molecule and information of its surrounding cellular structure are available. Detailed interactions between PSMA and the cellular structures such as cell membrane, sorting endosomes and lysosomes are discussed.

2. REMOTE-FOCUSING MULTIFOCAL PLANE MICROSCOPY

2.1 Introduction

Cellular trafficking of proteins and receptors is a major focus of recent cell biology and oncology. This is fundamentally important to understanding biological phenomena of proteins and receptors as well as designing and evaluating therapeutics such as antibody-dependent cell-mediated cytotoxicity (ADCC) and antibody drug conjugates (ADCs) [45, 46, 47, 48]. Trafficking behavior at the single molecule level, however, is poorly understood due to the limitations of current microscopy techniques.

Single molecule microscopy is an ideal approach to understanding such cellular processes [12, 49, 50, 51]. Single molecule microscopy allows the observation of detailed molecular dynamics by avoiding the averaging effect of conventional microscopy. Current single molecule microscopy is primarily used to detect single molecules in two or three dimensions with very shallow depths [25, 24, 30, 31]. This is particularly related to the single molecule dynamics at the plasma membrane adjacent to the coverslip. Cellular processes, however, mostly occur in three dimensions. Therefore, the current single molecule microscopy techniques are not suitable to study such events. More importantly, the three–dimensional trajectory of the single molecule is only properly understood in the context of the cellular environment. The biological implications may change significantly depending on the cellular structures that the single molecule interacts with, such as the plasma membrane or sorting endosomes. Therefore, the development of a microscope system that is capable of imaging 3D single molecule dynamics with the cellular environment is desired. Such a microscope should satisfy the following criteria: first, rapid three-dimensional single molecule trajectories can be imaged and identified with the highest possible accuracy. Secondly, three–dimensional cellular structures that the single molecules interact with can be obtained.

Typically, three-dimensional microscopy data are acquired by z-stacking [52, 53]. Z-stack images are obtained by changing the focus position over time using a high numerical aperture objective lens. The focus change is carried out by adjusting either the objective lens or the sample position along the optical axis. In fact, z-stacking is generally used for imaging fixed cell specimen. When the temporal resolution becomes an important matter in imaging, e.g., in live cell imaging or single molecule imaging, z-stacking creates problems. The mechanical motion of the objective lens or the sample stage may introduce vibrations. In addition, highly dynamic objects such as single molecules may be impossible to image using z-stacking since we may be at the wrong focus position at the wrong time. There are alternative approaches that use sophisticated feedback systems to track single molecules in real time by changing the focus position as the target moves through 3D space. This method, however, only permits tracking of one or very few molecules at a time. Therefore, the problems still remain that (1) we may miss important dynamics since we only focus on one target at a time and (2) mechanical instability cannot be avoided since the position of the objective lens or the sample stage changes during the imaging experiment.

It would be ideal to image multiple 3D single molecule trajectories simultaneously. Multifocal plane microscopy (MUM) meets this requirement. MUM acquires 3D volume data by imaging multiple focal plane images simultaneously [54, 55, 56]. In this way, multiple molecules can be tracked by avoiding the wrong focus and wrong timing issues. Additionally, MUM allows the identification of a single molecule trajectory with high accuracy over thick cellular samples while the other techniques only support comparable accuracies over a shallow depth range [30].

Imaging 3D cellular structures using MUM is also possible, but it is certainly limited by the number of focal planes at which images can be obtained. For example, a MUM experiment can be configured with four focal planes that are 2 µm apart, i.e., planes could be located at 0, 2, 6 and 8 µm. This MUM setup acquires four images at the four focal planes simultaneously. The precise location of individual single molecules can be determined using a localization procedure in this setup since they are well-defined point sources. Cellular structures, however, cannot be properly visualized in such a setup. Cellular structures are densely labeled with fluorophores which cannot be resolved like individual point source. Structural data needs to be acquired by considering the Nyquist—Shannon sampling criterion in which the data needs to be sampled at half of the system resolution. This can be achieved by acquiring z-stack images.

Here we introduce a novel microscopy technique, remote-focusing multifocal plane microscopy (rMUM), that enables the imaging of single molecules in deep cellular samples at high temporal and spatial resolution as well as visualizing 3D cellular structures in the context of the single molecule dynamics. The microscope incorporates both the MUM and the remote focusing configuration. MUM identifies single molecule trajectories in 3D with high precision using the MUM localization algorithm [35, 34]. The three-dimensional cellular structures in the context of single molecule dynamics are obtained using a remote focusing technique [57, 58, 59, 60]. This technique acquires a series of z-stack images rapidly independent of the single molecule imaging.

This Section deals with the design of an rMUM setup and the development of software packages to process and analyze the acquired data. The organization of this section is as follows. Section 2.2 describes the construction and the implementation of the rMUM setup. The rMUM imaging experiment produces complex multi-dimensional data, and Section 2.3 explains the data processing approaches. Processed data then needs to be properly analyzed, and Section 2.4 discusses the data analysis techniques.

2.2 Remote focusing multifocal plane microscopy (rMUM)

To explain the principle of the rMUM setup, an example imaging experiment is introduced (Figure 2.1). We may study the dynamics, such as membrane diffusion, endocytosis and exocytosis, of antibody molecules in cancer cells. Such a study requires the visualization of single molecule dynamics in the context of the plasma membrane and endosomal compartments. The antibody molecules conjugated with quantum dots (QDs) can provide single molecule trajectories. Cellular structures labeled with green fluorescent proteins (GFPs) can be used via transfecting cells [61, 62]. The dynamics of antibody molecules labeled with QDs are highly mobile. The single molecule trajectories can be obtained using MUM at high spatial and temporal resolutions. A series of z-stack images of GFP—labeled cellular structures are obtained using the remote focusing configuration. Both single molecule and cellular structure images are acquired simultaneously by separating the emission light into different ranges of spectra, i.e., emission of QDs: 645 nm, emission of GFP: 520 nm, using dichroic filter sets.

Figure 2.1 explains the details of such imaging experiments. Assume we have a single molecule outside the cell. This molecule may enter the cell and interact with cellular structures such as the plasma membrane, sorting endosomes and lysosomes. Such events are only properly understood when both the single molecule dynamics and the cellular structure information are available in 3D. Therefore, the traces

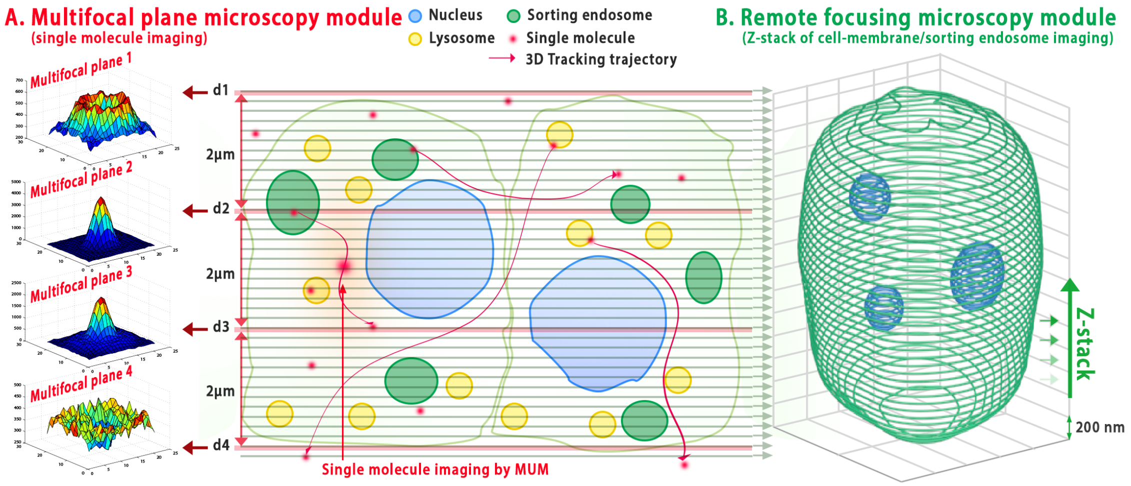

Figure 2.1: An example imaging experiment using the rMUM setup. Single molecule trajectories are imaged using the MUM-module (A), at the same time, z-stack images of cellular structures are obtained using the r-module (B).

of the single molecules are imaged using MUM in four focal plane images (Figure 2.1A, horizontal red lines). At the same time, cellular structures such as the plasma membrane and the endosomal compartments are acquired as a series of z-stack images using the remote focusing configuration (Figure 2.1B, horizontal green lines).

The rMUM setup is designed to carry out such an imaging experiment. The setup essentially consists of two different components that are attached to the standard microscope body (Figure 2.2A). Any standard microscope body can be used. The first major component is the remote focusing configuration that obtains 3D cellular environment information in the context of the single molecule trajectory. The second major component is MUM that acquires the 3D single molecule trajectories (see Section 2.2.1). A dichroic filter is set between two major components of the remote focusing microscopy module (see Section 2.2.2) and the MUM-module splits the emission light of cellular structures and single molecules accordingly in a wavelength-dependent manner. Precise single molecule locations are obtained by fitting 3D point spread functions to the images acquired from the cameras (C2-C5) in the MUM-module (see Figure 2.2B and Section 2.3.1). In between the two opposing objective lenses O2 and O3, the optical replica of the specimen is reconstructed. The r-module acquires 3D cellular structure images as a series of z-stacks (Figure 2.2C). The z-stacking is carried out by changing the focus of O3 using a piezo nanopositioner (PZ).

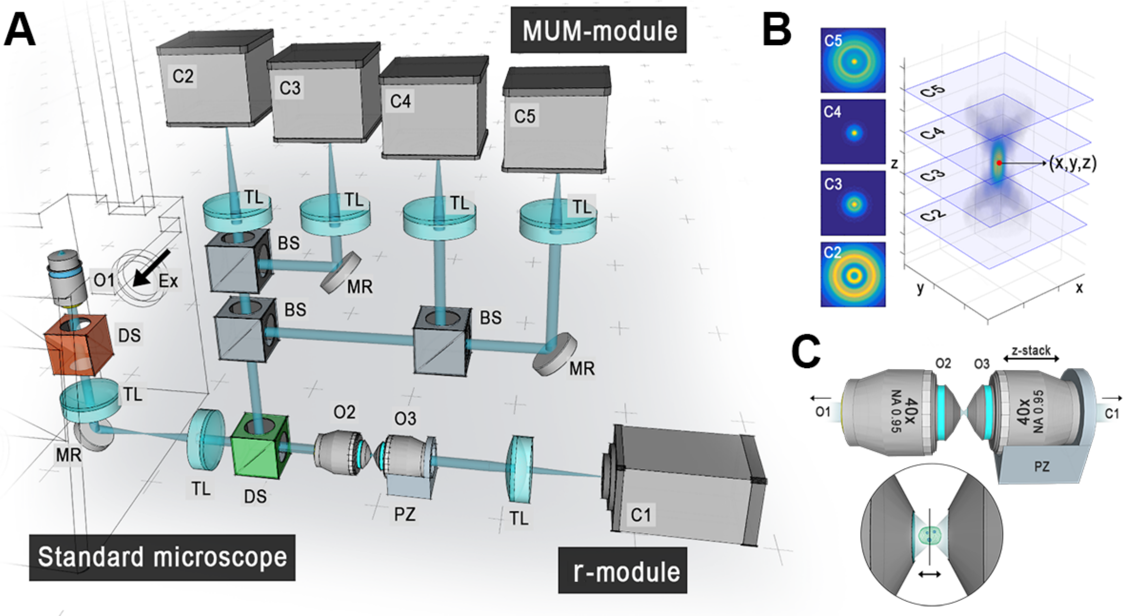

Figure 2.2: Illustration of emission light path of the rMUM setup. (A) Schematic of the rMUM setup configured with a standard microscope. The r- and the MUM-module is attached to the emission port of the microscope. (B) The MUM-module in (A) acquires four focal plane images of single molecules simultaneously using four EMCCD cameras (C2-C5). (C) In between two opposing objective lenses O2 and O3, an optical replica of the specimen is formed. Z-stack images of the specimen are obtained by moving O3 using the piezo nanopositioner (PZ).

More specifically, we assembled the rMUM setup with the following components (see Figure 2.2A): a standard inverted microscope with the excitation light path (Ex), a dichroic filter set (DS), an objective lens (O1), a tube lens (TL) and a mirror (MR). The emission light is split into the r-module and the MUM-module using a dichroic filter set (DS). The light entering the MUM-module is equally split into four light paths using three 50:50 beam splitters (BSs), which are simultaneously imaged using four cameras (C2-C5) that are positioned at specific distances from their respective tube lenses (TLs). The r-module is composed of two opposing objective lenses (O2 and O3), a piezo nanopositioner (PZ) and a camera (C1).

2.2.1 Multifocal plane microscopy module

The optical configurations of the multifocal plane microscopy module (MUM-module) are described in Section 2.2. The design of the specific spacings between the focal planes is carried out using the MUMDesignTool software package [63] (http://wardoberlab.com/software/mumdesigntool/). This tool assists in obtaining the optimal focal plane spacing for MUM experiments based on an information theoretic approach. With the current MUM configurations described in Section 2.2, we obtain the optimal focal plane spacing of 0.6 µm to 0.7 µm apart at each focus level. This ensures a localization accuracy of 5 nm and 15 nm in lateral and axial directions with 3.6 µm depth coverage with 1000 photons. The focal plane positions of the individual detectors are set by placing each detector at a specified distance from the corresponding tube lens through the use of appropriate spacers [35].

The MUM focal plane spacings are confirmed by analyzing a z-stack of images of a fluorescent bead sample that is acquired using a piezo objective focusing system. The fluorescent bead sample is prepared as follows: a 200 µl Poly-L-lysine solution (PLL, Sigma-Aldrich) is applied to the glass bottomed area of a Mattek dish for 10 minutes at room temperature. The PLL is then replaced with a fluorescent bead solution comprised of 0.5 nM TetraSpeck microspheres (Invitrogen) in 200 µl phosphate-buffered saline (PBS) for 10 minutes at room temperature. The sample is washed twice with PBS at room temperature followed by the addition of 1 mL PBS to the dish.

The fluorescent bead sample is imaged as follows: the bead sample is placed at the microscope stage 10 minutes before imaging to allow for temperature equilibration between the sample and the microscope, to reduce sample drift. Z-stack images are obtained using the MUM-module by moving the objective lens with, for example, a piezo positioner (or the sample in systems with an appropriately equipped sample stage) along the optical axis of the microscope in 50 nm step sizes. The four cameras in the MUM-module each acquire 10 images per step simultaneously, resulting in four sets of z-stack images (see Figure 2.3A).

For each of the imaged beads and for each of the piezo positions, a region of interest (ROI) is defined in each of the images acquired by the four cameras such that the bead is in the center of the ROI. For each of these ROIs, we calculate the ratio between the count in the center pixel and the average of the counts in the edge pixels. For the images from each camera, these ratios are then plotted as a function of the piezo position. Each of these four plots is smoothed by plotting a second order polynomial around the maximum of the plot. The locations of the maxima of these interpolating polynomials are taken as the focus positions of the corresponding detectors. The focal plane spacings are calculated as the differences between these focus positions. Figure 2.3 shows an example of the analysis. Z-stack images of a fluorescent bead in Figure 2.3A are analyzed as described above. The relative intensity of beads and the range of z positions are shown with corresponding second order polynomial fits (bold lines) in Figure 2.3B. 10 to 20 beads are typically analyzed using the same methods, and the focal plane position is determined by the

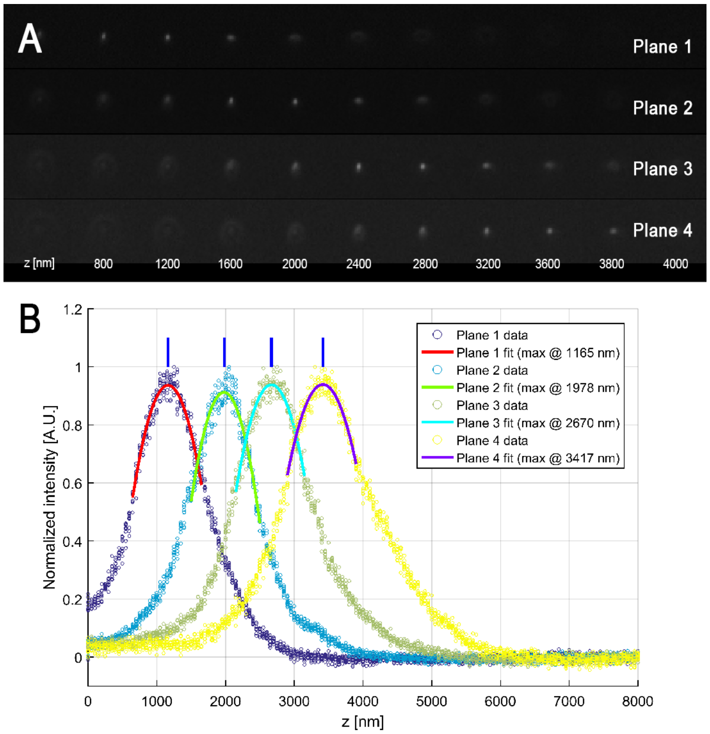

Figure 2.3: MUM-module calibration. The calibration experiment is carried out by acquiring z-stack images of a fluorescent bead sample using the MUM-module. (A) Z-stack images of the bead from four cameras are displayed. A bead appears at different z-positions in each camera image (Plane 1 to 4). (B) Processed intensity values of the z-stack images are plotted. The peak represents the relative focal plane position.

average of the measurements.

2.2.2 Remote focusing microscopy module

The remote focusing microscopy module (r-module) is designed as an attachment to a standard microscope. We follow a design as proposed by Wilson *et al.* [58]. Figure 2.4 shows a schematic of the r-module. The emission from a specimen is collected using an objective lens (O1), and the image is created at the image plane using a tube lens (TL1). The r-module is coupled after the image plane. The r-module consists of two concatenated microscopy systems. The first microscope, which is inverted in the light path forms an intermediate focal plane through an objective lens (O2). The second microscope in the r-module is used to image the intermediate focal plane with the second objective lens (O3). The images are recorded using a detector (C1). The second objective lens is mounted on a piezo nanopositioner to allow for the imaging of different intermediate focal planes.

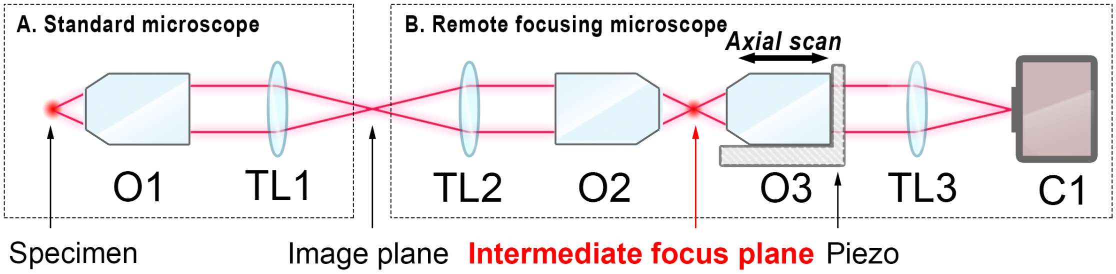

Figure 2.4: Schematic of the remote focusing microscopy module.

The overall magnification M_R of the r-module of the imaging system is given by

[58]

$$M_R = \frac{n_2 F_2 M_1}{n_1 F_1 M_2} \times \hat{M_3}, \tag{2.1}$$

where M_1 and M_2 denote the magnifications of the objectives O1 and O2, and $\hat{M_3}$ is the total magnification of the third microscope subsystem consisting of O3 and TL3. F_1 and F_2 denote the focal length of the tube lenses TL1 and TL2, and n_1 and n_2 denote the refractive indices of immersion media corresponding to objectives O1 and O2.

The rMUM system also supports multi-color volume imaging through the r-module. This can be achieved by using a multiband filter set. For example, the filter set in Figure 2.6 is composed of a multiband emitter and a multiband dichroic to capture the light from GFP and red fluorescent proteins (RFP) selectively. Imaging these two fluorescent proteins is achieved by alternating the excitation of the sample between excitation with a 488 nm laser and a 543 nm laser. For each z-position of the piezo one image is acquired for the GFP signal excited by the 488 nm laser, followed by one image for the RFP signal excited by the 543 nm laser (see Figure 2.10).

The maximum volume imaging speed λ_{max} in volumes per second (VPS) of the r-module is given by:

$$\lambda_{max} = \frac{1}{(P \times (\alpha + \max(T)))}, \tag{2.2}$$

where P denotes the number of steps in a z-stack, α is the minimum exposure time of the detector and T is defined as a vector $T := \tau, \phi$ where τ is the time taken to settle the piezo in a position stably, and ϕ is the delay by the acquisition software required for saving the acquired images, controlling the lasers, etc. For example, imaging a volume of 6 µm thickness with a step size of $\delta = 0.6$ µm requires $P_{6\mu\mathrm{m}} = 10$ frames per stack, or a volume of 4 µm thickness requires $P_{4\mu\mathrm{m}} = 6$ frames per stack. Further,

Table 2.1: The r-module operation speed with specific configurations.

sCMOS camera			Operation time		Volume imaging speed	
Pixel area	Maximum frame rate [FPS]	Minimum exposure time α [ms]	Piezo settling time τ [µs]	Software control time ϕ [µs]	4 µm depth coverage $P_{4\mu m} = 6$ [VPS]	6 µm depth coverage $P_{6\mu m} = 10$ [VPS]
2048x2048	100	10	6	6.5	10.1	6.1
1920x1080	192	5.2	6	6.5	14.3	8.5
512x512	403	2.4	6	6.5	18.7	11.2
128x128	1578	0.6	6	6.5	23.5	14.1

we assume that we image an area of 53 × 53 μm^2 using an sCMOS camera which acquires images at a rate of 403 frames per second (FPS), i.e., with an exposure time of $\alpha = 2.48$ µs for the given imaging area of 512×512 pixel^2. The piezo settling time was measured to be $\tau = 6$ µs for the case when the piezo moves a relatively small step size. The operation time of our acquisition software was measured to be $\phi = 6.5$ µs, which includes the execution times for the controls for the cameras, the lasers, the piezo including its settling time, and the saving of the images to disk. With these conditions, the maximum volume imaging speed of the given r-module imaging system is 11.2 VPS for a 6 µm thick volume or 18.7 VPS for a 4 µm thick volume. Table 2.1 shows the maximum volume imaging speeds for different conditions.

2.2.2.1 Alignment of the r-module optics

Precise alignment of the optics in the r-module is essential for obtaining aberration-free images. To achieve this, an r-module optics alignment tool was developed. Figure 2.5A shows a schematic of the r-module alignment tool. The tool is configured with a laser, a 50:50 beam splitter, and a target screen (alignment screen). Any kind of laser can be used, but a green class 2 laser is recommended for visibility and safety. Here the laser line defines the optical axis of the target optics. The laser beam points out toward the optics to be aligned. The laser transmitted through the target optics has some amount of reflection at the surface. For example, a typical convex lens transmits 95% to 99% of the incident light while reflecting much of the rest. A simple lens has two interfaces one at the front and one at the back surfaces. Multiple reflections are introduced by these two interfaces. Half the reflected laser beam is directed to an alignment screen using a 50:50 beam splitter. Figure 2.5B shows an example of the various beam paths displayed on the screen. If the optics are perfectly aligned with respect to the optical axis of the laser line, all the reflections will overlap to produce a single spot on the screen. In other words, multiple spots will appear on the screen if the target optics are not aligned properly. In Figure 2.5B, red and blue spots are shown on the screen which come from the reflections from the reflections from the front and back surfaces of the lens.

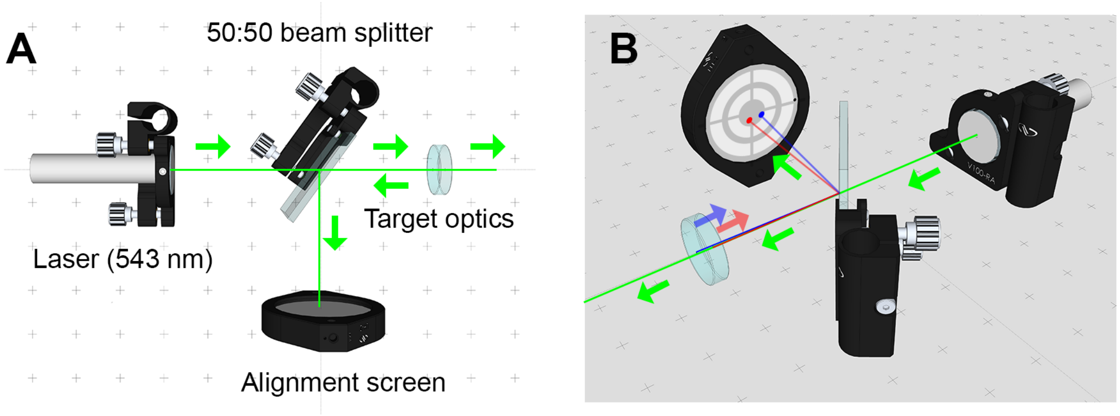

Figure 2.5: Schematic of r-module optics alignment tool.

The r-module is assembled with a standard microscope. Therefore, we first need to use the alignment tool to find the optical axis of the standard microscope. The optics in the standard microscope are fixed, so we cannot align the microscope optics to the alignment tool. Instead, we adjust the alignment tool to place the laser line on the optical axis of the microscope using the same technique described above. Next, we add the r-module optics into the optical axis. Here the optics that need to be added closest to the microscope are aligned first. The addition of optics increases the number of spots, and all the spots have to be aligned as one in the center of the screen.

The following conditions should be satisfied at the completion of the r-module construction. First, the magnification of the optical system has to match Equation 2.1. Magnifications can be measured by imaging a micro-ruler. Second, the shape of point spread function (PSF) should correspond to a theoretical PSF (e.g., Born & Wolf PSF [64]).

2.2.3 rMUM configurations

The rMUM setup is designed as a module that is attached to a standard commercial microscope that is equipped with suitable laser excitation. Attaching an rMUM module to the standard microscope does not require significant modifications of the existing microscope system, in contrast to many other advanced microscopy methods. In addition to the excellent adaptability, the rMUM configuration is highly flexible in that it can be transformed into a multi-modality microscope. For example, the MUM-module and the r-module can be operated separately. The MUM-module can be used as an 3D super-resolution microscopy system. The r-module alone can be used as a conventional 3D imaging system with a high volume scanning rate and supporting multiple channels.

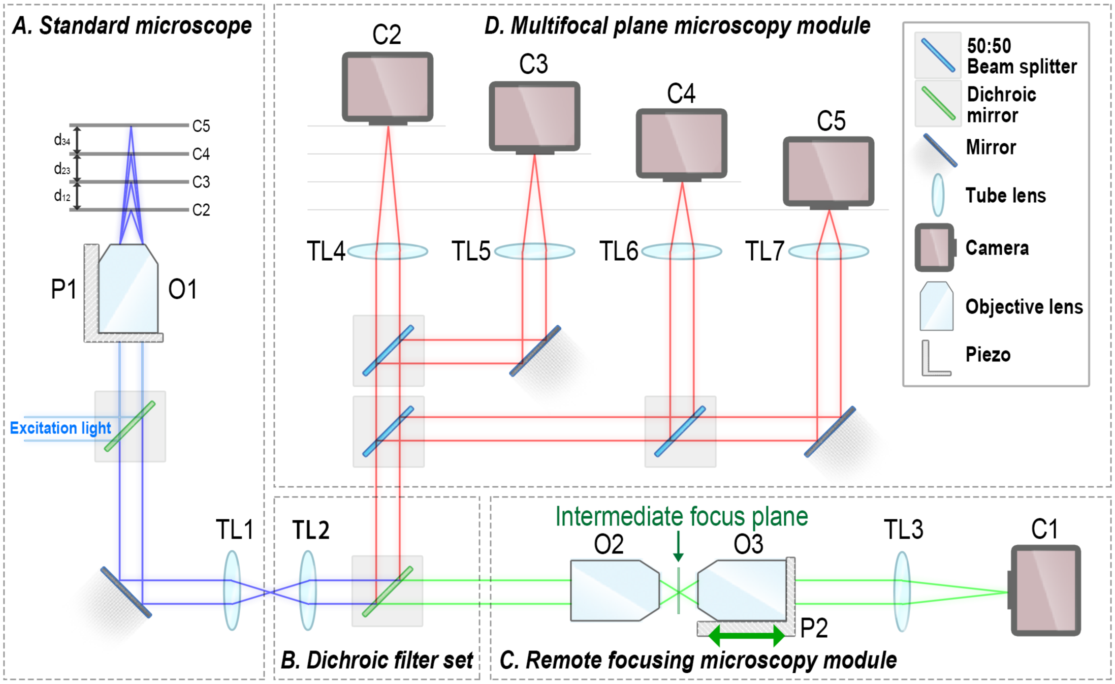

Figure 2.6: rMUM setup with four focal plane configuration.

We demonstrate the flexibility of the rMUM system by with two different rMUM setups. Figure 2.6 shows an rMUM setup with four focal plane MUM configuration. Here, emission from the sample is collected using a standard inverted microscope (Observer A1, Zeiss) with a Zeiss 63× NA 1.4 oil immersion objective lens, O1. The emission light is split by a wavelength dependent dichroic filter set (89019bs; Chroma, ff01-507-582, ff01-655-15; Semrock) into the r- and MUM-modules. Here the fluorescent emission of QD655 is reflected into the MUM-module, and the fluorescent emission of GFP or RFP passes through the filter to the r-module. The MUM-module is set up to acquire data for single QDs from four distinct focal plane images simultaneously, using four identical EMCCD cameras, C2-C5 (iXon DU897-BV; Andor Technologies). The spacings d_{12}, d_{23} and d_{34} between the focal planes are 0.642, 0.637 and 0.675 µm, respectively. The r-module consists of two opposing Zeiss 40× NA 0.95 dry objective lenses, O2 and O3. The intermediate focal plane is created between objective lenses O2 and O3. The change of focus is achieved using a piezo nanopositioner, P2, attached to O3. A sCMOS camera (Zyla 4.2; Andor Technologies), C1, is used as a detector for the r-module. This rMUM setup supports large depth coverage by having four focal planes in the MUM-module, and can capture dual-color z-stack images using the r-module.

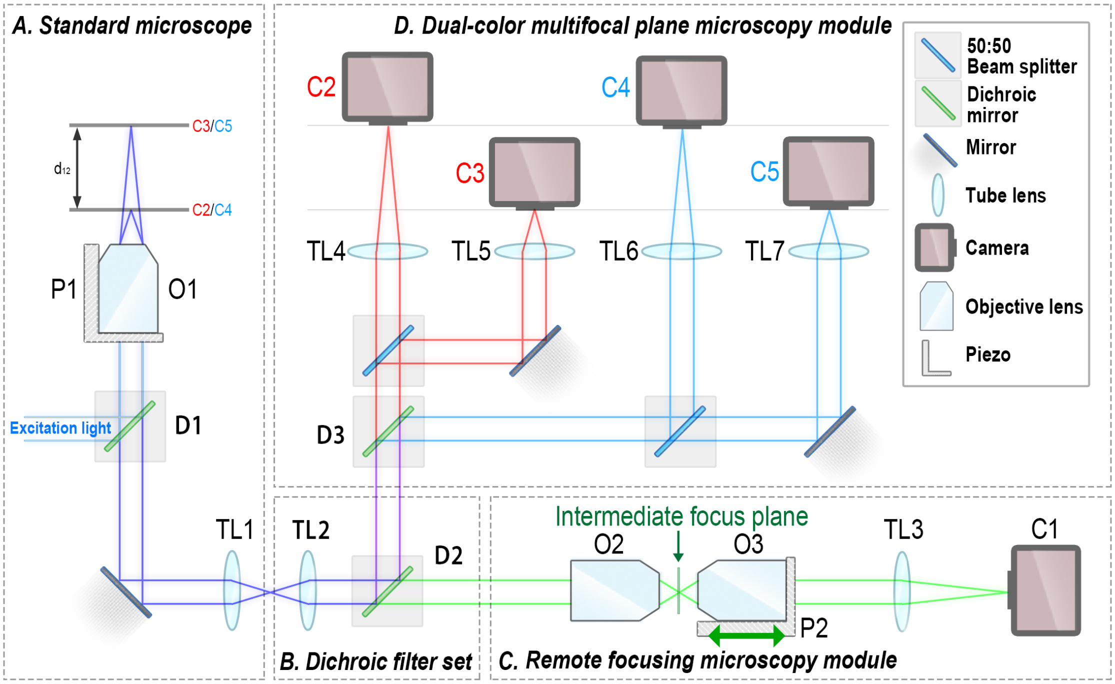

Figure 2.7: rMUM setup with dual-color two focal plane configuration.

The second rMUM configuration is capable of dual-color two focal plane MUM imaging (see Figure 2.7). The excitation light is reflected to illuminate the specimen using a quad-band dichroic filter D1 (Di01-R405/488/543/635-25x36; Semrock). Emission from the sample is collected using a standard inverted microscope (Observer A1, Zeiss) with a Zeiss 63× NA 1.4 oil immersion objective lens, O1. The emission light is split by a wavelength—dependent dichroic filter set D2 (89019bs; Chroma, ff01-507-582, ff01-655-15; Semrock) into the r- and the MUM-module. Here the fluorescent emission from QD655 and GFP is reflected into the MUM-module, and the fluorescent emission of RFP passes through a filter to the r-module. The fluorescent emission is split into two channels using a wavelength dependent dichroic filter set D3 (FF01-520/35, FF01-676/37, FF560-Di01, Semrock) as it enters the MUM-module. Each channel is imaged using two identical EMCCD cameras, i.e. four cameras for two channels with two focal planes, C2-C5 (iXon DU897-BV; Andor Technologies). The spacing d_{12} between the focal planes is set to 0.612 µm for each channel. The r-module consists of two opposing Zeiss 40× NA 0.95 dry objective lenses, O2 and O3. The intermediate focal plane is created between objective lenses O2 and O3. The change of focus is achieved using a piezo nanopositioner, P2, attached to O3. An sCMOS camera (Zyla 4.2; Andor Technologies), C1, is used as a detector for the r-module. This rMUM setup is capable of imaging rapid dynamics of a single molecule or the cellular compartments in dual color.

The r-module magnification with the configuration as described above can be obtained using Equation 2.1. Zeiss tube lenses (f = 164.5 mm) were used for the setup. The magnification of the r-module $M_R = 41.6\times$.

2.3 rMUM data processing

An rMUM setup consist of a r- and a MUM-module. The r-module acquires z-stack images, while the MUM-module simultaneously obtains multifocal plane images. The r- and the MUM-modules acquire images at different frame rates. The rMUM setup also performs multi-color imaging. Taking these factors about the rMUM setup into account, the analysis was performed as follows. First, single molecule images from the MUM-module are processed using the MUMLA algorithm (see Section 2.3.1). 3D single molecule trajectories are then mapped into the r-module image space by a spatial registration process (see Section 2.3.2). The r-module data is temporally synchronized to the MUM module data (see Section 2.3.3), followed by a deconvolution process (see Section 2.3.4).

2.3.1 Localization

Precise 3D locations of single molecules are identified using the MUM localization algorithm (MUMLA) with the four focal plane MUM setup as described previously [34, 35]. We first select a pair of focal plane images that contain the brightest signal from the QDs. A small region of interest (ROI) containing the QD image is then selected from these images and fit to a pair of 3D point spread function profiles given by

$$\begin{aligned}&\mu_\theta^1(p,t)\\&=\frac{\alpha^2 At}{\pi M_1^2}\iint_{C_p}\left|\int_0^1 J_0\left(\frac{\alpha}{M_1}\sqrt{(x-M_1x_{01})^2+(y-M_1y_{01})^2}\rho\right)e^{jW_{z_0}(\rho)}\rho d\rho\right|^2 dxdy,\end{aligned}$$

$$\mu_\theta^2(q,t)$$

$$= \frac{\alpha^2 At}{\pi M_2^2} \iint_{C_q} \left| \int_0^1 J_0 \left(\frac{\alpha}{M_2} \sqrt{(x - M_2 x_{02})^2 + (y - M_2 y_{02})^2} \rho \right) e^{jW_{z_0 - \delta_{12}}(\rho)} \rho d\rho \right|^2 dxdy, \tag{2.3}$$

to the above described ROIs, which had the background signals subtracted. The background signal is estimated by averaging intensity values from the edge pixels of the region of interest. Here $\theta = z_0$ denotes the z-location of the QD, (x_{01}, y_{01}) and (x_{02}, y_{02}) denote the center of the QD images in the two ROIs, C_p and C_q denote the p^{th} and q^{th} pixel in the 1st and 2nd ROIs, respectively, $p, q = 1, ..., N$, where N denotes the total number of pixels in the ROI, $\alpha = 2\pi NA/\lambda$, NA denotes the numerical aperture of the objective lens, λ denotes the wavelength of the detected photons, M_1 and M_2 denote the magnification at the two focal planes, A denotes the photon detection rate, t denotes the exposure time, δ_{12} denotes the spacing between the two focal planes, and W_{z_0} denotes the phase aberration term. Here we choose W_{z_0} as the Born and Wolf point spread function model [64, 65] which is given by

$$I_{z_0}(x,y) = \left| C \int_0^1 J_0 \left(\frac{2\pi NA}{\lambda} (\sqrt{x^2+y^2}) \rho \right) e^{jW_{z_0}(\rho)} \rho d\rho \right|^2, \tag{2.4}$$

where $(x, y) \in R^2$ denotes an arbitrary point on the detector plane, C is a constant with complex amplitude, λ denotes the wavelength of the detected photons, NA denotes the numerical aperture of the objective lens, J_0 denotes the zeroth order Bessel function of the first kind and W_{z_0} denotes the phase term given by

$$W_{z_0}(\rho) = \frac{\pi (NA)^2 z_0}{n_{oil}\lambda} \times \rho^2, \rho \in [0, 1], \tag{2.5}$$

where z_0 denotes the axial location of the single molecule and n_{oil} denotes the refractive index of the immersion oil.

2.3.1.1 MUMLA for r-module

We adopt an analogous MUMLA approach to estimate point source/bead locations from data acquired in the r-module. In particular, this was used for the spatial registration process that requires correlated control points from the r- and the MUM-module. For a set of z-stack images of a 3D bead sample from the r-module, we proceed as follows. For each bead image, we create a small region of interest containing the possibly defocused bead image in each of the four focal planes of the z-stack images that are closest to the in-focus position of the bead. Using a maximum likelihood estimation approach [65], we fit the four 3D point spread function profiles given by

$$\begin{aligned}
&\mu_\theta^1(k,t)\\
&= \frac{\alpha^2 At}{\pi M_1^2}\iint_{C_k}\left|\int_0^1 J_0\left(\frac{\alpha}{M_1}\sqrt{(x-M_1x_{01})^2+(y-M_1y_{01})^2}\rho\right)e^{jW_{z_0}(\rho)}\rho d\rho\right|^2 dxdy,\\
&\mu_\theta^2(l,t)\\
&= \frac{\alpha^2 At}{\pi M_2^2}\iint_{C_l}\left|\int_0^1 J_0\left(\frac{\alpha}{M_2}\sqrt{(x-M_2x_{02})^2+(y-M_2y_{02})^2}\rho\right)e^{jW_{z_0-\delta_{12}}(\rho)}\rho d\rho\right|^2 dxdy,\\
&\mu_\theta^3(m,t)\\
&= \frac{\alpha^2 At}{\pi M_3^2}\iint_{C_m}\left|\int_0^1 J_0\left(\frac{\alpha}{M_3}\sqrt{(x-M_3x_{03})^2+(y-M_3y_{03})^2}\rho\right)e^{jW_{z_0-\delta_{13}}(\rho)}\rho d\rho\right|^2 dxdy,\\
&\mu_\theta^4(n,t)\\
&= \frac{\alpha^2 At}{\pi M_4^2}\iint_{C_n}\left|\int_0^1 J_0\left(\frac{\alpha}{M_4}\sqrt{(x-M_4x_{04})^2+(y-M_4y_{04})^2}\rho\right)e^{jW_{z_0-\delta_{14}}(\rho)}\rho d\rho\right|^2 dxdy,
\end{aligned} \tag{2.6}$$

to the above described ROI, which had the background signals subtracted. The background signal is estimated by averaging intensity values from the edge pixels of the region of interest. Here, $\theta = z_0$ denotes the z-location of the bead; $(x_{01}, y_{01}), (x_{02}, y_{02}), (x_{03}, y_{03})$ and (x_{04}, y_{04}) denote the estimated locations of the beads in the four ROIs; C_k, C_l, C_m and C_n denote the k^{th}, l^{th}, m^{th} and n^th pixel for each region of interest, respectively, $k, l, m, n = 1, ..., N$, where N denotes the total number of pixels in the region of interest; $\alpha = 2\pi NA/\lambda$; NA denotes the numerical aperture of the objective lens; λ denotes the wavelength of the detected photons; M_1, M_2, M_3 and M_4 denote the magnifications corresponding to the four focal planes; A denotes the photon detection rate; t denotes the exposure time; $\delta_{12} = \delta_{23} = \delta_{34}$ denote the distances between the focal levels of two successive focal positions of the r-module with $\delta_{13} := \delta_{12} + \delta_{23}$ and $\delta_{14} := \delta_{12} + \delta_{23} + \delta_{34}$. W_{z_0} is defined as in Equation 2.5.

All computations were performed using custom software written in MATLAB (The Mathworks) and the C programming language.

2.3.1.2 Localization computation

The single molecule localization processes are computationally expensive. The process requires evaluating complex PSFs at various subpixel points on a finely spaced grid. These evaluations need to be repeated multiple times for a single estimation process. This is especially true for 3D PSF models such as Born and Wolf PSF model [64] in Equation 2.5 due to the use of the Bessel function. Therefore, computation itself is a major challenge for 3D single molecule localization using MUMLA.

A graphics processing unit (GPU) was traditionally used for rendering video output from computers. Since video rendering needed to be efficient for fast refresh

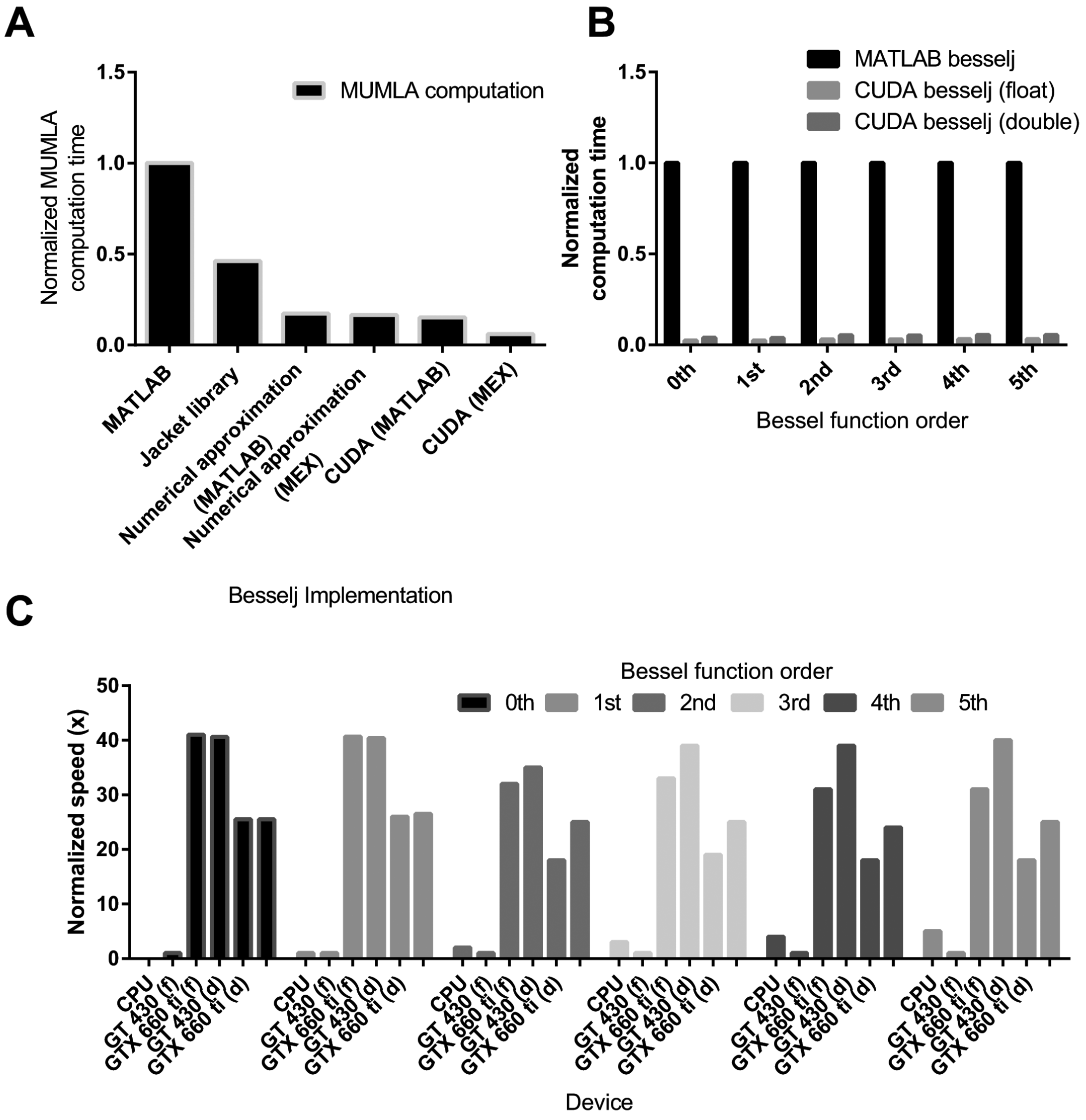

Figure 2.8: GPU accelerated MUMLA computation. (A) Three-dimensional single molecule location estimation using MUMLA algorithm with 6 different implementations: MATLAB Bessel function, Bessel function from Jacket library (MATLAB-GPU library), MATLAB with numerically approximated Bessel function, C implementation of numerically approximated Bessel function and CUDA implementation of numerically approximated Bessel function. (B) Computations of Bessel function of 0th to 5th order are performed using the MATLAB Bessel function, CUDA Bessel function with single precision, and CUDA Bessel function with double precision. (C) Same Bessel function implementations of (B) are tested with two different graphics cards: GT 430 and GTX 660 Ti from NVIDIA®.

rates, the GPU is optimized to perform simple computations, such as addition and multiplication in parallel. In recent years there have been large efforts made to use the GPU as a general computation module [66]. For example, the compute unified device architecture (CUDA) is a parallel computing platform and programming model created by NVIDIA®. Here we use CUDA to improve the speed of computations involved in MUMLA.

During the 3D localization using MUMLA, the Bessel function appears to be the most computationally expensive part. We therefore optimized the Bessel function computation. Figure 2.8A shows the MUMLA computational time comparison with six different implementations of Bessel function: MATLAB, Jacket library (MATLAB GPU library), a simplified numerical approximation of Bessel function implemented in MATLAB or MEX (C++), or using CUDA in MATLAB or MEX (C++). CUDA(MEX) implementation appears to be 16.5 times faster than the original implementation. The Bessel function computation alone is 41 times faster (single precision, 6 digits) or 25.5 times faster (double precision, 15 digits) than the MATLAB implementation (Figure 2.8B). Note that 1024 or 512 GPU cores were used for the single or double precision modes respectively. Double precision requires two GPU cores for the graphics card used for the tests. The same computation is performed using two graphics cards, GT 430 and GTX 660ti from NVIDIA® (Figure 2.8C). GTX 660ti is superior to GT 430 in terms of technical specifications. There is no difference between the two graphics cards in the computation speed of the Bessel function 0th order. However, GTX 660ti speeds up for the high order Bessel function calculation.

2.3.2 Spatial registration

The rMUM imaging experiment produces 3D single molecule trajectories from the MUM-module and cellular structure z-stack images from the r-module simultaneously. These single molecule and cellular data sets have to be spatially registered in 3D. To perform the registration between the data from the r- and the MUM-module, a calibration experiment is designed using a 3D bead sample.

The 3D bead sample was prepared as follows: 200 µl 30% acrylamide/bis, 37.5:1 solution (Bio-Rad) was mixed with 2 µl 100 nm TetraSpeck microspheres (Invitrogen). 3 µl Tetramethylethylenediamine (TEMED; Bio-Rad) and 6 µl 10% ammonium persulfate (Sigma-Aldrich) were added to the mixture, which was then transferred to the glass bottomed area of a Mattek dish. The mixture was pipetted up and down for a few seconds, and the dish was covered to facilitate gel polymerization. Ten minutes later, 2 mL 1X Tris–Glycine–Sodium dodecyl sulfate buffer (TGS; Bio-Rad) was added to the dish.

The sample was imaged within two hours of preparation using the rMUM setup. For each acquisition time point, the MUM-module simultaneously acquired one set of four focal plane images of the sample. At the same time, the r-module acquired one set of z-stack images of the sample. Note that the registration sample was imaged twice, once before and once after the rMUM imaging experiment.

Here we register the single molecule coordinates obtained by the MUM-module with the images of the cellular context acquired by the r-module. Here the coordinate system for the r-module is defined in such a way that the x-y plane coincides with the image planes.

In order to be able to obtain the transformation mapping from the MUM coordinate system to the coordinate system of the r-module, the 3D bead sample was imaged using the rMUM setup. The locations of the beads serve as control points for the registration algorithm. We estimated the 3D locations of the beads/control points using MUMLA and obtained estimated coordinates $\hat{c}^M = (\hat{x}^M, \hat{y}^M, \hat{z}^M)^T, q = 1, ..., Q,$ in the MUM-module coordinate system and $\hat{c}^R = (\hat{x}^R, \hat{y}^R, \hat{z}^R)^T, q = 1, ..., Q,$ in the r-module coordinate system.

We assume that there exists an affine transformation T between the coordinate system defined for the r-module and the coordinate system for the MUM-module:

$$T : \mathbb{R}^3 \to \mathbb{R}^3, x \mapsto A \times x + s, \tag{2.7}$$

where A is a 3×3 matrix and s is a 3×1 vector. Estimates $\hat{A}$ and $\hat{s}$ of the matrix A and the vector s are obtained from the estimates of the control point coordinates $\hat{c}_q^M$ and $\hat{c}_q^R, q = 1, ..., Q$, using an extension of the multivariate generalized least squares algorithm that is based on an errors-in-variables data model [67, 68].

We assume that we have identified P single molecules as imaged in the MUM-module. Using MUMLA (see Section 2.3.1), we determine the location $d_{p,t_l}^M = (x_{p,t_l}^M, y_{p,t_l}^M, z_{p,t_l}^M)^T \in \mathbb{R}^3$ of each of the single molecules at the time point t_l^M with $T_{min}^M = t_1^M < \cdots < t_l^M < \cdots < T_{max}^M, p = 1, ..., P$. The registered coordinates $d_{p,t_l}^{Re_M} = (x_{p,t_l}^{Re_M}, y_{p,t_l}^{Re_M}, z_{p,t_l}^{Re_M})^T \in \mathbb{R}^3$ of single molecule locations obtained in the MUM-module $d^M = (x_{p,t_l}^M, y_{p,t_l}^M, z_{p,t_l}^M)^T \in \mathbb{R}^3$ are then calculated as

$$d_{p,t_l}^{Re_M} = \hat{A} \times d_{p,t_l}^M + \hat{s}, \tag{2.8}$$

where $T_{min}^M = t_1^M < \cdots < t_l^M < \cdots < T_{max}^M, p = 1, ..., P$.

Figure 2.9A shows an example of a registration sample imaged using the rMUM setup. The bead sample imaged using the r-module and the MUM-module is visu-

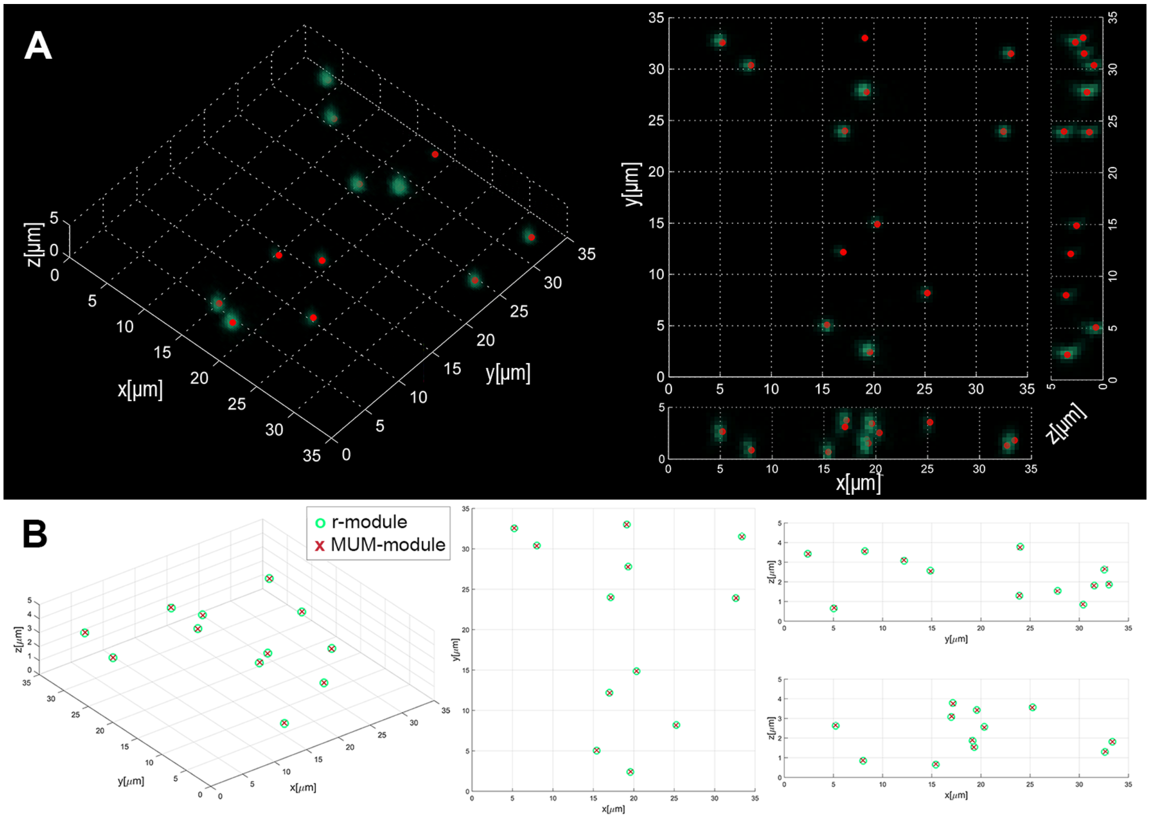

Figure 2.9: Imaging a 3D bead sample using the rMUM setup. (A) A 3D bead sample is imaged using the rMUM setup. 3D reconstruction of z-stack images from the r-module (green voxel) and bead locations from the MUM-module (red spheres) are visualized. (B) Locations of the same 3D bead sample from (A) is plotted in 3D. 3D bead positions from both the r- and the MUM-module (green circles and red crosses, respectively) are estimated using MUMLA.

alized as green voxels and red spheres, respectively. The right panels are the x-y projection (upper middle panel), the x-z projection (lower right panel) and the y-z projection (upper right panel) of the 3D visualization in the left panel. In Figure 2.9B, 3D coordinate plots of the 3D bead sample are displayed as red crosses (x) and green circles (o) for the r- and MUM-module data respectively. Here the 3D coordinates are obtained using MUMLA (see Section 2.3.1). The coordinates from the r- and the MUM-modules are visualized in the 3D projection (left panel), x-y projection (middle panel), y-z projection (upper right panel) and x-z projection (lower right panel).

2.3.3 Temporal registration

The temporal registration between data from the r- and the MUM-module is essential for both visualization and data analysis. There are two complications to achieving appropriate temporal registration. First, the r- and the MUM-module typically operate at different frame rates. Second, in the r-module all images, particularly the images for the different focal positions are acquired sequentially, whereas in the MUM-module, for each acquisition time point the images for all focus points are acquired simultaneously.

Typically, the r- and the MUM-module operate at different frame rates during the rMUM operation. The r-module acquires z-stack images at rates of 50-400 FPS. At the same time, the MUM-module obtains single molecule images over multiple focal planes simultaneously at frame rates of 10-25 FPS. These acquisition frame rates are chosen based on the sample conditions, the signal and background noise levels and the object dynamics. The data acquisition rate of the r- and the MUM-module is designed in a semi-synchronous manner: the r-module runs “n” times faster than the

MUM-module where “n” is a positive integer.

The r-module acquires time-lapse z-stack images. Therefore, the images are not only correlated with the axial position, but with time as well. In addition, this correlation depends on the method of the r-module operation. We assume that the r-module acquires K^R z-stack plane images in a step size δ [µm] at each time point t_l^R with $T_{min}^R = t_1^R < \cdots < t_l^R < \cdots < T_{max}^R$ with two scanning modes: mono-directional scan and bi-directional scan (see Figure 2.10 for a graphical representation).

We first interpolate the images temporally so that at each time point we have a z-stack of images available for analysis and visualization. We can obtain this by interpolating the images corresponding to the same z-focus level with a linear function to obtain interpolants at the time points at which no image is available at that particular z position (see Figure 2.11B).

For voxel-based 3D visualization, it is important to have voxels of uniform spatial dimensions. In order to achieve this, we need to interpolate the z-stacks along the z-direction so that z increments of the interpolated images match the dimensions of the image pixels. At each time point, we interpolate the available images using the B-splines [69] to obtain images such that their distances in the z-direction equal the pixel length of the cameras (see Figure 2.11C).

Figure 2.10A and B illustrate the r-module operation in the mono-directional scan mode and the bi-directional scan mode. The sequence of acquiring images is represented as red rectangles. In the mono-directional scan mode, the piezo returns to the original starting position at every completion of the acquisition of a z-stack to acquire the next z-stack images. In the bi-directional scan mode, the piezo moves in one direction to acquire a z-stack and then moves the opposite direction to acquire a further z-stack. Either scan mode of the r-module is capable of multi-color volume imaging (see Figure 2.10). This is carried out by sequentially obtaining images of the

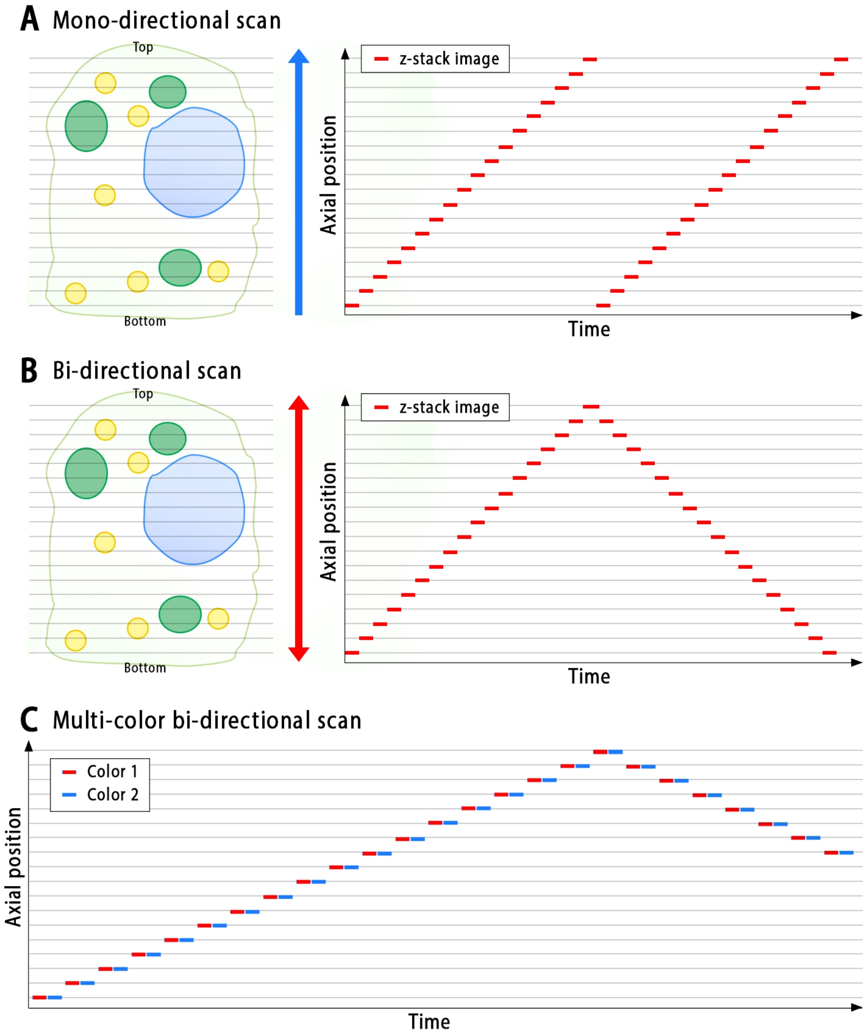

Figure 2.10: Z-stack image acquisition using the r-module. The r-module acquires z-stack images of the specimen in two scanning modes: (A) Mono-directional scan and (B) Bi-directional scan. (C) The r-module is also capable of multi-color imaging by acquiring, for example, two color images, sequentially, per z-position.

different fluorophores at each focal level. For example, two-color imaging is carried out by obtaining two images at each focus position, one through excitation with the first laser and the second one through excitation with the second laser.

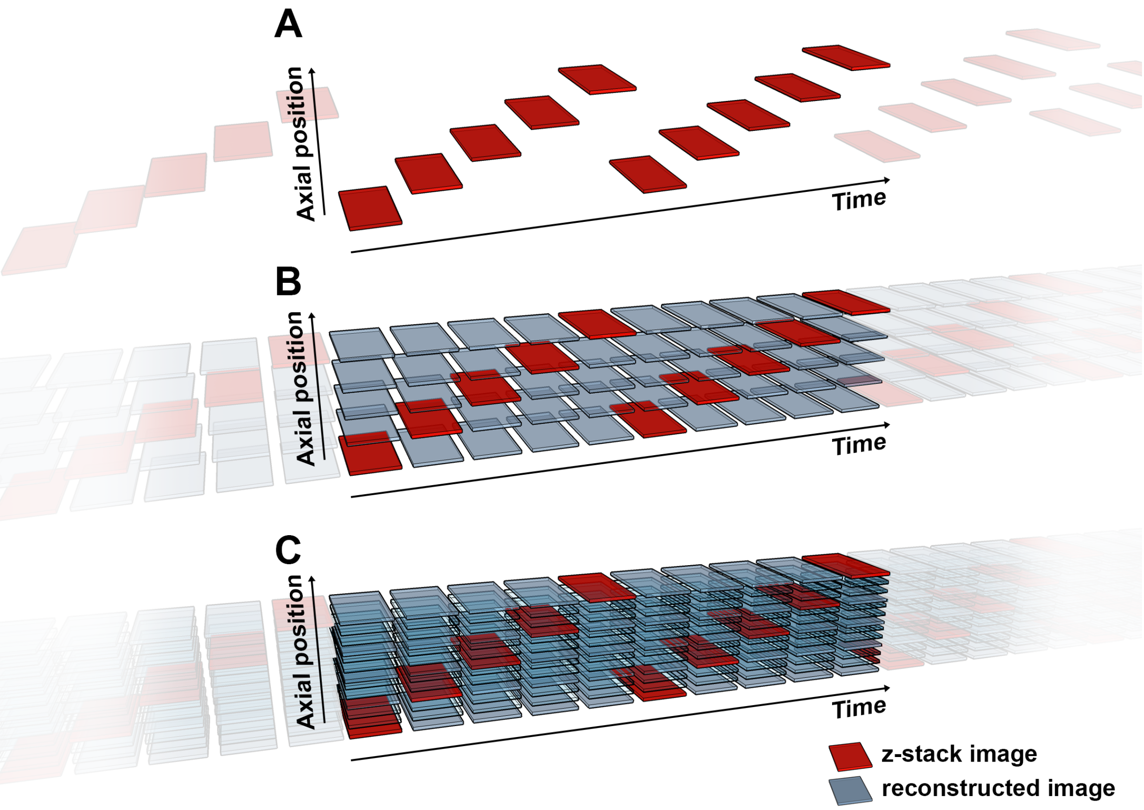

Figure 2.11: An example of the 4D reconstruction of z-stack images from the r-module. (A) Z-stack images from the r-module consist of one image per z-position at each timepoints (red rectangle). (B) Missing images between adjacent timepoints at a particular z-position are filled using a linear interpolation method. (C) Images reconstructed from (B) have non-isotopic dimensions between x-y and z. Images are created between z-positions using B-spline interpolation.

Figure 2.11 exemplifies the temporal registration process described above. In Figure 2.11A, the r-module sequentially acquires five images in the mono-directional mode. Here the acquired images are represented as red rectangles. Such a sequential acquisition produces one image at a time, and therefore there are "missing" images at different z focus levels over a z-stack. These "missing" images are represented as grey rectangles in Figure 2.11B. These images are obtained by linear interpolation methods. In Figure 2.11C, we generate images in the z-direction using B-spline interpolation so that the spacing between consecutive images in the z-direction matches the spacing in the x- and y- directions. This is used for the voxel-type volume visualization.

The temporal registration process with the r-module images is extremely computationally intensive. Therefore, analysis is optimized by processing a subset of the data as a sliding window along the time dimension. All computations were performed using the MIATool custom developed software module in MATLAB (The Mathworks).

2.3.4 Deconvolution

The z-stack images acquired from the r-module were first deconvolved using the Richardson-Lucy algorithm [70, 71]. Figure 2.12 shows an example of the deconvolution process. Here we have the cross sections of z-stack images in x-y, y-z and x-z directions along the yellow lines. A set of z-stack images were simulated using the measured 3D point spread function (Figure 2.12A). The simulated point sources were arranged in a triangular pyramid shape (Figure 2.12B). Figure 2.12C shows the deconvolution results. The cross section images clearly show all four dots of the triangular pyramid edges.

A challenge of the deconvolution process is the computational expense; which requires an enormous amount of memory and significant computational power. The r-

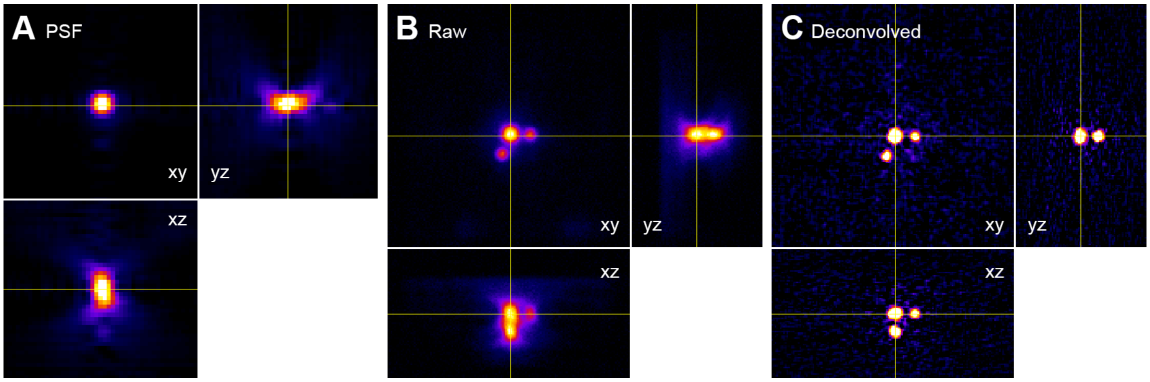

Figure 2.12: An example of deconvolution with simulated images. (A) An experimental point spread function (PSF) is obtained by acquiring z-stack images of a bead sample. (B) A set of z-stack images is simulated using the PSF from (A). (C) Images from (B) are deconvolved.

module produces time-lapse z-stack images at a rapid rate; resulting in large amount of data. To improve the computational efficiency, we adapted the idea of using a GPU from Section 2.3.1.2 for the deconvolution process [72]. The Richardson-Lucy deconvolution algorithm is implemented using CUDA in MATLAB. This GPU implementation make the deconvolution process 1.6 times faster.

2.4 rMUM data analysis

rMUM provides single-molecule trajectories with images of the cellular structure that the single molecules interact with. To understand the context of single molecule dynamics, sophisticated data analysis methods are required. We measure diffusion rates in relation to the cellular structure (see Sections 2.4.1 and 2.4.4). Complex single molecule trajectories that are composed of two different diffusive motions are analyzed using probability distribution of square displacement analysis (see Section 2.4.3). An automated tracking algorithm [73, 74, 75] is used to quantify rMUM data. Associations between single molecule tracks and cellular structure are evaluated as well (see Section 2.4.6). Finally, rMUM data is visualized using 3D voxel or isosurface displays (see Section 2.4.7).

2.4.1 Diffusion coefficient measures

Complex diffusion dynamics of the single molecule trajectories are quantified by measuring diffusion coefficients. The diffusion coefficient measures are carried out using mean square displacement (MSD) analysis [73, 76]. We classified diffusion dynamics into four different scenarios: two-dimensional unconstrained diffusion, three-dimensional unconstrained diffusion, directed diffusion, and unconstrained diffusion on a sphere. Three types of experiments are analyzed: two-dimensional tracks, three-dimensional tracks, and tracks on the surface of spherical structures.

2.4.1.1 Two-dimensional unconstrained diffusion

For a series of two-dimensional single molecule track coordinates $(x(k), y(k)), k = 1, ..., N$, captured in N frames, the MSD is described as

$$MSD_{2D}(\Delta t_n) = \frac{1}{N-1-n} \sum_{j=1}^{N-1-n} \{[x(j\delta t + n\delta t) - x(j\delta t)]^2 + [y(j\delta t + n\delta t) - y(j\delta t)]^2\}, \tag{2.9}$$

where $\Delta t_n = n\delta t$ with the frame time δt and n is the time increment. If the single molecule undergoes unconstrained diffusion, the MSD is described by

$$MSD_{2D}(\Delta t_n) = 4D_{2D}\Delta t_n + 4\sigma^2, \tag{2.10}$$

where D_{2D} is the diffusion coefficient and σ is the average localization precision [77]. Motivated by this identity, the diffusion coefficient can be estimated by fitting a linear function to the plot of MSD versus Δt_n of Equation 2.9. The time increment is chosen as $n = 1, ..., 5$ [78].

2.4.1.2 Three-dimensional unconstrained diffusion

The diffusion of a single molecule in three-dimensional space is carried out analogously. The MSD for a series of track coordinates in three dimensions $(x(k), y(k), z(k)), k = 1, ..., N$, captured in N frames can be expressed as

$$MSD_{3D}(\Delta t_n) = \frac{1}{N-1-n} \times \sum_{j=1}^{N-1-n} \{[x(j\delta t + n\delta t) - x(j\delta t)]^2 + [y(j\delta t + n\delta t) - y(j\delta t)]^2 + [z(j\delta t + n\delta t) - z(j\delta t)]^2\}, \tag{2.11}$$

where $\Delta t_n = n\delta t$ with the frame time δt and n is the time increment. For unconstrained three-dimensional diffusion, the diffusion coefficient D_{3D} is also given by

$$MSD_{3D}^{Normal}(\Delta t_n) = 6D_{3D}\Delta t_n + 6\sigma^2, \tag{2.12}$$

where σ is the average localization precision [77]. The measurement of the diffusion coefficient is carried out by fitting a linear function to the plot of MSD versus Δt_n of Equation 2.11, where we have chosen $n = 1, ..., 5$ [78].

2.4.1.3 Three-dimensional directed diffusion

For a single molecule that moves directionally with a velocity V, the MSD can be expressed as

$$MSD_{3D}^{Directed}(\Delta t_n) = 6D_{3D}\Delta t_n + (V\Delta t_n)^2 + 6\sigma^2, \tag{2.13}$$

where σ is the average localization precision [77]. For this model, the estimation of the diffusion coefficient is carried out again by fitting the Equation 2.13 to the plot of MSD versus Δt_n. Here the time increment is chosen to be $n = 1, ..., 10$.

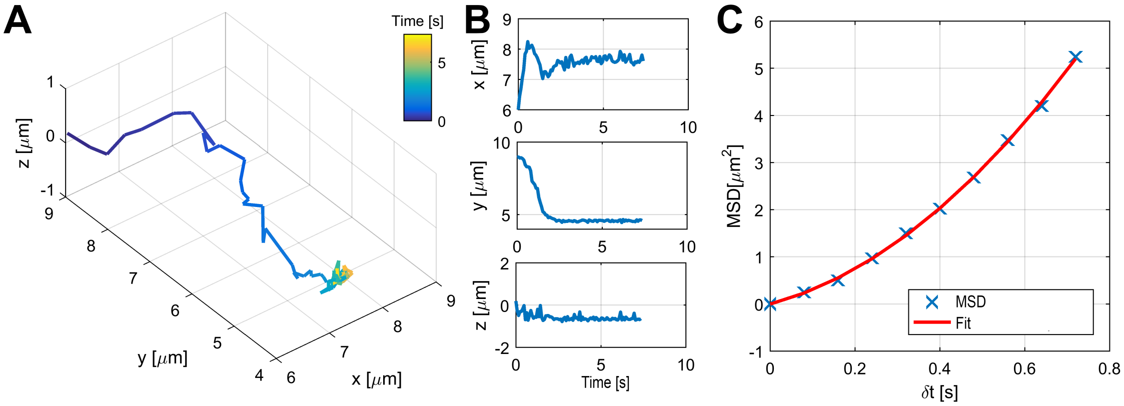

Figure 2.13: An example of three-dimensional directed diffusion analysis. (A) Directed diffusive motion of a single molecule is identified from the MUM-module. (B) The X, Y and Z trajectories of (A) are plotted against time. (C) The trajectory is analyzed using the MSD analysis with the directional diffusion model.

Figure 2.13A shows an example of 3D single molecule trajectory with directed diffusion. The trajectory travels over 6 μm within 2 seconds with highly directed motion (see Figure 2.13B for a detailed view into X, Y and Z direction over time). We obtain MSDs of the trajectory using Equations 2.11 and 2.13 (Figure 2.13C).

2.4.1.4 Unconstrained diffusion on a sphere

To investigate the diffusion of single molecules on the inner membrane of a sphere, we compute the MSD for a series of three-dimensional track coordinates $(x(k), y(k), z(k)), k = 1, ..., N$, captured in N frames as

$$MSD_{Sphere}(\Delta t_n) = \frac{1}{N-1-n} \sum_{j=1}^{N-1-n} (r \times \alpha(j\delta t + n\delta t, j\delta t))^2, \tag{2.14}$$

where $\Delta t_n = n\delta t$ with the frame time δt, n is the time increment and α is the angle between two coordinates calculated as

$$\begin{aligned} &\alpha(j\delta t + n\delta t, j\delta t) = \\ &\arctan\left(\frac{|[x(j\delta t + n\delta t), y(j\delta t + n\delta t), z(j\delta t + n\delta t)][x(j\delta t), y(j\delta t), z(j\delta t)]^T|}{[x(j\delta t + n\delta t), y(j\delta t + n\delta t), z(j\delta t + n\delta t)][x(j\delta t), y(j\delta t), z(j\delta t)]^T}\right). \end{aligned} \tag{2.15}$$

Since the displacement is on the surface of the sphere, i.e. two-dimensional distance, the measurement of the diffusion coefficient is carried out by fitting a linear function to the plot of MSD versus Δt_n of Equation 2.10. The time increment is chosen to be $n = 1, ..., 5$ [78].

Figure 2.14A shows an example of a simulated track that diffuses on a spherical surface. MSDs of the track are obtained using Equation 2.14 and a linear function is fitted following Equation 2.10 (Figure 2.14B). We evaluate this method in Section 2.4.2.

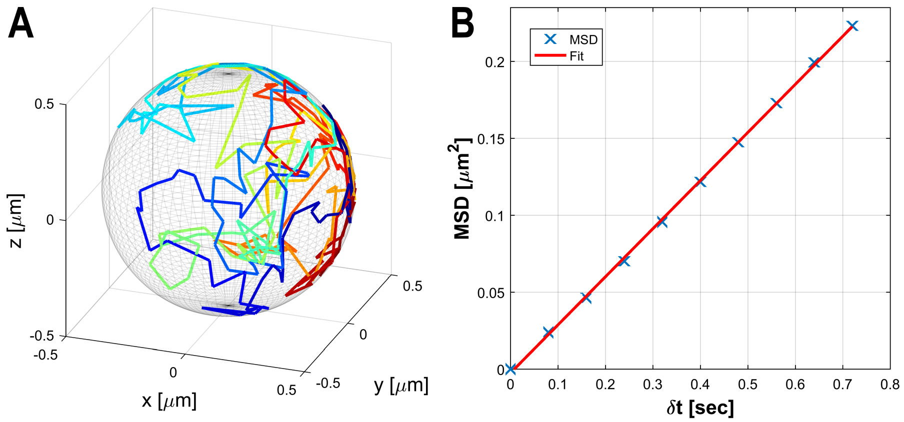

Figure 2.14: Spherical diffusion analysis. (A) A trajectory is simulated that diffuses on a spherical surface. (B) The trajectory from (A) is analyzed using MSD analysis with the spherical diffusion model.

2.4.2 Spherical diffusion model

2.4.2.1 Simulation of spherical diffusion model

The simulation of a trajectory on a spherical surface is carried out according to the following steps. We first create a point on the sphere and find a plane orthogonal to the sphere at that point. We then simulate the point of a trajectory on this orthogonal plane. Now the trajectory consists of two coordinates, i.e., the first coordinate at the point on the sphere and the second coordinate on the orthogonal plane. We consider the second coordinate as a reference point. Next, we find a point on the sphere surface that is the closest to the reference point. Here we assume that the distance between the new point and the reference point is very small. The process is repeated by now finding a plane orthogonal to the sphere at the new point. By repeating these steps, we simulate a diffusion trajectory on the surface of the sphere. Figure 2.14 shows an example of the simulation. The diffusion coefficients of the simulated tracks are measured as described in Section 2.4.1.4. The method is verified using a set of simulations (see Section 2.4.2.2).

2.4.2.2 Verification of spherical diffusion model

To verify the diffusion measurement approach described in Section 2.4.1.4, we establish a set of simulations (see Section 2.4.2.1 for the simulation method). A stimulated trajectory is associated with a simulated diffusion coefficient, D_S [µm^2/s], a sampling time, T [s], a sphere size, R [µm], a track length, N [#] and a measured diffusion coefficient from the simulated track, D_M [µm^2/s]. We create a set of simulated trajectories with parameters, $D_S = \{0.01, 0.21, 0.41, 0.61, 0.81\}$, $T = \{10^{-4}, 10^{-6}, 10^{-8}, 10^{-10}\}$, $R = \{0.1, 0.4, 0.7, 1.0, 1.3, 1.6\}$ with $N = 1500$. Diffusion coefficients D_M are measured and the results are shown in Figures 2.15 to 2.17. For each simulation condition, 1000 trajectories are simulated and the means and standard deviations are plotted as lines and error bars, respectively.

Figure 2.15 shows the simulated diffusion coefficients (D_S x-axis) against the measured diffusion coefficients (D_M, y-axis) in different simulated conditions. Ideally, simulated and measured diffusion coefficients are equal ($D_S = D_M$). In summary, the diffusion measurements show a larger error when 1) sphere size is small, 2) sampling rate is high, and 3) simulated diffusion coefficient is large. Especially, the sampling rate affects the measurement error.

We therefore plot the diffusion coefficient measures (D_M, y-axis) against the sampling rate (T, x-axis). As expected, larger sampling times produce a larger error. With a large sampling time, we notice that the error is significant when the sphere size is small.

Figure 2.17 visualizes the diffusion coefficient measures (D_M, y-axis) against the sphere size (R, x-axis). With the given simulation conditions, the diffusion coefficient measures are always accurate if 1) sampling time is less than 10^{-4} s or the sphere

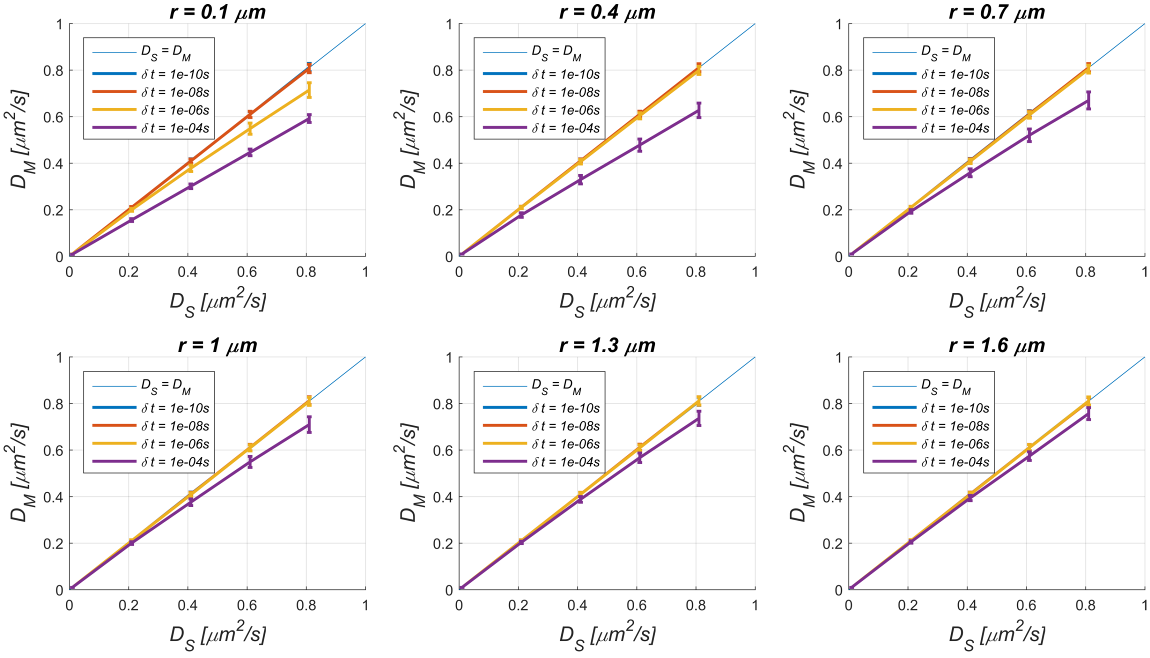

Figure 2.15: Verification of the MSD analysis with the spherical diffusion model of different sampling rates. Measured diffusion rates are plotted against simulated diffusion rates. Each plot shows the simulation and measurements for different sphere sizes.

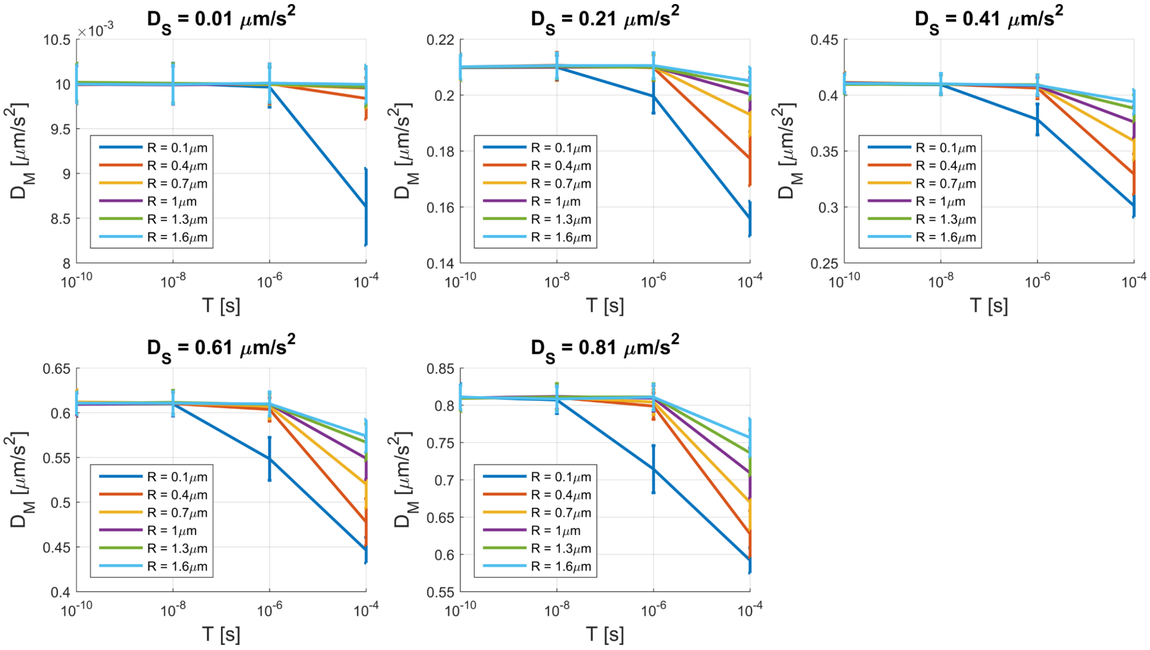

Figure 2.16: Verification of the MSD analysis with the spherical diffusion model for different sphere sizes. Measured diffusion rates are plotted against sampling rates. Each plot shows the simulation and measurements under different simulation conditions.

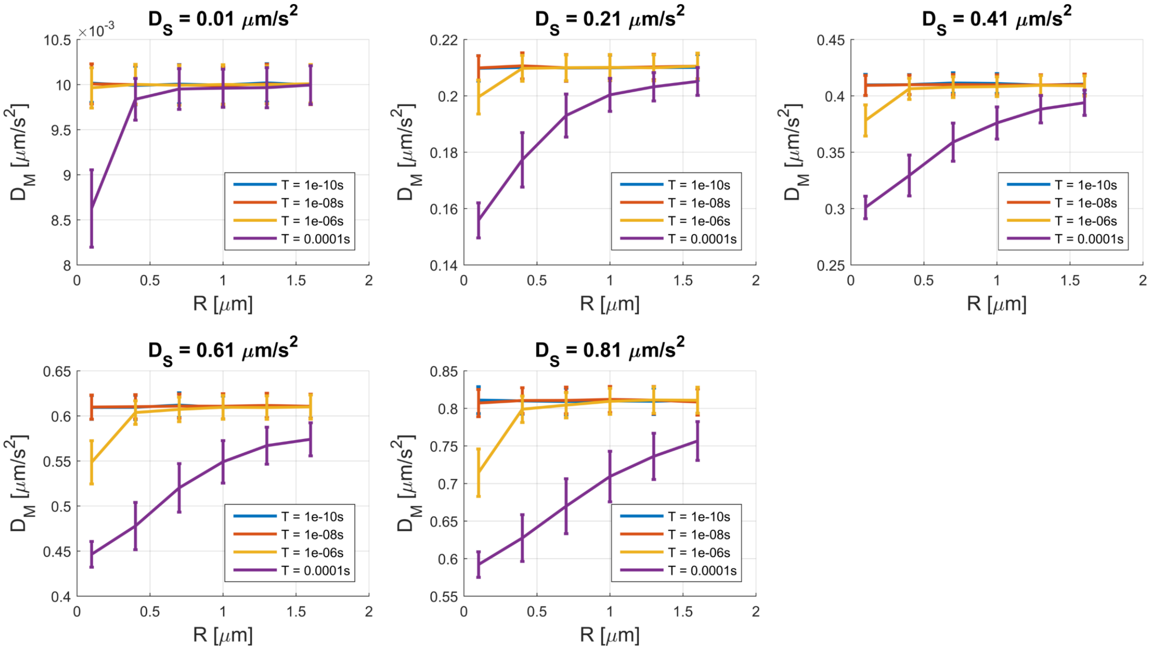

Figure 2.17: Verification of the MSD analysis with the spherical diffusion model for different simulation conditions. Measured diffusion rates are plotted against sphere sizes. Each plot shows the simulation and measurements under different simulation conditions.

size is larger than 0.1 µm.

2.4.3 Probability distribution of square displacement analysis

We analyze multi-stage diffusion dynamics of a single molecule using the probability distribution of square displacement (PDSD) analysis [79, 80]. Here we extend the analysis to support three-dimensional trajectories as well as two-dimensional tracks. For a single molecule trajectory of the unconstrained diffusion in two-dimensional or three-dimensional space, the PDSD of this trajectory is given by

$$P(r^2, \tau) = 1 - e^{-r/kD\tau}, \tag{2.16}$$

where r^2 denotes the square displacement, τ denotes the time lag, D is the diffusion coefficient and $k = 4$ for a two-dimensional track or k=6 for a three-dimensional track. If a trajectory has n different diffusion dynamics, the PDSD of the trajectory is given by

$$P(r^2, \tau) = 1 - \sum_{i=1}^{n} \alpha e^{\frac{-r}{kD_i\tau}}, \sum_{i=1}^{n} \alpha_i = 1, \tag{2.17}$$

where r^2 denotes the square displacement, τ denotes the time lag, α_i denotes the fraction of i^{th} diffusion motion, D_i is the diffusion coefficient of i^{th} diffusion motion, and $k = 4$ for a two-dimensional track or $k = 6$ for a three-dimensional track. A normalized cumulative histogram of the square displacements of a track is fitted, using the nonlinear least squares algorithm, to the distribution function in Equation 2.17 with 160 µs time lag with two diffusion rates ($n = 2$). To compare the performance of PDSD for the single diffusion case, the measured displacement data is fitted to Equation 2.16.

Figure 2.18 demonstrates a PDSD analysis with simulations. We simulate a

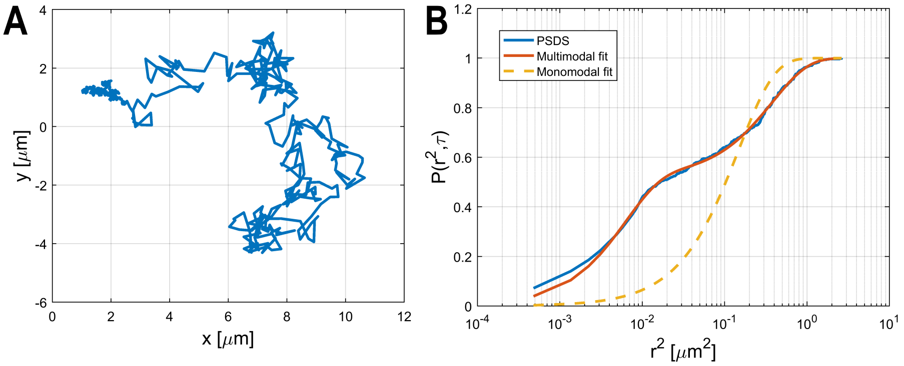

Figure 2.18: Demonstration of the probability distribution of square displacement (PDSD) analysis with a simulated trajectory. (A) A trajectory is simulated by combining two trajectories that are simulated with two different diffusion rates. (B) The trajectory in (A) is tested using PDSD analysis.

track $T = \{(x_n, y_n) \in \mathbb{R}^2 | n = 1, ..., N, N+1, ..., 2N\} = T_1 \cup T_2$ with two subsets $T^1 = \{(x_n, y_n) | n = 1, ..., N\}$ and $T^2 = \{(x_n, y_n) | n = N+1, ..., 2N\}$. Here T^1 and T^2 are sets of coordinates in two-dimensional space from unconstrained diffusive motion. In particular for Figure 2.18A, the diffusion rates of T^1 and T^2 were $D^1 = 0.01$ μm^2/s and $D^2 = 0.6$ μm^2/s respectively. Using the PDSD analysis described above, we evaluate the PDSD of T and fit Equation 2.17 with $n = 2$. Two diffusive motions are measured with diffusion rates, $\hat{D}^1 = 0.0096$ μm^2/s (48.05%), $\hat{D}^2 = 0.5983$ μm^2/s (51.95%). Percentages denote the contributions of the diffusive motions within the trajectory.

2.4.4 Cellular structure approximation and trajectory compensation

2.4.4.1 Organelle approximation

Understanding single molecule dynamics in the context of the surrounding cellular structures is an important aspect of rMUM. Examining the behavior of a single molecule as it interacts with organelles of the endocytic pathway such as sorting endosomes, multivesicular bodies, and lysosomes is of particular interest.

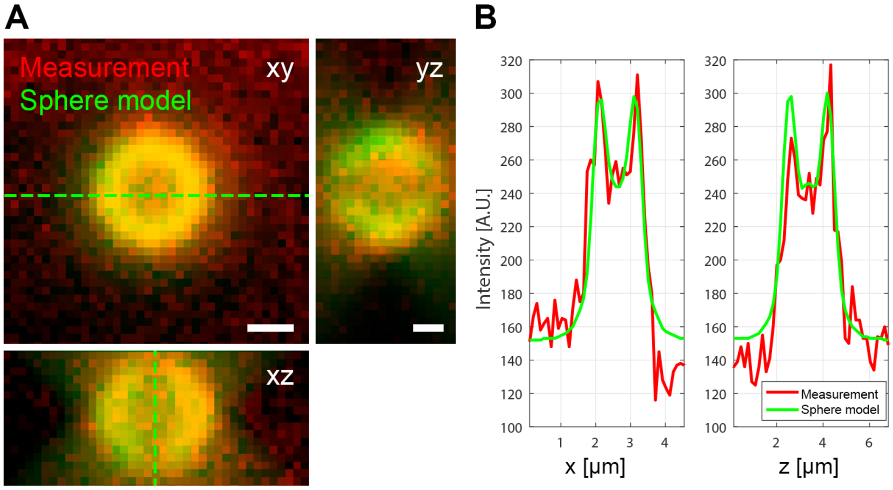

Figure 2.19: Approximation of a sorting endosome by a sphere. (A) An endosome labeled with eGFP-FcRn in a 22Rv1 cell is imaged using the r-module (red, measurement) and is fitted into the sphere model (green). (B) Intensities along the green dotted lines in (A) are plotted. Scale bar: (A) 500 nm.

To understand such dynamics, it is necessary to have mathematical descriptions of not only the single molecule, but also of the organelles. We found that the limiting membrane of the organelles can be well approximated by a spherical shell. Figure 2.19A shows a set of z-stack images of a sorting endosome labeled with FcRn–eGFP in a 22Rv1 cell (red). Here we fit a 3D sphere model with a 10 nm thick shell [81]. The realization of the z-stack images of the 3D sphere model is carried out by convolving with the Born and Wolf point spread function model [64]. The 3D sphere model is fit to the data using the maximum likelihood estimator (see Figure 2.19A, green channel, Scale bar: 500 nm.) [34]. Figure 2.19B shows intensities along the center lines of images in Figure 2.19A.

The sphere fitting method allows good approximation of the organelle structure. However, the fitting process is computationally extremely expensive, and therefore it is not suitable for analyzing organelle images from the rMUM. We found an alternative way to approximate the spherical organelle structure using the Hough transform [82]. We first create maximum intensity projection images of the z-stack images of the organelle onto the x-y, y-z and x-z planes. From each projection, center coordinates with radius information are extracted by applying the Hough transform (using the MATLAB command `imfindcircles`). We take the average of those coordinates and radius measures for the sphere approximation.

To verify the two approaches described above, we evaluated the location and size of 29 sorting endosomes. The average difference in estimates between the two approximation methods were 0.054 µm, 0.069 µm and 0.074 µm for the x-coordinate, y-coordinate and z-coordinate for the location of the approximating sphere and 0.029 µm for its diameter.

2.4.4.2 Trajectory compensation

The organelle approximation described in Section 2.4.4.1 together with the single molecule trajectory provides complete information of the single molecule dynamics in its context. This allows for the examination of the behavior of single molecule trajectories in organelles.

Let us assume that we have a single molecule in the sorting endosome. We measure both a single molecule trajectory and an organelle trajectory. The single molecule trajectory in relation to the sorting endosome it interacts with can, therefore, be obtained by subtracting the coordinates of the sorting endosome in time from the single molecule coordinates for each time point. Figure 2.20 visualizes such an approach to show that we are indeed able to understand the single molecule dynamics

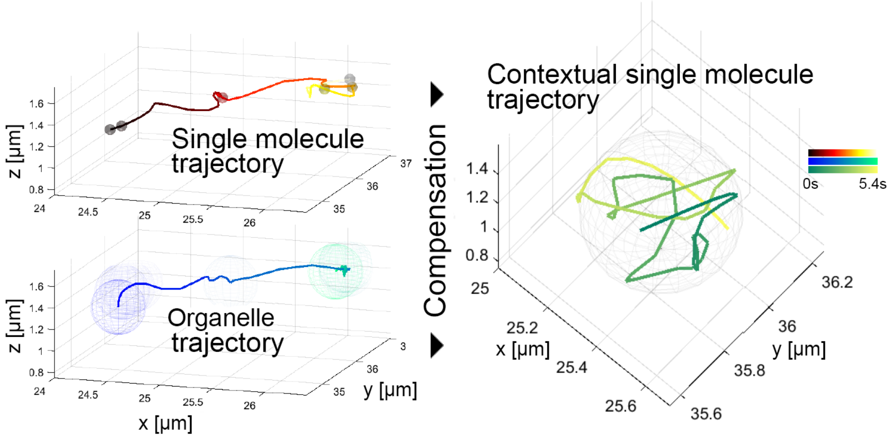

Figure 2.20: An illustration of the trajectory compensation analysis. A single molecule trajectory from the MUM-module with the organelle trajectory from the r-module are compensated for. Here the organelle carries the single molecule. The compensation steps allows for the analysis of the single molecule trajectory in the context of the organelle dynamics.

in the organelle by compensating for external movements.

2.4.5 Automated single molecule tracking

Automated tracking is performed through two steps: frame-to-frame linking and gap closing, as described previously [73, 74]. The frame-to-frame linking is carried out by connecting the nearest-neighbor coordinates in adjacent frames using the Munkres & Kuhn algorithm [75]. Similarly, the gap closing is processed by linking nearest-neighbor trajectories within a certain range of frames using the Munkres & Kuhn algorithm [75].

The automated tracking is performed using custom modules of the software package MIATool.

2.4.6 Co-association analysis

Co-association analysis is used to evaluate the interrelationship between proteins, or between a protein and a cellular structure. The analysis is designed for rMUM single molecule trajectory data with surrounding cellular structure information. We first measure the diffusion rate of the single molecule trajectory using MSD analysis (see Section 2.4.1). Next, we calculate the average distance to the nearest-neighbor proteins or cellular structures along the single molecule trajectory.

From the scatter plot of the diffusion rates and the average distance measures of single molecule trajectories, subgroups may be identified (see Figure 3.15C for an example). These subgroups are analyzed using the k-means clustering algorithm [83]. The number of subsets is defined using the gap statistic approach [84]. The co-association analysis is carried out using MATLAB.

2.4.7 Visualization

The rMUM imaging experiments produce three-dimensional single molecule trajectories or streaks acquired with the MUM-module and multi-color z-stack images acquired with the r-module. After the data processing and analysis described in Sections 2.3 and 2.4, the data need to be properly visualized. The visualization involves the display of 3D single molecule trajectory with the surrounding cellular structures.

A single molecule track is composed of a set of 3D coordinates over time. These 3D coordinates can be visualized as a colored trajectory line (see Figure 2.21A). Here color denotes time. The display of the trajectory requires the compensation process described in Section 2.4.4.2 when it is drawn as a still image. Since the still image does not typically show structural dynamics, single molecule trajectories without the compensation step may lead to misinterpretation of the data. Figure 2.21A shows

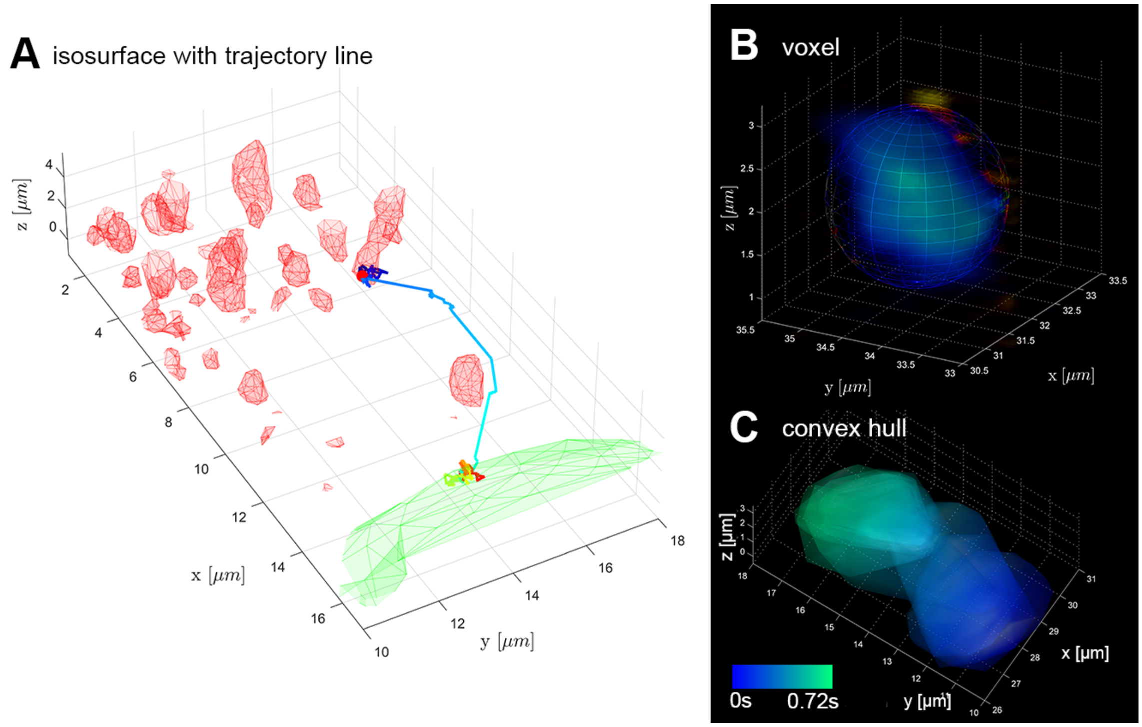

Figure 2.21: Three-dimensional visualization of the rMUM data. (A) 3D single molecule trajectory from the MUM-module is plotted as a 3D line plot and the cellular structures from the r-module are reconstructed using the isosurface method. (B) The cellular structure images from the r-module are visualized using a 3D voxel display. (C) Streaks of a single molecule imaged from the MUM-module are reconstructed using the 3D convex hull approach.

an example of a trajectory after compensation.

In particular, single molecules sometimes appear as “streaks” in different focal planes of the MUM-module. This happens when the single molecule is in a low—viscosity medium like water. The streak cannot be localized properly, so it cannot be shown as a trajectory. The streak signal over MUM images is reconstructed with the convex hull in three-dimensional space (Figure 2.21C).

The 3D volumetric images from the r-module (after the processes described in Section 2.3) can be rendered as a 3D isosurface [85]. The isolevels are obtained using the unimodal thresholding method [86]. Particularly, the cellular membrane structures are averaged normal to the surface. 3D rendering of the isosurface is carried out using dual contouring polygonization of the isosurface. Figure 2.21A shows an example of the isosurface visualization.

The 3D voxel-based rendering is an alternative approach to 3D volumetric image rendering [87]. The processed volumetric images form an isotopic volumetric grid. For each volume pixel, i.e. voxel, the color and transparency are given based on the image intensity. Figure 2.21B shows an example of 3D voxel rendering.

All 3D figures and videos were rendered using MATLAB (The Mathworks) and OpenGL.

3. THREE-DIMENSIONAL SINGLE PARTICLE TRACKING IN CELLULAR CONTEXT

3.1 Introduction

Prostate specific membrane antigen (PSMA) is an important biomarker for prostate cancer cells and as such is an important therapeutic target for antibody-based therapies [43, 88, 89, 90]. For example, of particular interest are PSMA-specific antibodies that are conjugated with cytotoxic drugs, so-called antibody drug conjugates (ADCs). To decrease non-specific toxicity, a critical part of their design is that the toxin is only released at specific conditions such as the reducing or proteolytic environment that is present in the lysosome [32, 33]. Therefore, understanding the precise pathway to late endosomes and lysosomes for PSMA-specific antibodies is of major importance for the appropriate functioning of ADC therapy. We therefore analyzed the pathway of a PSMA-specific antibody from before the initial binding to PSMA at the cell membrane until the trafficking into a lysosome. This section describes a study of PSMA-specific antibody trafficking in prostate cancer cells using rMUM. The organization of this section is as follows. Section 3.2 deals with the materials and methods used in the PSMA trafficking study including rMUM imaging experiments and control experiments to support the results. In Section 3.3, we closely examine the trafficking of PSMA-specific antibodies.

3.2 Materials and methods

This section deals with materials and methods for carrying out the experiments discussed in Section 3.3.

3.2.1 Reagents and antibodies

QDot® 655 streptavidin conjugate, 0.1 µm TetraSpeck™microspheres, cholera toxin B subunit Alexa Fluor® 555 conjugate, transferrin Alexa Fluor® 647 conjugate and all secondary antibody conjugates were purchased from Invitrogen (Carlsbad, CA). Mouse monoclonal anti-Early Endosome Antigen 1 (EEA-1) antibody was purchased from BD Biosciences (San Jose, CA). Mouse anti-human Lysosomal-Associated Membrane Protein 1 (LAMP-1) antibody was purchased from the Developmental Studies Hybridoma Bank (DSHB; Iowa City, IA). Paraformaldehyde, glutaraldehyde and all chemicals and reagents for transmission electron microscopy were purchased from Electron Microscopy Sciences (Hatfield, PA).

3.2.2 Cell culture

The human prostate carcinoma epithelial cell line 22Rv1 (ATCC; Manassas, VA) was maintained in RPMI-1640 (Lonza; Basel, Switzerland) supplemented with 10% FCS (HyClone; Logan, UT). For imaging studies, the culture medium was changed to the imaging medium comprised of phenol-red free RPMI-1640 (Invitrogen) supplemented with 10% FCS (HyClone) that had been depleted of Immunoglobulin G (IgG) [61].

3.2.3 Expression constructs

The following expression constructs were used: enhanced green fluorescent protein–neonatal Fc receptor (eGFP–FcRn), monomeric red fluorescent protein–FcRn (mRFP–FcRn), aequorea coerulescens green fluorescent protein–neuromodulin (AcGFP–MEM), LAMP-1–mRFP, eGFP–clathrin light chain (eGFP–CLC), and β2–microglobulin (β2m).

The gene encoding rat LAMP-1 was recloned from an expression plasmid encoding LAMP-1–GFP (rat) (a generous gift of Prof. P. Luzio, University of Cambridge) into mRFP–N1 as an EcoRI fragment using standard methods as described previously [36]. The mRFP gene [91] was generously provided by R. Tsien (UCSD, CA). The AcGFP–MEM construct was purchased from Clontech (Mountain View, CA). eGFP–FcRn, mRFP–FcRn, eGFP–CLC and human β2m constructs have been described previously [36, 61, 92, 93]. All FcRn–fluorescent protein constructs used in the present study contain a mutated variant of human FcRn ('D132N-E135Q-H166A') that has been engineered using standard methods so that the encoded FcRn does not bind to IgG or albumin [27, 61].

3.2.4 Transfection

22Rv1 cells were transfected with two different combinations of expression plasmids for use in fluorescence microscopy experiments, as follows: 1) eGFP–FcRn, human β2m, and LAMP-1–mRFP; 2) mRFP–FcRn, human β2m and AcGFP–MEM; 3) mRFP–FcRn, human β2m and eGFP–CLC. The transfections were carried out using the Amaxa Nucleofector technology (Lonza) with solution V and program X-001. To ensure that expression of fluorescently labeled human FcRn/human β2m, MEM, CLC and LAMP-1 did not affect intracellular trafficking (recycling) pathways, flow cytometry experiments were performed to study the transferrin recycling rate using 22Rv1 cells transfected with eGFP–FcRn, AcGFP–MEM, eGFP–CLC or LAMP-1–mRFP as described previously [93]. The flow cytometry assay and the results are described in Sections 3.2.11 and 3.3.2.

3.2.5 Site-specific biotinylation of PSMA-specific antibody and quantum dot labeling

The genes encoding the heavy and light chain variable domains of the PSMA-specific antibody, 026, were synthesized with GenScript and used to generate full-length heavy (human IgG1) and light (kappa) chain expression constructs using the expression vector pcDNA3.4-TOPO. Codons encoding a biotinylation signal peptide (Bsp) sequence were appended to the carboxy terminus of the CH3 domain using standard methods of molecular biology [94]. The antibody was expressed and purified from culture supernatants of HEK cells using protein G-Sepharose. Then, the antibody was site-specifically biotinylated with BirA as previously described [55]. The expressed protein was further purified via size exclusion chromatography to remove aggregates. Quantum dot labeled PSMA-specific antibody (QD-αPSMA) was prepared by mixing the site specific biotinylated PSMA-specific antibody with streptavidin-coated QDot® 655 at a ratio of 1:50 antibody:QD. The mixture was incubated for 10 minutes at room temperature and was then diluted with imaging medium. For use as a control to assess non-specific binding, site-specifically biotinylated hen egg lysozyme-specific antibody, HuLys10 [55, 94], was used. Biotinylated HuLys10 was coupled to streptavidin-coated QDot® 655 using the same approach as for the PSMA-specific antibody.

3.2.6 Live cell imaging experiment using rMUM

Live cell imaging experiments were carried out using the rMUM setup equipped with a microscope incubation system (Okolab; Pozzuoli NA, Italy) and an objective warmer (Bioptechs; Butler, PA) to maintain the temperature at 37°C with 5% CO_2 and 95% humidity.

The live cell samples for Sections 3.3.6, 3.3.7 and 3.3.9 were prepared as follows: 22Rv1 cells were transfected with mRFP–FcRn, human β2m and MEM–AcGFP and incubated with QD-αPSMA (at a concentration of 550 pM with respect to antibody) for 5 minutes at room temperature. The cells were washed once with pre-warmed (37°C) imaging medium and subsequently imaged using the rMUM setup. The MUM-module was configured with four distinct focal planes with spacings between planes of 0.642, 0.637 and 0.675 µm (see Figure 2.6). The acquisition rate of the MUM-module was 12.5 stacks of four simultaneously acquired images per second. The r-module was configured to acquire z-stack images at a 0.3 µm step size with 12 frames per stack. These images were obtained at a rate of 50 frames per second (FPS) with two channels; therefore, 2 volumes were obtained per channel per second.

The live cell samples for Section 3.3.8 were prepared as follows: 22Rv1 cells were transfected with MEM–AcGFP and incubated with QD-αPSMA (at a concentration of 550 pM with respect to antibody) for 5 minutes at room temperature. Following incubation with QD-αPSMA, the cells were washed once with pre-warmed (37°C) imaging medium and subsequently imaged using the rMUM setup. The MUM-module was configured with four distinct focal planes with spacings between planes of 0.642, 0.637 and 0.675 µm (see Figure 2.6). The acquisition rate of the MUM-module was 12.5 stacks of four simultaneously acquired images per second. The r-module was configured to acquire z-stack images at a 0.2 µm step size with 31 frames per stack. These images were obtained at 25 FPS; therefore, 0.8 volumes were obtained per second.

The live cell samples for Section 3.3.10 were prepared as follows: 22Rv1 cells were transfected with mRFP–FcRn, human β2m and eGFP–CLC and incubated with QD-αPSMA (at a concentration of 550 pM with respect to antibody) for 5 minutes at room temperature. Following incubation with QD-αPSMA, the cells were washed once with pre-warmed (37°C) imaging medium and subsequently imaged using the rMUM setup. The MUM-module was configured with dual–color two focal planes with spacings between planes of 0.612 µm for each channel (see Figure 2.7). The acquisition rate of the MUM-module was 12.5 stacks of four simultaneously acquired images per second. The r-module of the rMUM system was configured to acquire z-stack images at a 0.2 µm step size and 10 frames per stack. These images were obtained at a rate of 25 FPS with two channels; therefore, 2.5 volumes were obtained per channel per second.

The live cell samples for Section 3.3.11 were prepared as follows: 22Rv1 cells were transfected with eGFP–FcRn and human β2m and incubated with QD-αPSMA (at a concentration of 550 pM with respect to antibody) for 10 minutes at 37°C. The cells were washed once with pre-warmed (37°C) imaging medium. The sample was incubated for 10 minutes at 37°C and then imaged using the rMUM setup. The r-module of the rMUM system was configured to acquire z-stack images at a 0.2 µm step size and 24 frames per stack. These images were obtained at a rate of 50 FPS with two channels, therefore, one volume was obtained per channel per second. The MUM-module is configured with four distinct focal planes with spacings between planes of 0.642, 0.637 and 0.675 µm (see Figure 2.6). The acquisition rate of the MUM-module was 12.5 stacks of four simultaneously acquired images per second.

The live cell samples for Section 3.3.12 were prepared as follows: 22Rv1 cells were transfected with eGFP–FcRn and human β2m and incubated with QD-αPSMA (at a concentration of 550 pM with respect to antibody) for 10 minutes at 37°C. The cells were washed once with pre-warmed (37°C) imaging medium. The sample was incubated for 30 minutes at 37°C and then imaged using the rMUM setup. The r-module of the rMUM system was configured to acquire z-stack images with a 0.2 µm step size and 24 frames per stack. These images were obtained at a rate of 50 FPS with two channels, therefore, one volume was obtained per channel per second. The MUM-module was configured with four distinct focal planes with spacings between planes of 0.642, 0.637 and 0.675 µm (see Figure 2.6). The acquisition rate of the MUM-module was 12.5 stacks of four simultaneously acquired images per second.

3.2.7 Data processing

The data from rMUM consists of complex multi-dimensional images and needs to be processed carefully for analysis and visualization. Details of rMUM data processing are described in Section 2.3. Here we discuss the overall process flow for rMUM data.

Two three-dimensional image spaces exist in the r- and the MUM-module, and they need to be registered spatially. Spatial registration is performed using calibration data, which is obtained by imaging a 3D bead sample using rMUM as described in Section 2.3.2. The beads are imaged both in the r- and the MUM-module simultaneously. Using the MUMLA described in Section 2.3.1, precise 3D locations of the beads are identified in the MUM-module. Similarly, bead images from the r-module are processed using the MUMLA algorithm with slight modifications (see Section 2.3.1.1). Using two sets of 3D coordinates from the r- and the MUM-module, an affine transformation between two modules is estimated using a generalized least squares algorithm [67]. The affine transformation is applied to single molecule trajectories from the MUM-module, and consequently, the MUM-module data is registered to the r-module data. The details of the spatial registration process are described in Section 2.3.2.

The r- and the MUM-module operate at different sampling rates, i.e., the r-module acquires images 2 to 4 times faster than the MUM-module in practice.

Therefore, data from two modules need to be temporally registered. The temporal registration is carried out by interpolating images from the r-module. 3D deconvolution is applied to the r-module data using the Richardson-Lucy algorithm [70, 71]. The details for temporal registration and the deconvolution process are described in Sections 2.3.3 and 2.3.4.

3D locations of single molecules imaged with the MUM-module are identified using the MUMLA algorithm. Details of the MUMLA process are described in Section 2.3.1. Single molecules diffusing in the cell exterior appear as "streaks" in MUM images (see Figures 3.9 and 3.11). The traces of single molecules are shown in different focal plane images. The probable location of the molecule is visualized by the three-dimensional convex hull (see Figure 3.10). More details are described in Sections 2.3.1 and 2.4.7.

3.2.8 Data analysis

Single molecule trajectories from the rMUM are analyzed using diffusion analysis. The diffusion coefficient of the single molecule in two or three dimensions is measured using mean square displacement (MSD) analysis (see Sections 2.4.1.1 and 2.4.1.2). Single molecule tracks with directed motion are also analyzed similarly using MSD analysis with a directed diffusion model (see Section 2.4.1.3).

One benefit of the rMUM modality is that both single molecule trajectories and cellular structure are imaged simultaneously. Therefore, single molecule dynamics can be understood in the context of cellular structures. We established a method to analyze single molecules in organelles such as sorting endosomes, multivesicular bodies, and lysosomes. The organelles in the cell are not stationary. Therefore, the single molecule dynamics within the organelle present a mix of complex dynamics from both the molecule and the organelle. Here the organelle is approximated well as a sphere, so the single molecule dynamics within the organelle can be extracted by compensating for the organelle motion (see Section 2.4.4). In the case where a single molecule appears on the limiting membrane of the organelle, spherical diffusion dynamics are modeled (see Section 2.4.1.4).

Single molecule trajectories consist of complex dynamics, and multiple diffusion behaviors are often observed within a track. Such trajectories are analyzed using the probability distribution of square displacement analysis [79] with modifications for three-dimensional trajectory analysis (see Section 2.4.3).

The identification of single molecule trajectories is carried out using an automated tracking analysis method [73, 74, 75]. The co-associations of single molecule trajectories and cellular structure are also evaluated using the nearest neighbor algorithm (see Section 2.4.6).

The normality of all statistical data is tested using the Kolmogorov-Smirnov test (MATLAB `kstest` command) with a significance of 5%. Data visualization of rMUM data is carried out by the combination of surface display of cellular structure superimposed with the 3D single molecule trajectory (see Section 2.4.7).

3.2.9 Transmission electron microscopy

22Rv1 cells were treated with QD-αPSMA (at a concentration of 550 pM with respect to antibody) for 40 minutes at 37°C. Following washing with PBS, the cells were fixed using 4% paraformaldehyde with 0.2% glutaraldehyde for 12 hours at 4°C. The cells were then washed five times at room temperature with 0.05 M maleate buffer supplemented with 0.5 mM $CaCl_2$ and 2% sucrose and incubated with 1% uranyl acetate in maleate-sucrose for 1 hour. The cells were dehydrated by incubation in 50% ethanol for 8 minutes at room temperature. The dehydration process was then continued stepwise using 70, 80, 90, 95 and 100% ethanol for 8 minutes for each ethanol concentration at room temperature. The cells were then subjected to an infiltration process using ethanol and LR White at ratios of 2:1 (ethanol:LR white) and 1:2 (ethanol:LR white) for 30 minutes each sequentially, and then three times with 100% LR White for 3 hours each time. The cells in LR White were polymerized for 16 hours at 50°C, and ultra-thin sections were obtained using a ultramicrotome. The sections were placed on the nickel grids and were treated with R–Gent SE–EM silver enhancement reagents (Aurion; Wageningen, Netherlands) to visualize QDs according to the manufacturers instructions. The sections were sequentially stained with 2% uranyl acetate and Reynolds lead citrate for 30 seconds at room temperature and imaged using an FEI Morgagni transmission electron microscope with an acceleration voltage of 80 keV. Transmitted electron micrograms were acquired using a side mounted charge coupled device (CCD) camera (Olympus Soft Imaging Solutions; Münster, Germany), and magnification was calibrated using a grating replica (80051; EMS). The acquired data were processed for display using the software package MIATool [95].

3.2.10 Immunofluorescence microscopy

22Rv1 cells were plated on glass coverslips, cultured for 36 hours and cooled down for 10 minutes by incubation on ice. Cells were incubated with QD-αPSMA (at a concentration of 5.5 nM with respect to antibody) for 30 minutes on ice, washed twice with PBS at room temperature and incubated with pre-warmed phenol-red free RPMI-1640 medium supplemented with 10% FCS (IgG depleted) for different times at 37°C. The cells were fixed with 3.4% paraformaldehyde and permeabilized with

0.02% saponin, each for 10 minutes at room temperature. Fixed and permeabilized cells were treated with 4% bovine serum albumin, stained with primary antibodies and incubated with goat serum prior to counter-staining with secondary antibody conjugates. Each incubation step was for 25 minutes at room temperature, and cells were washed with PBS between each step. The cells were imaged using a Zeiss Axiovert 200M widefield epifluorescence microscope with filter sets (Chroma Technologies; Battlebro, VT) specific for eGFP/Alexa Fluor® 488 (filter set # 41017), mRFP/Alexa Fluor® 555 (filter set # 41002b), Alexa Fluor® 647(filter set # 41008) and QD 655 (filter set # 39107).

3.2.11 Flow cytometry assay

For flow cytometry experiments [96], transfected and untransfected 22Rv1 cells were plated in 24 well plates. Following 36 hours of culturing, cells were pulsed with 10 µg/mL Alexa Fluor® 647–labeled transferrin in phenol red–free RPMI-1640 medium supplemented with 10% FCS (IgG-depleted) for 60 minutes at 37°C in a 5% CO_2 incubator, washed, and then chased in the medium containing 1 mg/mL unlabeled holo-transferrin for varying times up to 30 minutes. After each chase period, cells were washed with ice-cold phosphate-buffered saline (PBS) and removed from the wells by trypsinization. Cells were then washed with medium and analyzed by flow cytometry on an LSRFortessa or Accuri C2 (Becton Dickinson; Franklin Lakes, NJ). Data were analyzed using FlowJo (FlowJo, LLC; Ashland, OR). The results are discussed in Section 3.3.2.

3.3 Prostate specific membrane antigen trafficking in the prostate cancer cells

PSMA is an important therapeutic target for antibody-based therapies [43, 88, 89, 90]. Here the success of such therapy requires the understanding of intracellular trafficking for PSMA. In this section, we first verify the experimental methods and models via control experiments (Sections 3.3.1 to 3.3.5). Sections 3.3.6 to 3.3.12 depict PSMA-specific antibody trafficking in 22Rv1 cells in detail.

3.3.1 Specific binding of the PSMA-specific antibody quantum dot conjugates in prostate cancer cells

PSMA-specific antibody production and quantum dot conjugation assay are described in Section 3.2.5. Ideally, only QD-αPSMA should bind to PSMA on prostate cancer cells. To verify this specificity, we analyze the binding activities of QD-αPSMA, quantum dot without PSMA-specific antibody (QD), and anti-hen egg lysozyme antibody (HuLys10) QD complexes (QD-HuLys10) to 222Rv1 cells.

Figure 3.1 shows specific binding of QD-αPSMA to PSMA on 22Rv1 cells at two different temperatures: on ice and at 37°C. For Figure 3.1A, 22Rv1 cells were cooled for 10 minutes by incubation on ice. Cells were incubated with QD-αPSMA, QD-HuLys10 or QD for 30 minutes on ice, washed twice with ice-cold PBS and fixed with 3.4% paraformaldehyde on ice for 10 minutes. For Figure 3.1B, 22Rv1 cells were incubated with QD-αPSMA, QD-HuLys10 or QD at 37°C for 5 minutes, washed twice with pre-warmed PBS and fixed with 3.4% paraformaldehyde at 37°C for 10 minutes. All cells were stained with cholera toxin subunit B (CTxB) Alexa Fluor® 555 conjugate to visualize the cell membrane. The intensity of images for the QD channel (QD-αPSMA, QD-HuLys10, and QD) was equally adjusted. Both on ice and at 37°C, QD-αPSMA is shown on 22Rv1 cell membrane but no signal

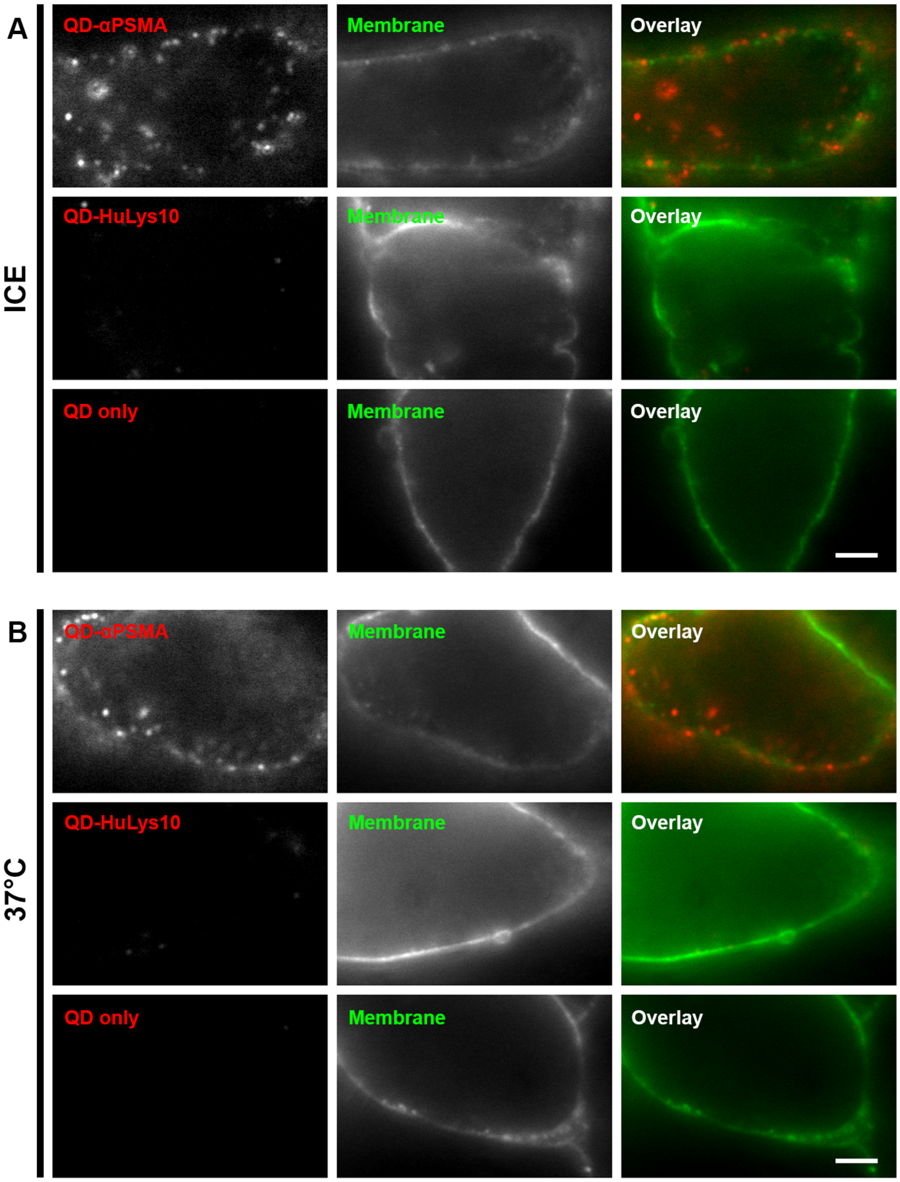

Figure 3.1: The specific binding of QD-αPSMA on 22Rv1 cells. The binding of QD-αPSMA on 22Rv1 cells is highly specific. QD-αPSMA, QD-HuLys10 and quantum dot (QD) alone are incubated with 22Rv1 cells on ice (A) or at 37°C (B). Scale bar: 3 µm.

is detected from QD and QD-HuLys10. This demonstrates specific binding of the PSMA-specific antibody to PSMA, as well as specific conjugation of the quantum dot to the PSMA-specific antibody.

3.3.2 Validation of transfection model

rMUM imaging experiments are carried out by imaging both single molecules and the cellular structure in living cells. To visualize cellular structures such as the cell membrane, clathrin, sorting endosomes, multivesicular bodies and lysosomes, 22Rv1 cells were transfected with AcGFP–MEM, eGFP–CLC, eGPF–FcRn (with human β2m), or LAMP-1–mRFP (see Sections 3.2.3 and 3.2.4 for more details on construct and transfection). However, transfection of plasmid DNA and expression of proteins may cause changes in cellular trafficking behavior in the cell.

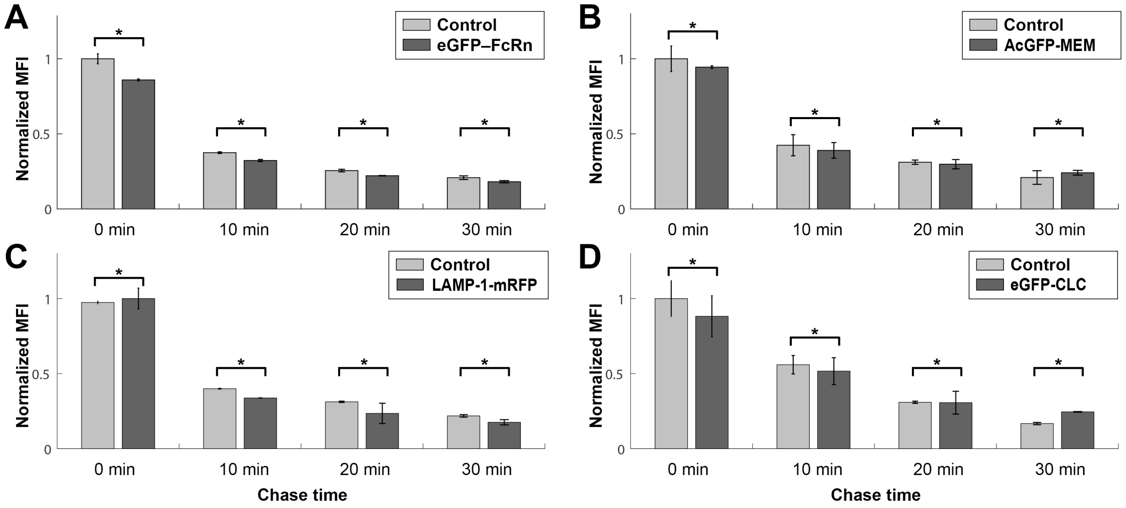

Figure 3.2: Transfections of 22Rv1 cells and transferrin recycling rates. Transfection of 22Rv1 cells with AcGFP–MEM, eGFP–CLC, eGFP–FcRn with β2m or LAMP-1–mRFP does not affect transferrin recycling rates. There were no significant differences in transferrin recycling rates between transfected and untransfected 22Rv1 cells (indicated by *; Student's t–test, $p > 0.01$).

Here we investigate whether that transfection of 22Rv1 cells with AcGFP–MEM, eGFP–CLC, eGFP–FcRn with β2m or LAMP-1–mRFP affects transferrin recycling rates. 22Rv1 cells were transfected with expression constructs encoding AcGFP–MEM, eGFP–CLC, eGFP–FcRn (plus human β2m), or LAMP-1–mRFP and recycling of Alexa Fluor® 647–labeled transferrin is assessed as described in Section 3.2.11. Normalized mean fluorescence intensities (MFIs) of transfected and untransfected 22Rv1 cells for eGFP–FcRn, AcGFP–MEM, LAMP-1–mRFP or eGFP–CLC at different recycling times are indicated. There were no significant differences in transferrin recycling rates between transfected and untransfected 22Rv1 cells, indicating that expression of the those proteins does not affect endosomal trafficking.

3.3.3 Validation of FcRn as a sorting endosome marker

FcRn has been used to label sorting endosomes in living cells [27, 55, 61, 62, 94, 96]. Here 22Rv1 cells are transfected with a mutated variant of human FcRn ('D132N-E135Q-H166A'). This variant is designed not to bind to human IgG1 or albumin.

We first verify that the mutant FcRn labels sorting endosomes in living cells. Figure 3.3 shows 22Rv1 cells transfected with eGFP–FcRn and human β2m. The sample is prepared as described in Sections 3.2.3 and 3.2.4. Cells were fixed with 3.4% paraformaldehyde at 37°C for 10 minutes. The cells were then stained with CTxB–Alexa Fluor® 555 conjugate, and subsequently permeabilized using 0.25% saponin for 10 minutes at room temperature. The cells are treated with 5% bovine serum albumin in phosphate-buffered saline. The cells were stained with mouse monoclonal anti-EEA-1 antibody and Hoechst for 30 minutes at room temperature. The sample was treated with 50–fold diluted goat serum, followed by goat anti-mouse (H+L) antibody–Alexa Fluor® 488 conjugate staining for 30 minutes at room temperature.

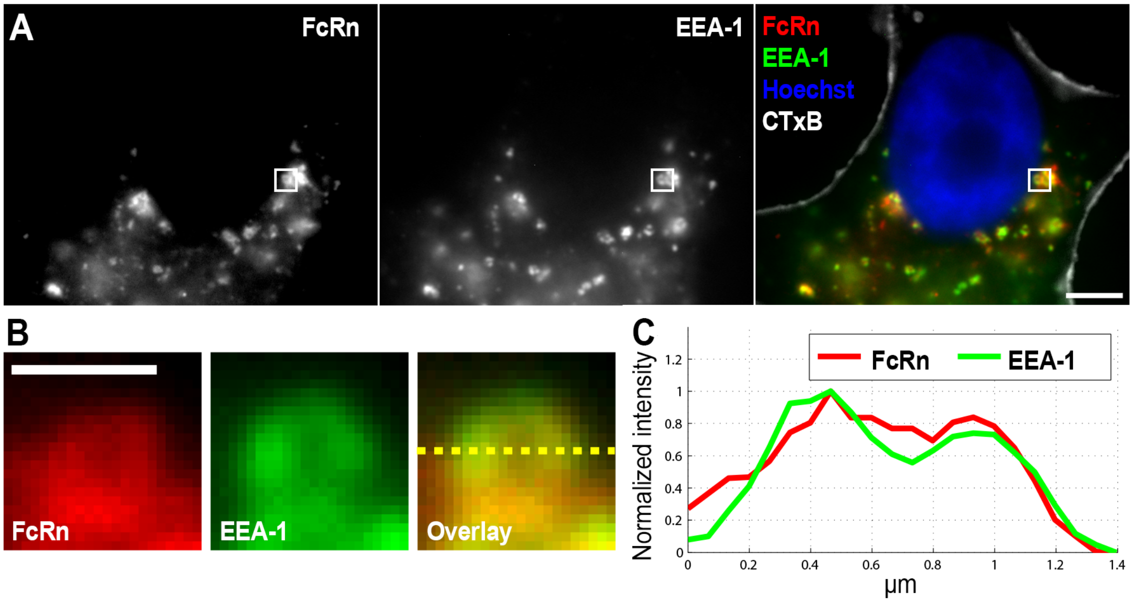

Figure 3.3: Colocalization of EEA-1 and FcRn in 22Rv1 cells. (A) Colocalization between EEA-1 and eGFP–FcRn is observed in 22Rv1 cells. (B) FcRn (red) and EEA-1 (green) signals are shown from a cropped sorting endosome from boxed region (A). (C) Normalized fluorescence intensities along the dotted line in (B) is plotted. Scale bars: (A) 5 μm, (B) 1 μm.

Figure 3.3A shows images of a 22Rv1 cell. FcRn (left), EEA-1 (middle) and overlay of FcRn (red), EEA-1 (green), Hoechst (blue, nucleus) and CTxB (white, cell membrane) are shown. Figure 3.3B shows endosomal compartments in boxed regions of interest of Figure 3.3A. Fluorescence signals corresponding to FcRn and EEA-1 are pseudo-colored red and green, respectively. Normalized fluorescence intensities along the yellow dotted lines in the overlay shown in Figure 3.3B are presented in the fluorescence intensity plots (Figure 3.3C).

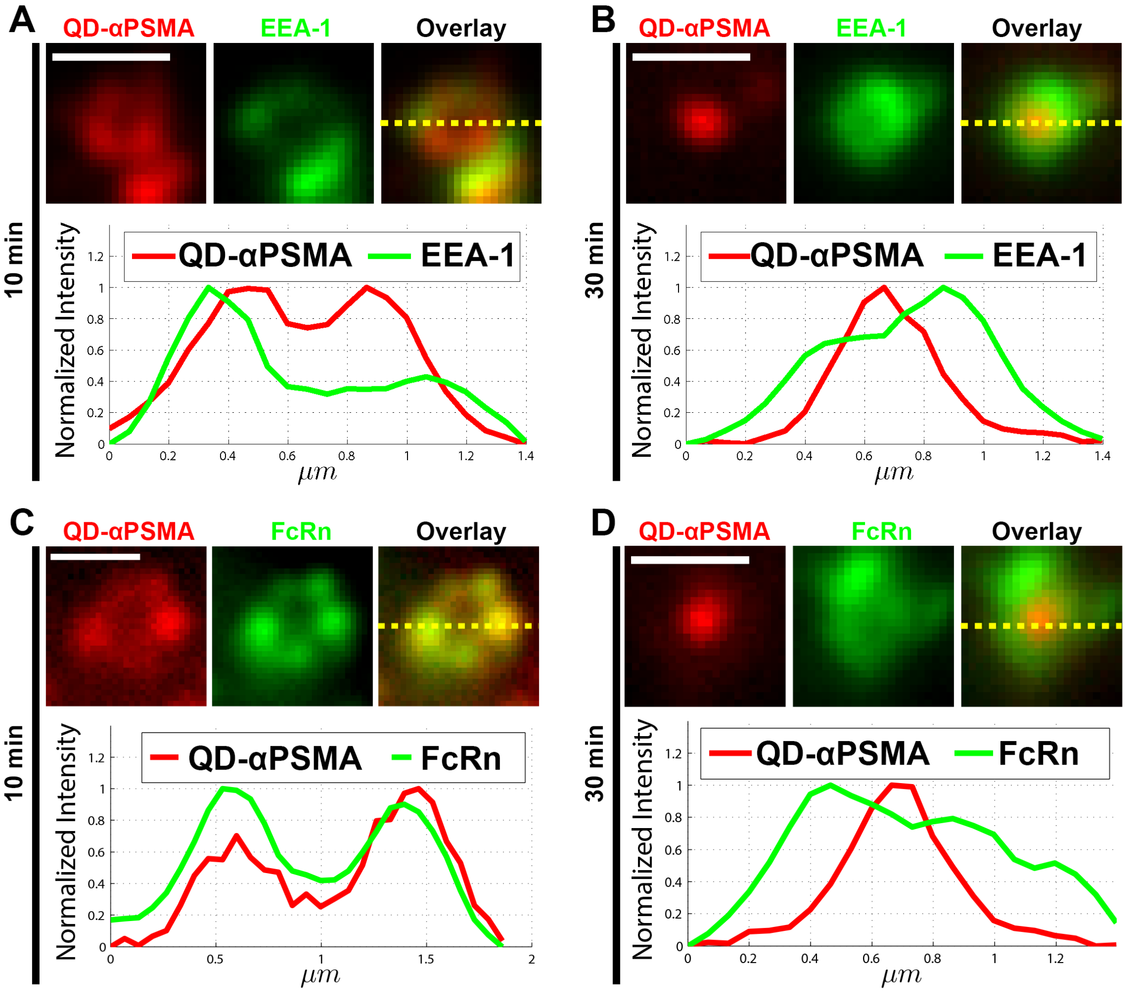

Figure 3.4: QD-αPSMA trafficking at the sorting endosomes in 22Rv1 cells. 22Rv1 cells were treated with QD-αPSMA for 30 minutes on ice followed by 10 minutes and 30 minutes incubation with imaging medium at 37°C. (A, C) QD-αPSMA is found at the limiting membrane of sorting endosomes at 10 minutes after the treatment. (B, D) QD-αPSMA is located at the center of sorting endosomes at 30 minutes after the treatment. 22Rv1 cells were either transfected with eGFP–FcRn and β2m (C,D) or stained with EEA-1 (A,B). Scale bars: 1 μm.

Next, we compare the distribution of QD-αPSMA in these sorting endosomes with that of EEA-1–positive endosomes. Untransfected 22Rv1 cells (Figure 3.4A and C) or 22Rv1 cells following cotransfection with eGFP–FcRn and human β2m expression constructs (Figure 3.4B and D) as described in Section 3.2.4 are used, with different chase times of 10 and 30 minutes. QD-αPSMA can be detected in early endosomes up to 30 minutes (see Section 3.3.5). Untransfected cells were stained with mouse monoclonal anti EEA-1 antibody and counter-stained with anti-mouse IgG (H+L) antibody–Alexa Fluor® 488 conjugate. Colocalization of QD-αPSMA on the limiting membrane of EEA-1–positive (Figure 3.4A) or FcRn–positive (Figure 3.4C) compartments was observed following 10 minutes of chasing (Figure 3.4A and C). By contrast, following 30 minutes of chasing, QD-αPSMA was observed in the center of the EEA-1–positive or FcRn–positive compartments (Figure 3.4B and D). Normalized fluorescence intensities along the yellow dotted lines in the overlay for each panel are presented in the fluorescence intensity plots.

3.3.4 FcRn–positive endosomes with LAMP-1–positive domains

As discussed in Section 3.3.3, sorting endosomes are identified by labeling them with FcRn [27, 55, 61, 62, 94, 96]. For later stages of endosomal trafficking involving multivesicular bodies and lysosomes, we use LAMP-1. LAMP-1 has previously been identified as a member of late endosomes and lysosomes [97]. Here, we identify some compartments which are labeled with both FcRn and LAMP-1 [98, 99].

Figure 3.5 shows 22Rv1 cells cotransfected with eGFP–FcRn, LAMP-1–mRFP and human β2m expression constructs and imaged as live cells (see Section 3.2.3 and 3.2.4 for details).

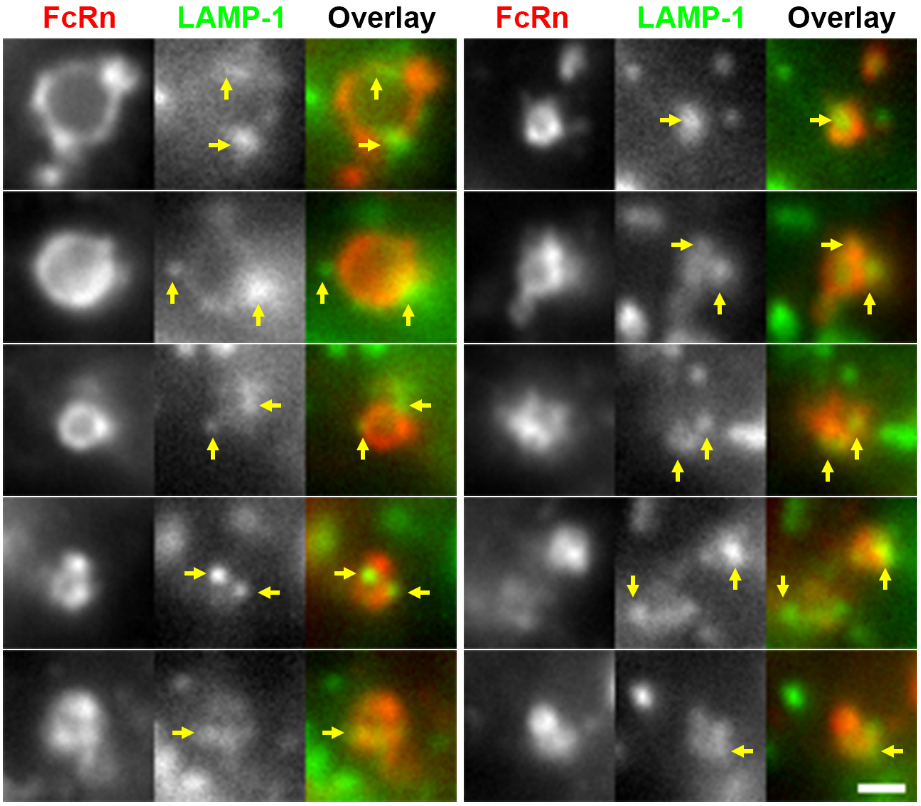

Figure 3.5: A subset of FcRn–positive endosomes with LAMP-1–positive domains. The distribution of FcRn + LAMP-1 on late endosomes indicates domain formation (yellow arrows). Scale bar: 1 µm.

3.3.5 PSMA-specific antibody trafficking

We started by establishing an experimental model using the human prostate carcinoma epithelial cell line, 22Rv1. QD-αPSMA was used for visualizing single molecule dynamics of PSMA-specific antibody. Figures 3.6 and 3.7 show preliminary measures of QD-αPSMA dynamics in 22Rv1 cells using immunofluorescence microscopy (see Section 3.2.10).

QD-αPSMA was internalized into early endosomes in 22Rv1 cells. 22Rv1 cells were prepared as described in Section 3.2.10 with different chase times of 0, 10, 20, 30 and 60 minutes. Cells were fixed, stained with CTxB–Alexa Fluor® 555 conjugate, and subsequently permeabilized and stained with mouse anti EEA-1 antibody. The bound EEA-1–specific antibody was detected using anti-mouse IgG (H+L) antibody–Alexa Fluor® 488 conjugate. QD-αPSMA was initially detected on the cell membrane (0 minute), followed by internalization into EEA-1–positive early endosomes within 10–20 minutes (yellow arrows). The localization in early endosomes was decreased following later chase times (30–60 minutes).

QD-αPSMA was trafficked into LAMP-1–positive late endosomes and lysosomes in 22Rv1 cells. 22Rv1 cells were prepared as described in Section 3.2.10 with different chase times of 0, 10, 20, 30 and 60 minutes. Cells were fixed, stained with CTxB–Alexa Fluor® 555 conjugate, and subsequently permeabilized and stained with mouse anti-human LAMP-1 antibody. The bound LAMP-1–specific antibody was detected using anti-mouse IgG (H+L) antibody–Alexa Fluor® 488 conjugate. QD-αPSMA was colocalized with LAMP-1–positive compartments following chase times of 30–60 minutes (yellow arrows).

In summary, QD-αPSMA reached sorting endosomes within 10 minutes (see Figure 3.6) followed by a decrease at later chase times (30–60 minutes). At the same

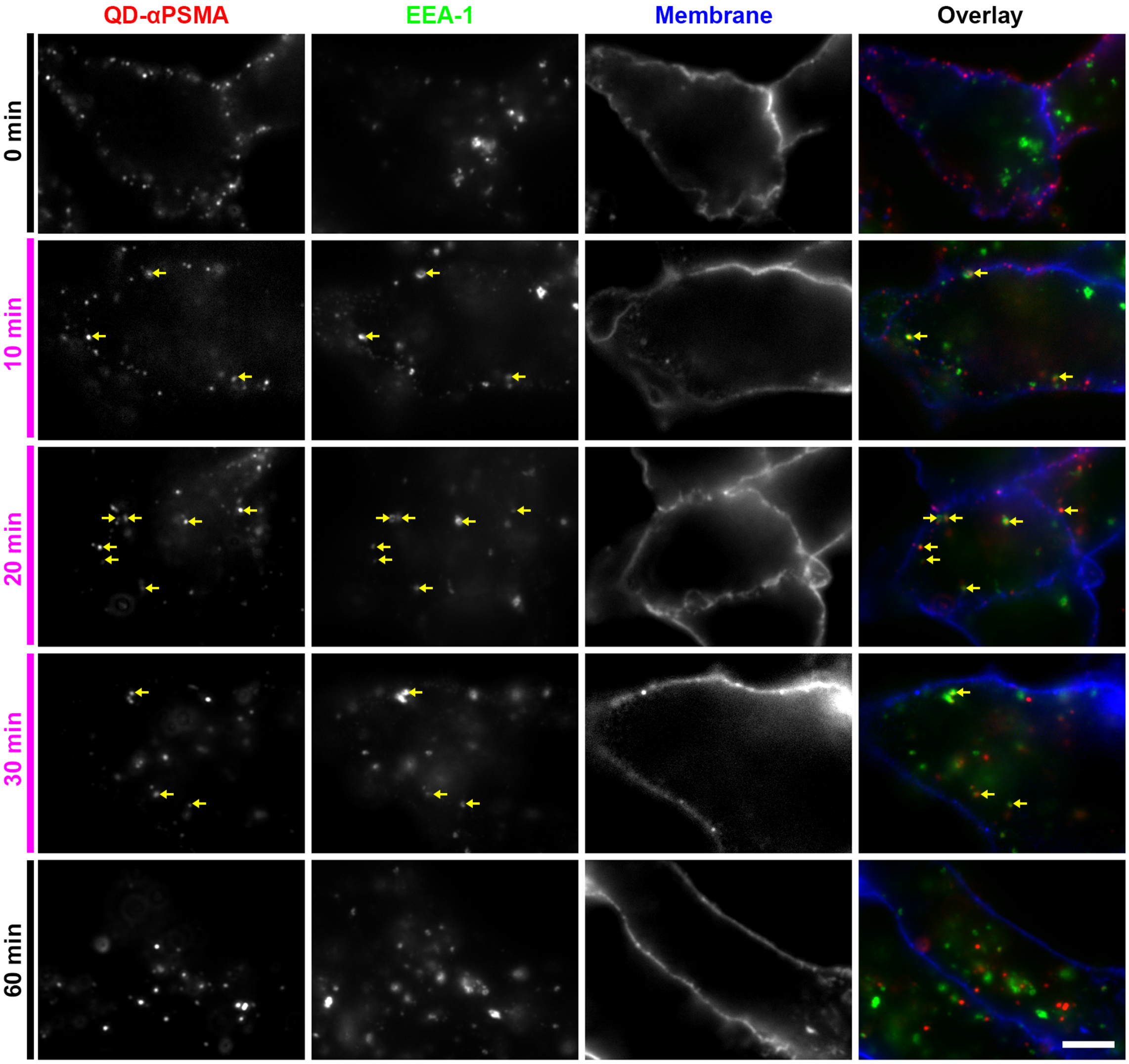

Figure 3.6: QD-αPSMA trafficking to sorting endosomes in 22Rv1 cells. QD-αPSMA is internalized into early endosomes. QD-αPSMA reaches sorting endosomes within 10 minutes. Colocalization between QD-αPSMA and EEA-1 cannot be detected after 60 minutes. Scale bar: 5 µm.

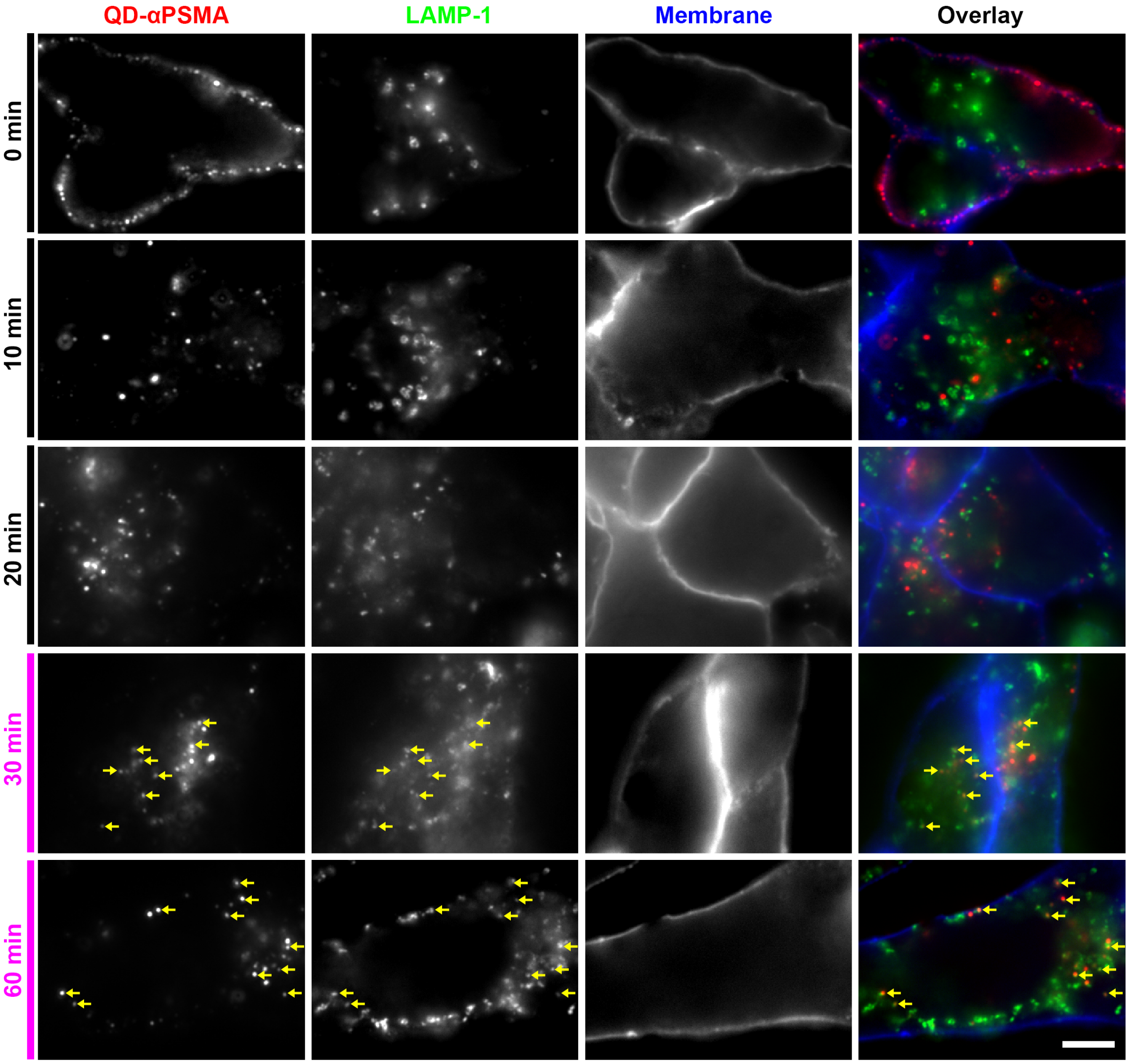

Figure 3.7: QD-αPSMA trafficking to late endosomes and lysosomes in 22Rv1 cells. QD-αPSMA is trafficked into LAMP-1–positive late endosomes and lysosomes. Colocalization between QD-αPSMA and LAMP-1 appears following 30–60 minutes. Scale bar: 5 µm.

time, QD-αPSMA appeared in lysosomes within 30 minutes (see Figure 3.7). Figures 3.6 and 3.7 shows one representative result, where three independent experiments were conducted for each. These results give a glimpse into QD-αPSMA dynamics in 22Rv1 cells.

3.3.6 QD-αPSMA trafficking imaged using rMUM

Here we uncover the detailed dynamics of QD-αPSMA in 22Rv1 cells using rMUM. Figure 3.8A and B show a QD-αPSMA trajectory (A) and cellular structures of a 22Rv1 cell (cell membrane and sorting endosomes, B) imaged using MUM- and simultaneously r-module. The QD-αPSMA trajectory shows complex dynamics including unconstrained motion, constrained motion and directed motion. Previously, we were unable to interpret this trajectory properly without knowing the context of these complex dynamics within the cellular environment. Using rMUM, we deliver both the single molecule dynamics and the cellular structure information simultaneously.

rMUM allows us to identify the trajectory at four different stages regarding the biological context. In Figure 3.8C, a QD-αPSMA molecule at the cell exterior rapidly moves toward the cell membrane, and the streaks of the QD-αPSMA was captured (0–0.58 seconds, inset 1). The QD-αPSMA attached to the cell membrane diffuses on the cell membrane (0.56–25.44 seconds, inset 2). Here we see two distinct diffusion behaviors: unconstrained diffusion (0.56–14.24 seconds) and constrained diffusion (14.24–25.44s). The QD-αPSMA undergoes endocytosis, and its endocytic trafficking shows highly directional diffusion toward the cell interior (25.44–36.72 seconds, inset 3). The QD-αPSMA finally reaches the sorting endosome and spherically diffuses on the inner leaflet of the sorting endosome (36.72–68.64 seconds, inset 4).

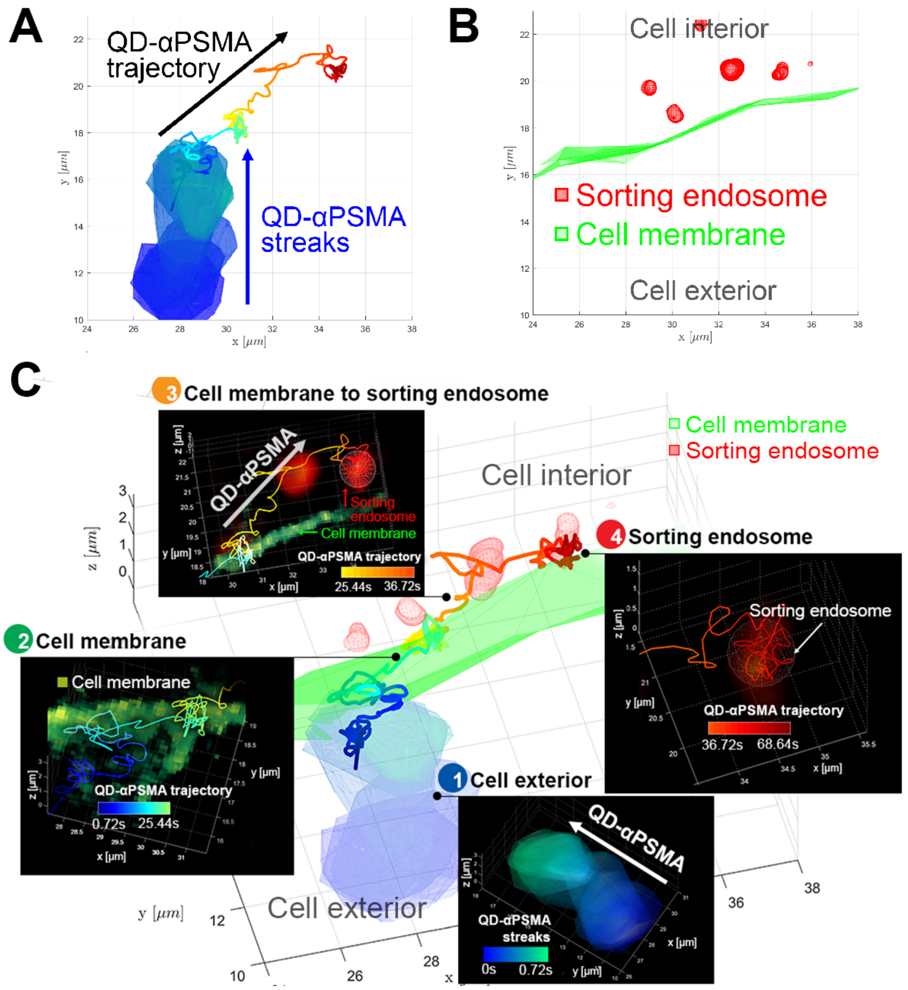

Figure 3.8: Trafficking pathway of a PSMA-specific antibody molecule in a 22Rv1 cell imaged using rMUM. QD-αPSMA trajectory is imaged using the MUM-module, (A) and cellular structures, i.e. sorting endosomes (red) and cell membrane (green) imaged from the r-module (B), are spatially-temporally registered and visualized (C). (C) Insets visualize QD-αPSMA trafficking in the context of the cellular structures of (1) cell exterior, (2) cell membrane, (3) cell membrane to sorting endosome and (4) sorting endosome.

In the following sections, we investigate precise details of these PSMA-specific antibody dynamics in the prostate cancer cells using rMUM.

3.3.7 QD-αPSMA in cell exterior

Imaging single molecule dynamics in the growth medium is very difficult due to the high diffusion rate. For instance, diffusion coefficient measures of IgG molecules in water are in the range of 40 $\mu m^2/s$ [100]. Therefore traditional imaging of this process is not likely to be successful with the photon emission rate that can be realistically achieved with standard fluorescent probes in the live cell imaging environment. We have therefore chosen to image the diffusing single molecule with exposure times so that "streaks" in the single molecule are expected to be recorded on the camera. Due to the speed of the molecule and the low photon emission rate the signal level of this streak is very low. Therefore, it would not be detectable in one image above the background signal. To solve this, synchronized acquisition in MUM allows us to observe the molecular "streak" on different focal planes along parts of the trajectory, thereby confirming a single molecule trajectory (see Figure 3.9). Streak of single molecule appears as smeared fluorescence signal over different focal plane images (see Figure 3.10). Twenty events were identified from three independent experiments and one representative result is shown in Figures 3.9 and 3.10.

Figure 3.9 shows the approach of a QD-αPSMA towards 22Rv1 cells. 22Rv1 cells were transfected with mRFP–FcRn and AcGFP–MEM. The QD-αPSMA channel was imaged using the MUM-module and FcRn and MEM channels were imaged using the r-module. The behavior of the QD-αPSMA in the imaging medium is highly dynamic. Therefore, it is almost impossible to image the dynamics using conventional time-lapse imaging techniques (see also Figure 3.10). The maximum intensity

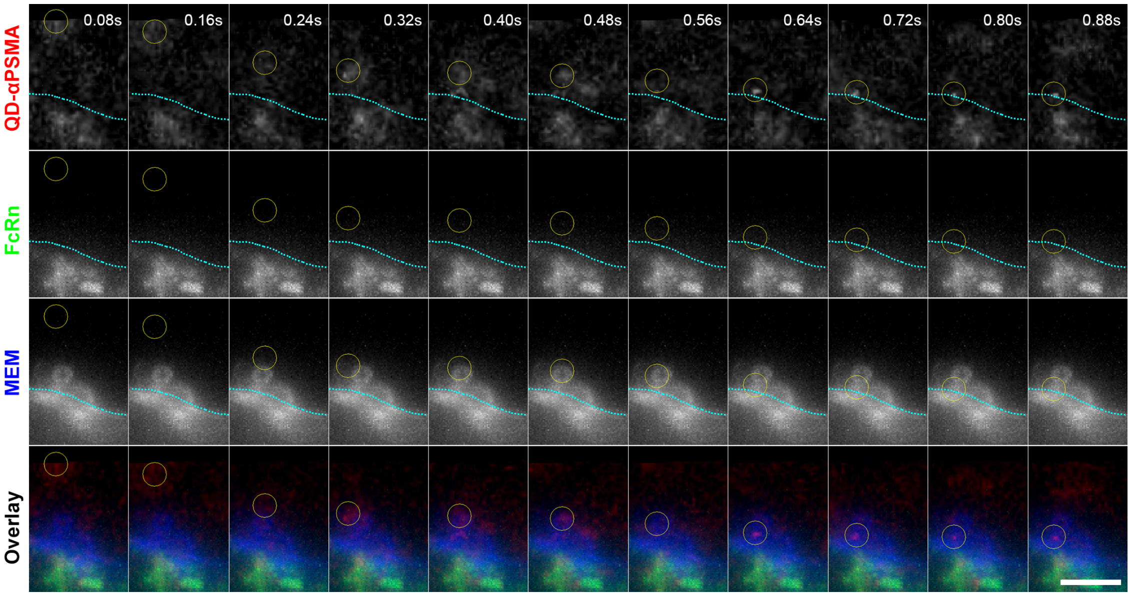

Figure 3.9: Approach of a QD-αPSMA towards the 22Rv1 cell membrane. Scale bar = 5 µm.

projections of four focal plane images of the QD-αPSMA is presented for each frame. Similarly, the maximum intensity projections of the time-lapse z-stacks of FcRn and MEM are presented. The QD-αPSMA appears at the top of the image (circle) and rapidly reaches the cell membrane within a period of 0.48 seconds. Subsequently, the QD-αPSMA diffuses on the cell membrane surface.

Figure 3.10 shows the detailed dynamics of the QD-αPSMA at the cell exterior imaged using the MUM-module. The rapid dynamics of a QD-αPSMA at the cell exterior, i.e., in imaging medium, were imaged using the MUM-module (see also Figure 3.9). The MUM-module was used to acquire a series of large–volume images at high frame rate. Therefore, the trace of the single QD was captured as it traveled over 5 µm within 560 µs. In Figure 3.10A, the single QD trace was imaged using MUM. Each row represents focal planes, i.e. top plane, mid-top plane, mid-bottom plane and bottom plane from top to bottom. Each column represents frames from

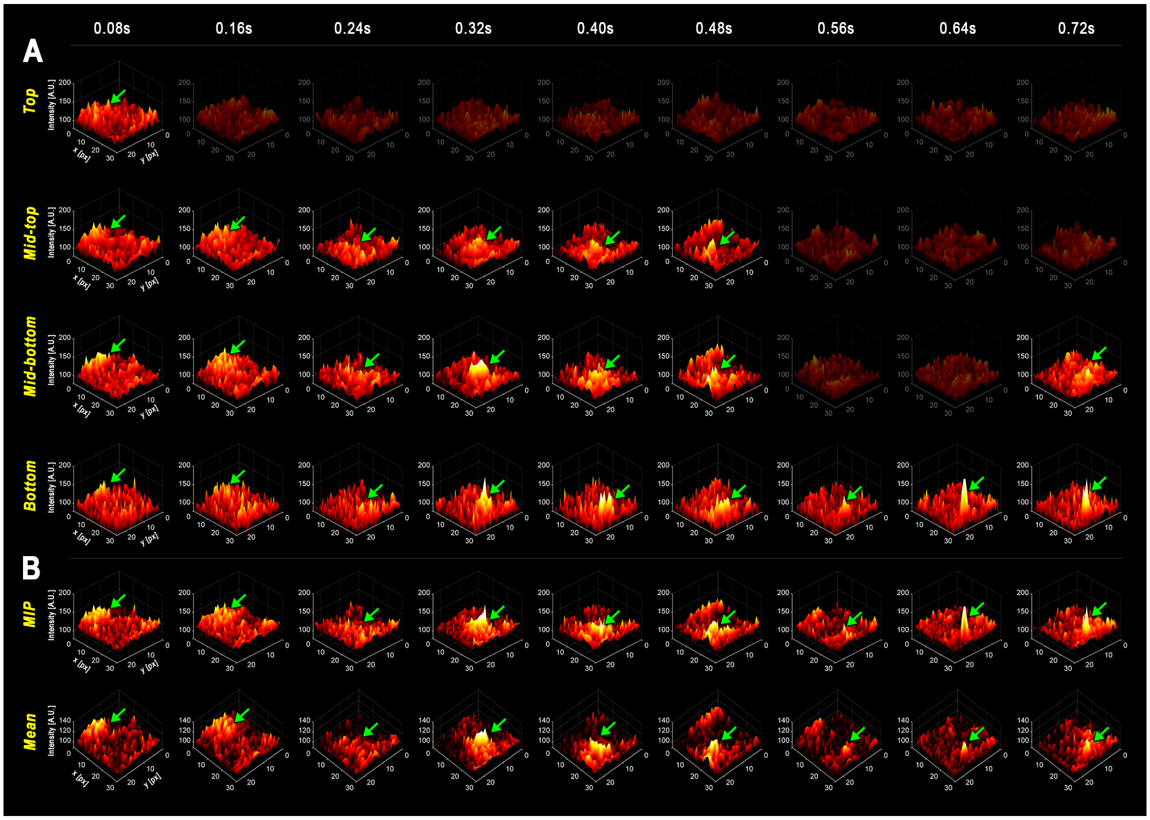

Figure 3.10: Dynamics of QD-αPSMA at the cell exterior imaged using the MUM-module. (A) QD-αPSMA streaks are shown in different focal plane images. (B) Maximum intensity projection images (MIP) and average projection (mean) images of (A) are plotted. Green arrows indicate the streak signal.

time-lapse images, with the time of acquisition shown. The streaks of the single QD observed across multiple focal planes during the 0–480 µs time frame is shown. Subsequently, the QD localizes to the cell membrane at 560 µs. Figure 3.10B shows maximum intensity projection (MIP) and mean projection of MUM data of Figure 3.10A.

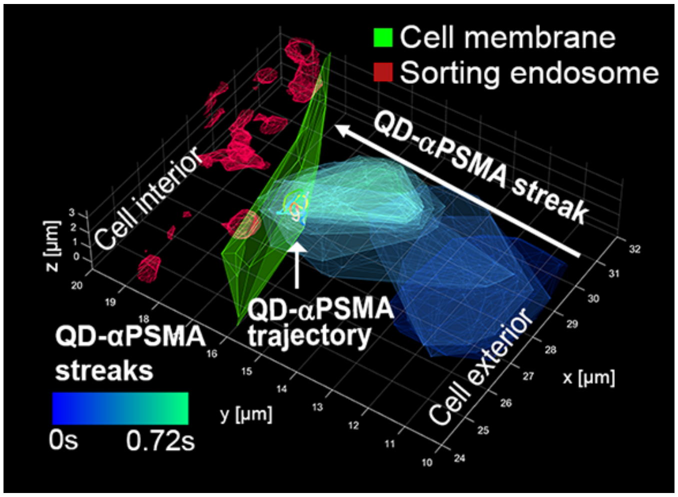

Figure 3.11: 3D reconstruction of QD-αPSMA streaks in cell exterior imaged using rMUM. A QD-αPSMA outside the cell moves toward the 22Rv1 cell membrane.

In Figure 3.11, the streaks identified in Figures 3.9 and 3.10 and the cell membrane and sorting endosomes are visualized as described in Section 2.4.7. This shows the streaks of the QD-αPSMA as it approaches the cell membrane.

3.3.8 Unconstrained and constrained diffusion of QD-αPSMA at the cell membrane

The classical approach to studying ligand-receptor dynamics on the cell membrane is by total internal reflection fluorescence microscopy (TIRFM) [61, 101, 102].

This, however, has several potential problems, as TIRFM imaging occurs at the cell membrane adjacent to the coverslip. First, it can be difficult to deliver a ligand such as the PSMA-specific antibody to the cell membrane adjacent to the coverslip as is necessary when using TIRFM imaging. Second, the adhesion of this cell membrane imaged by TIRFM to the coverslip might impact the trafficking behavior.

Through our imaging system, we can now study trafficking on any part of the cell membrane as we can visualize the cell membrane through the r-module and the single molecule dynamics through the MUM-module. Here we studied the diffusion of the QD-αPSMA on different parts of the cell membrane of 22Rv1 cells. QD-αPSMA trajectories were imaged from three different parts of the cell of 22Rv1 cells: the membrane that is adjacent to the cover glass (ventral); the membrane that is on the opposite side of the cell from the cover glass (dorsal) and the lateral side of the cell (lateral, see Figure 3.12A). Similarly, Figures 3.12B and C show the unconstrained diffusion of QD-αPSMA at the other parts of the membrane that we consider. Figure 3.12D shows unconstrained diffusion of a QD-αPSMA at the lateral surface imaged using rMUM. The difficulty here is not only the imaging of the single molecule motion along the optical axis but also that the membrane itself is not stationary. Here we can see both the cell membrane and the QD-αPSMA moves together while the QD-αPSMA diffuses on the lateral surface of the cell membrane.

To understand the dynamics of QD-αPSMA at the different locations, the trajectories were analyzed using mean square displacement (MSD) analysis to determine the diffusion coefficients described in Section 2.4.1. We collected 56 additional QD-αPSMA trajectories at three parts of the cellular membrane, and the average diffusion rate was 0.27 ± 0.06 $\mu m^2/s$ (see Figure 3.12E). These results demonstrate that the estimated diffusion coefficients are essentially identical for the three parts of the cellular membrane. The QD-αPSMA diffusion rates at the dorsal membrane, however, show twice the variability compared to those at the other membrane sites.

In addition, we identified QD-αPSMA trajectories showing constrained diffusion at the three parts of the cellular membrane. The average diffusion rate was measured as 0.011 ± 0.008 $\mu m^2/s$ (see Figure 3.12E, n = 52). The diffusion rates were statistically very similar among the three membrane locations for both the unconstrained and constrained populations (Welch's t–test, $p > 0.1$).

3.3.9 Directional motions of QD-αPSMA in endocytic and exocytic pathways

Following the unconstrained and the constrained diffusive motions on the cell membrane, QD-αPSMA undergoes endocytosis and moves towards a sorting endosome with highly directed motion in the prostate cancer cells. Figure 3.13A illustrates the endocytic pathway of an antibody molecule in the cell. The antibody on the cell membrane enters the cell by crossing the cell membrane, moves toward a sorting endosome and then merges with the sorting endosome. To identify and analyze such complex dynamics of the endocytic pathway at the single molecule level, both single molecule, and cellular context information are necessary. Also, single molecule dynamics and cellular structures are highly three-dimensional. Therefore, it is necessary to obtain both 3D single molecule trajectory and 3D cellular structure data. rMUM fulfills such requirements and is capable of identifying the endocytic pathway of QD-αPSMA in 22Rv1 cells.

A QD-αPSMA endocytosis event in a 22Rv1 cell was captured using rMUM (see Figure 3.13B). The sample was prepared and imaged as described in Section 3.2.6. Three-dimensional reconstructions of the cellular structures of the FcRn compartments and the membrane are shown in red and green, respectively. The QD-αPSMA trajectory is pseudocolored over time (0–51.20 seconds). Here a QD-αPSMA dif-

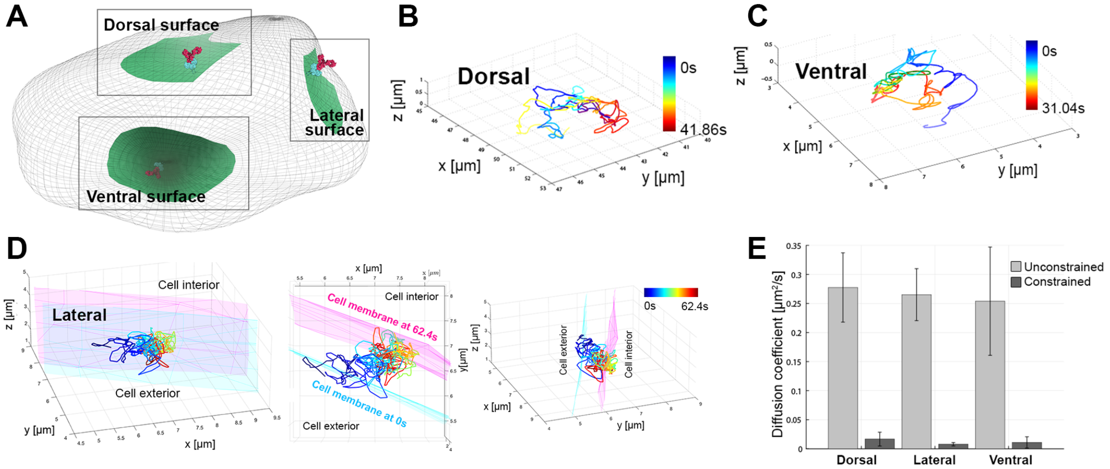

Figure 3.12: The diffusive motion of QD-αPSMA on different parts of the cellular membrane. (A) QD-αPSMA was studied at three different sites: dorsal surface, lateral surface and ventral surface adjacent to the coverslip. (B) A trajectory of a QD-αPSMA at the dorsal cell membrane. (C) A trajectory of a QD-αPSMA at the ventral cell membrane. (D) A QD-αPSMA trajectory at the lateral cell membrane. The cell membrane structure at the beginning (0 seconds) and at the end (62.4 seconds) of a trajectory was reconstructed and is shown in 3D, pseudocolored in blue and pink, respectively. The same reconstruction is shown in different viewpoints: 3D (top panel), top view (middle panel) and side view (bottom panel). (E) The diffusion coefficients of 108 QD-αPSMA trajectories on the cell surface were identified and analyzed. Two different populations were detected at all three sites: unconstrained diffusion trajectories and constrained diffusion trajectories. The diffusion rates for the unconstrained diffusion tracks were measured as 0.27 ± 0.05 $\mu m^2/s$, 0.26 ± 0.04 $\mu m^2/s$ and 0.25 ± 0.09 $\mu m^2/s$ from the dorsal, lateral and ventral cellular membrane respectively. The diffusion coefficients for the constrained diffusion tracks were measured as 0.016 ± 0.011 $\mu m^2/s$, 0.007 ± 0.002 $\mu m^2/s$ and 0.011 ± 0.009 $\mu m^2/s$ from the dorsal, lateral and ventral membrane respectively. There are no significant differences in the diffusion rates among the same population (Welch's t–test, $p > 0.1$). Data were obtained from nine independent experiments.

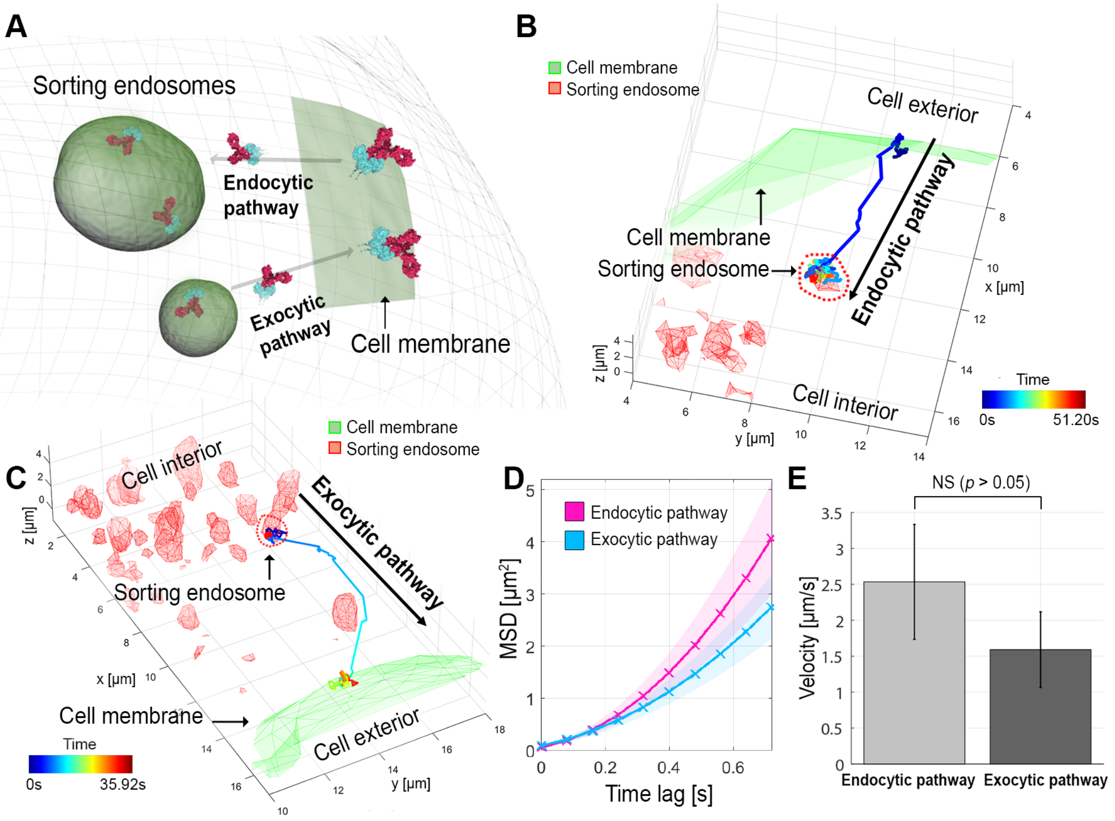

Figure 3.13: QD-αPSMA in endocytic and exocytic pathway. QD-αPSMA in endocytic and exocytic pathway in 22Rv1 cells are identified using rMUM. (A) Antibody-antigen complex on the cell membrane may undergo endocytosis and reach the sorting endosome along the endocytic pathway. Such an antibody-antigen complex may be recycled via the exocytic pathway and return to the cell membrane or the cell exterior. (B) A QD-αPSMA on the endocytic pathway is captured using rMUM. (C) A recycling event of a QD-αPSMA is imaged using rMUM. (D) The directed motion of QD-αPSMA in (B) and (C) is analyzed using the MSD analysis method with directed diffusion model. (E) 69 QD-αPSMA trajectories on endocytic or exocytic pathways are analyzed using the MSD analysis in (D), and the average velocity measures are plotted with error bars indicating standard deviation. (Welch's t–test, $p = 0.1008$). Data were obtained from seven independent experiments.

fuses into the cell membrane, followed by rapid endocytosis which is visualized as a highly directed movement of the QD-αPSMA towards the sorting endosome. The QD-αPSMA then enters the sorting endosome and diffuses within it. The MSD analysis is performed to characterize such a directed motion (see Figure 3.13D, and see Section 2.4.1 for the analysis). The QD-αPSMA molecule in Figure 3.13B moves from the cell membrane to a sorting endosome at a speed of 2.59 µm/s, and it takes 2 seconds to reach the sorting endosome from the cell membrane. We identify 55 endocytosis events, and the average speed of endocytosis was measured as 2.54 ± 0.80 $\mu m^2/s$ while the average distance and duration of endocytosis were measured as 10.25 ± 9.31 μm and 5.12 ± 4.91 seconds, respectively.

We also observed exocytosis (recycling) of QD-αPSMA from the sorting endosome to the cell membrane. Figure 3.13A describes the exocytic pathway of the antibody molecule. The antibody within the sorting endosome is transported to the cell membrane, followed by the exocytosis event. The antibody stays either at the cell membrane or is released into the cell exterior [103].

Figure 3.13C visualizes an exocytosis event of QD-αPSMA in a 22Rv1 cell imaged using rMUM. The exocytosis trajectories were characterized using the same MSD analysis as for endocytosis (see Figure 3.13D, and see Section 2.4.1 for the analysis). The speed along the exocytic pathway was measured as 1.46 µm/s. We found 14 exocytosis events of QD-αPSMA in 22Rv1 cells. The average speed of exocytosis was measured as 1.59 ± 0.53 µm/s (see Figure 3.13E). However, the distance and the duration of the exocytosis events are not consistent (7.06 ± 2.71 µm and 2.97 ± 2.22 seconds). Apparently, the difference between the endo- and the exocytosis speed of the QD-αPSMA is not statistically significant. Following exocytosis, the QD-αPSMA molecules did not leave the cell but remained on the cell membrane with unconstrained diffusion. The diffusion rate was measured as 0.25 ± 0.03 $\mu m^2/s$, a value that is similar to that of the unconstrained diffusion on the cell membrane from Section 3.3.8.

3.3.10 Clathrin-mediated endocytosis of QD-αPSMA

Clathrin is a protein that forms coated vesicles [104, 105, 106]. The vesicle formation involves receptor internalization, which is categorized as active transport of endocytic activity. This process is called clathrin-mediated endocytosis [107, 108, 109]. Clathrin-mediated endocytosis is an essential cargo internalization mechanism in mammalian cells. There are two pathways of clathrin-mediated endocytosis: (1) membrane receptors recruit clathrin molecules to form a vesicle [105, 109], or (2) membrane receptors move to existing clathrin pits and undergo endocytosis [110]. Roles of these two different pathways is not known yet and speculations about the effect of size and affinity of the receptors is documented [111].

Various studies show that PSMA–PSMA-specific antibody complexes in prostate cancer cells internalize rapidly [88, 112, 113]. However, the mechanism by which they internalize is controversial [89, 90, 112, 114, 115]. From previous studies in Section 3.3.5, QD-αPSMA reaches the sorting endosome within 10 minutes of traversing the cell membrane (see Figure 3.6). Here we investigate the early stages of endocytosis of QD-αPSMA with clathrin.

3.3.10.1 QD-αPSMA and clathrin pits on the cell membrane

We first identify QD-αPSMA colocalized with clathrin pits on the cell surface prior to internalization in 22Rv1 cells (see Figure 3.14). 22Rv1 cells were transfected with mRFP–FcRn, eGFP–CLC and human β2m expression constructs (see Section 3.2.4). Cells were prepared as described in Section 3.2.10 with different chase times of 0, 3, 6 and 10 minutes. QD-αPSMA is colocalized with clathrin pits on the cell

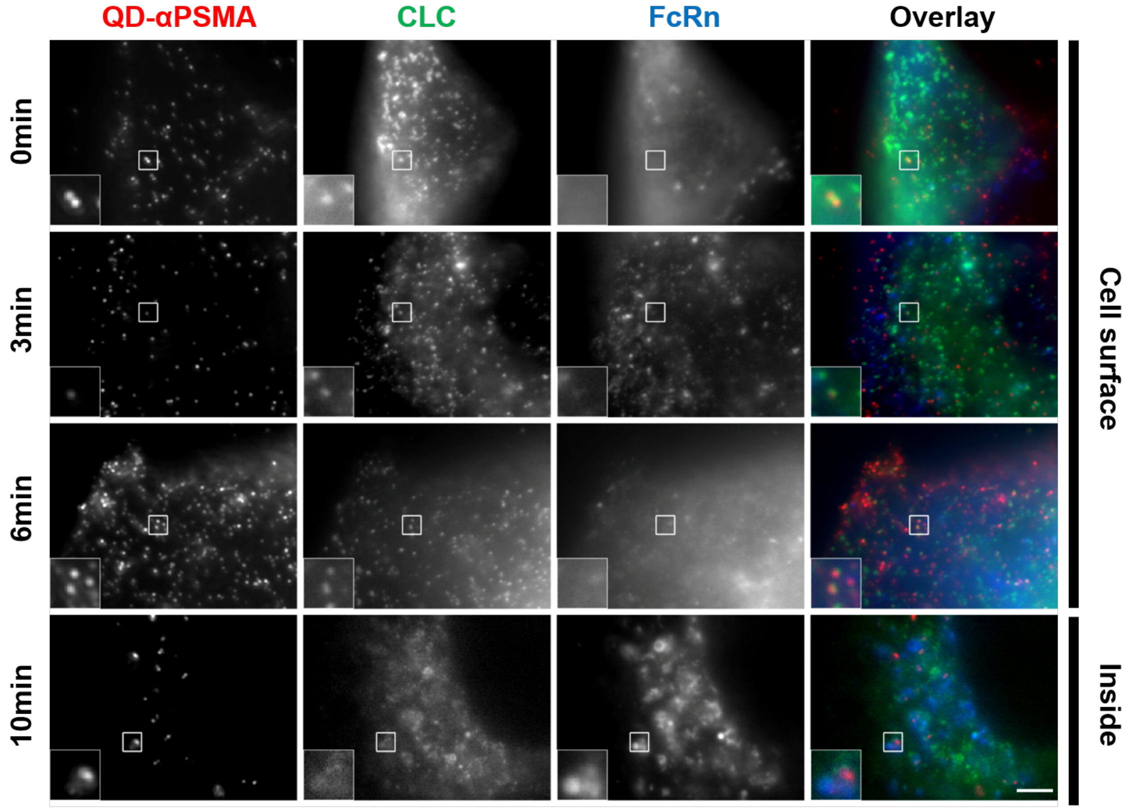

Figure 3.14: Colocalization between QD-αPSMA and clathrin pits. QD-αPSMA colocalizes with clathrin pits found on the 22Rv1 cell memebrane prior to internalization within 0–6 minutes. QD-αPSMA reaches FcRn–positive compartments in 10 minutes. Scale bar: 6 µm.

surface between 0–6 minutes. QD-αPSMA is present in compartments that were both FcRn- and clathrin–positive following 10 minutes of QD-αPSMA incubation. Figure 3.14 shows one representative result from two independent experiments.

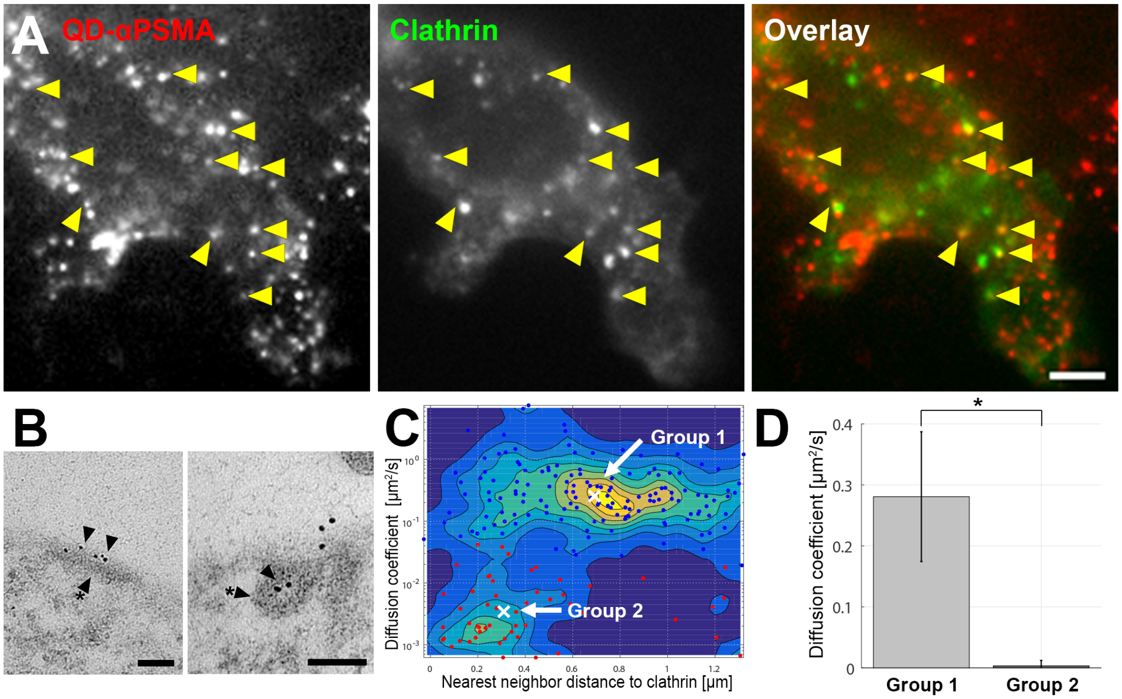

Figure 3.15: QD-αPSMA and clathrin pit on the 22Rv1 cell membrane. (A) 22Rv1 cells were transfected with eGFP-CLC and incubated with QD-αPSMA and imaged as live cells. Yellow arrows indicate the colocalization of QD-αPSMA and clathrin pits on the cell membrane. (B) Transmission electron micrograph of QD-αPSMA in 22Rv1 cells reveals QD-αPSMA in the coated pits. (C) Correlation between QD-αPSMA and clathrin pits on the cell membrane is evaluated. Diffusion rates of QD-αPSMA is very low when the QD-αPSMA is correlated with the clathrin pits. (D) Average diffusion rates with standard deviations of the two populations identified from (C) are plotted. Scale bar: (A) 5 µm (B) 100 nm.

Figure 3.15 shows QD-αPSMA and clathrin pits on the cell membrane. 22Rv1 cells were prepared as described in Section 3.2.6 and subsequently imaged using the dual-color live cell microscopy setup which is a modified dual-color rMUM setup (see Figure 2.7 and Section 2.2.3). Two electron multiplying charge-coupled device (EMCCD) cameras (C2 and C4 in Figure 2.7) acquire QD and GFP channels simultaneously. Figure 3.15A shows colocalization between QD-αPSMA and clathrin pits on the cell membrane. Yellow arrows indicate the colocalization.

Diffusive motion of QD-αPSMA is measured from live cell imaging data. We extract QD-αPSMA tracks using the automated tracking method (see Section 2.4.5). Diffusion coefficients are obtained from the tracks using the MSD analysis (see Section 2.4.1.1). Average distance between QD-αPSMA trajectories and clathrin pits was evaluated using nearest-neighbor search (see Section 2.4.6). Diffusion rate measures of 205 QD-αPSMA trajectories were plotted against average distance to the clathrin pits in Figure 3.15C. From the plot, two groups of QD-αPSMA tracks were identified using gap statistics [84] and analyzed using K-means cluster analysis [83]. The blue population (group 1) in Figure 3.15C appears to have large diffusion rate (cluster centroid = 0.25 $\mu m^2/s$) when QD-αPSMA and clathrin coated pits are presented separately (average distance = 0.69 µm). The red population (group 2) in Figure 3.15C has a lowdiffusion rate (cluster centroid = 0.0034 $\mu m^2/s$) when QD-αPSMA and clathrin coated pits are close to each other (average distance = 0.03 µm). The average diffusion rates are calculated as 0.28 ± 0.11 $\mu m^2/s$ and 0.0034 ± 0.0088 $\mu m^2/s$ for group 1 and group 2 respectively and are significantly different (see Figure 3.15D). Data were obtained from six independent experiments.

Figure 3.15B shows transmitted electron micrographs of QD-αPSMA on 22Rv1 cells. In the left panel, QD-αPSMA (arrows) is trapped in the coated pit (arrow with a star). The right panel shows QD-αPSMA (arrows) inside of the coated vesicle (arrow with the star). These results indicate that QD-αPSMA enters clathrin coated pit, and their diffusion rate dramatically decreases as a result.

3.3.10.2 Clathrin-mediated QD-αPSMA endocytosis

QD-αPSMA and clathrin pits are colocalized on the cell membrane with QD-αPSMA on clathrin pits being immobile (see Section 3.3.10.1). Here we capture the moment at which the clathrin–QD-αPSMA complex undergoes endocytosis (Figure 3.16). 22Rv1 cells were prepared as described in Section 3.2.6. The sample was then imaged using a dual-color MUM setup, which is a dual-color rMUM setup as in Figure 2.7, with no r-module operation.

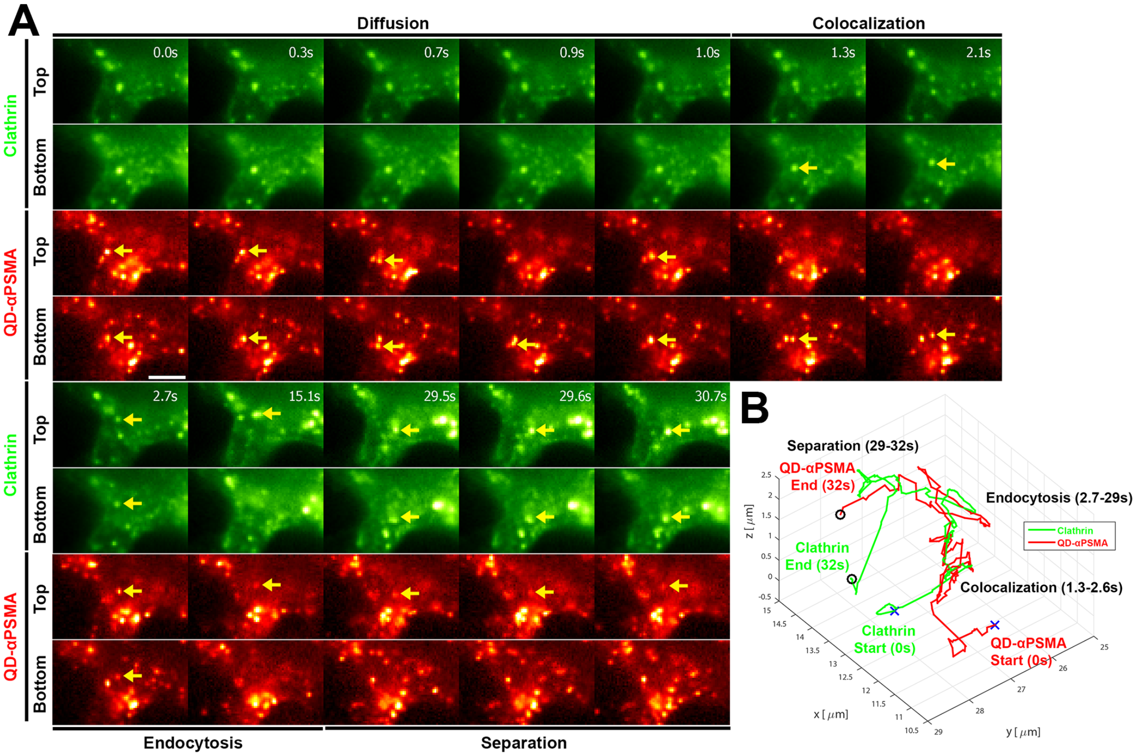

Figure 3.16: Clathrin-mediated endocytosis of QD-αPSMA. A QD-αPSMA undergoing clathrin-mediated endocytosis is captured using a dual-color MUM configuration. (A) Two focal planes (bottom and top) with dual channel images of clathrin (green) and QD-αPSMA (red) are shown over time. "Bottom" images are focused on the cell membrane above the coverslip. Yellow arrows indicate QD-αPSMA and clathrin pit/vesicle of interest. (B) The QD-αPSMA and clathrin trajectories estimated using MUMLA are plotted. Scale bar: (A) 3 µm.

Figure 3.16A visualizes endocytosis of a clathrin–QD-αPSMA complex imaged using MUM. Two focal plane images of clathrin and QD-αPSMA are shown as green and red channels, respectively. Yellow arrows indicate a QD-αPSMA or a clathrin pit of interest. A QD-αPSMA on the cell membrane diffuses on the cell membrane (0–1 second). The QD-αPSMA then moves towards a clathrin pit and colocalizes for 1.3 seconds (1.3–2.6 seconds). Subsequently, the clathrin–QD-αPSMA complex undergoes endocytosis. Here the complex from the cell membrane (bottom) moves towards the cell interior (top, 2.7–29 seconds). Finally, the QD-αPSMA and clathrin become separated (29–32 seconds). Trajectories of QD-αPSMA and clathrin are obtained using the MUMLA algorithm (see Section 2.3.1). Figure 3.16B shows the plot of the QD-αPSMA track and clathrin track in red and green respectively.

3.3.11 QD-αPSMA at the sorting endosome

QD-αPSMA on the cell membrane undergoes clathrin-mediated endocytosis (see Section 3.3.10). Figure 3.17B shows endocytosis of a clathrin–QD-αPSMA complex in 22Rv1 cells imaged using rMUM (see Sections 3.2.6 and 2.2.3 for the sample preparation and the rMUM setup, respectively). The clathrin–QD-αPSMA complex at the cell membrane undergoes endocytosis followed by directed motion towards a sorting endosome. Note that the clathrin signal decreases over time.

Subsequent to the directed motion towards a sorting endosome (see Section 3.3.9), the vesicle carrying QD-αPSMA appears to fuse with the sorting endosome (see Figure 3.17A). This is followed by what appears to be a diffusive motion on the membrane of the sorting endosome.

With rMUM, we were able to capture the directional motion of the QD-αPSMA in the endocytic pathway followed by the fusing event (Figure 3.17C). Here the QD-

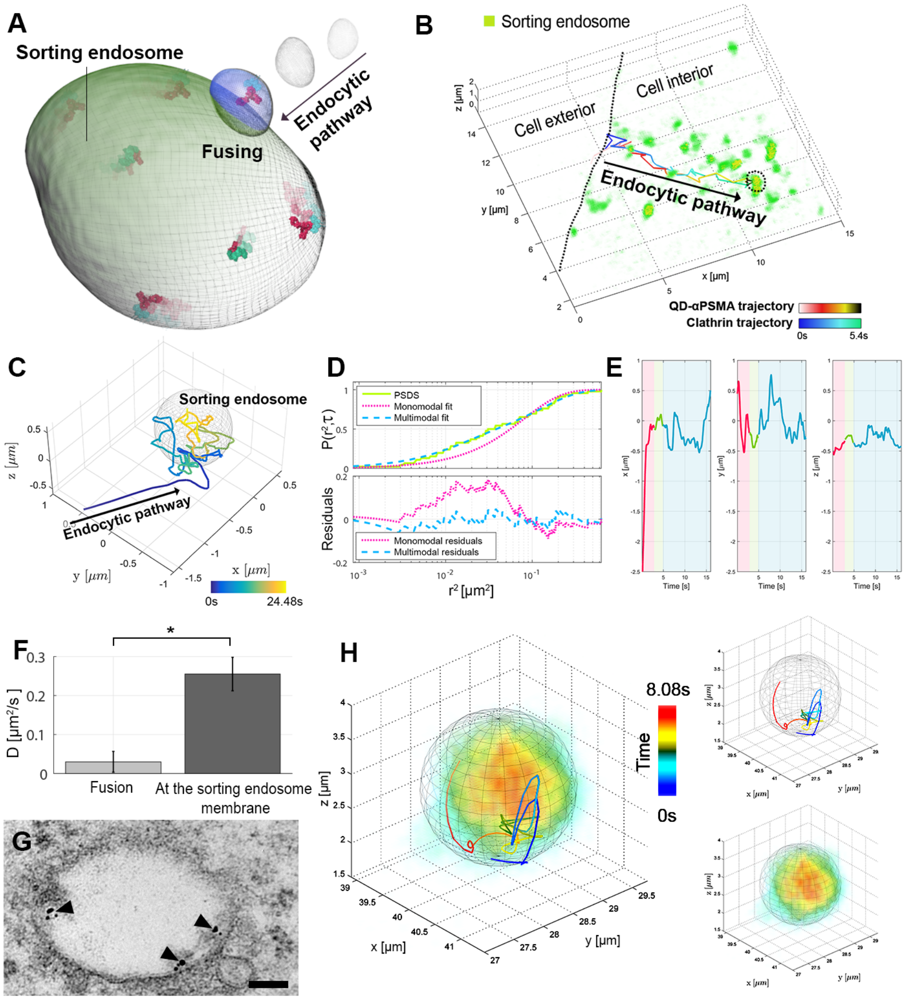

Figure 3.17: Trafficking of QD-αPSMA on a sorting endosome. (A) Illustration of endocytic trafficking. (B) Clathrin mediated endocytosis of QD-αPSMA was imaged using the rMUM. Both the clathrin vesicle and the QD-αPSMA move towards the sorting endosome. (C-D) The QD-αPSMA trajectory while approaching and reaching the sorting endosome (C) was analyzed using the PDSD analysis (D). (E) A short constrained motion is identified followed by the unconstrained diffusion on the sorting endosome. (F) These two different diffusive motions from 18 QD-αPSMA trajectories were analyzed, and the average diffusion and standard deviation are plotted. There were significant differences between two diffusive motions (indicated by *; Welchs t–test, $p < 0.01$) (G) A transmission electron micrograph shows that QD-αPSMA is on the inner leaflet of the sorting endosome in 22Rv1 cells. Black arrows indicate QD-αPSMA. (H) Spherical diffusive motion of QD-αPSMA on the sorting endosome is imaged using rMUM. Scale bar: (G) 100 nm.

αPSMA fuses with the sorting endosome and then diffuses on the inner leaflet of the sorting endosome. To identify the time of the fusing event, the trajectories after endocytosis were analyzed using the probability distribution of square displacement (PDSD) analysis (see Section 2.4.3 and Figure 3.17D). The time between encountering the sorting endosome and the beginning of diffusive motion was rather short, with an average of 1.30 ± 0.78 seconds. After the QD-αPSMA fused with the sorting endosome, the QD-αPSMA was released to the inner leaflet of the sorting endosome. The diffusion rate at the time point of the QD-αPSMA fusion was determined to be 0.029 ± 0.05 µm^2/s (n = 18, Figure 3.17G, fusion). X, Y and Z coordinates of the trajectory (Figure 3.17E) are plotted over time (Figure 3.17D). Here we identified three distinct diffusive motions: directed diffusion, constrained diffusion and unconstrained diffusion. QD-αPSMA moves towards the sorting endosome along the endocytic pathway in a highly directed motion (pink). Constrained diffusion of the QD-αPSMA was observed during a short period (green) in which the QD-αPSMA is transported into the sorting endosome. Subsequently, the QD-αPSMA diffuses on the inner leaflet of the sorting endosome (blue). A transmission electron micrograph of the QD-αPSMA (black dots with arrows) in the sorting endosome confirms that QD-αPSMA exists on the inner limiting membrane of the sorting endosome (Figure 3.17G).

We wanted to measure the diffusion coefficient of the QD-αPSMA on the sorting endosomal membrane. The rMUM instrument permits the imaging of the trajectories of antibodies within the sorting endosomes. (see Section 2.4.4). However, trajectory is not continued to a planar space, and coupled with significant movement of the sorting endosome during acquisition, this complicates the process of data analysis. With suitable compensation for both effects, the diffusion coefficient could be determined (see Section 2.4.1.4). The diffusion rate was measured as 0.25 ± 0.04

µm^2/s (n = 22, see Figure 3.17F, at the sorting endosome membrane). Data were obtained from six independent experiments. For accurate diffusion rate measures, the MSD analysis with sphere diffusion model was used. This is consistent with that measured on the cell membrane, suggesting that diffusion on the sorting endosome membrane is analogous to the diffusion on the cell membrane. We confirm that there is no significant difference in the diffusion rates between the QD-αPSMA dynamics on the sorting endosome membrane and the unconstrained diffusive motion of QD-αPSMA on the cell membrane in Figure 3.12 (Welch's t–test, $p > 0.01$). There is a dramatic difference between the diffusion rate during the fusion of QD-αPSMA with the sorting endosome and the unconstrained diffusion on the sorting endosome (see Figure 3.17F, Welch's t–test, $p < 0.01$).

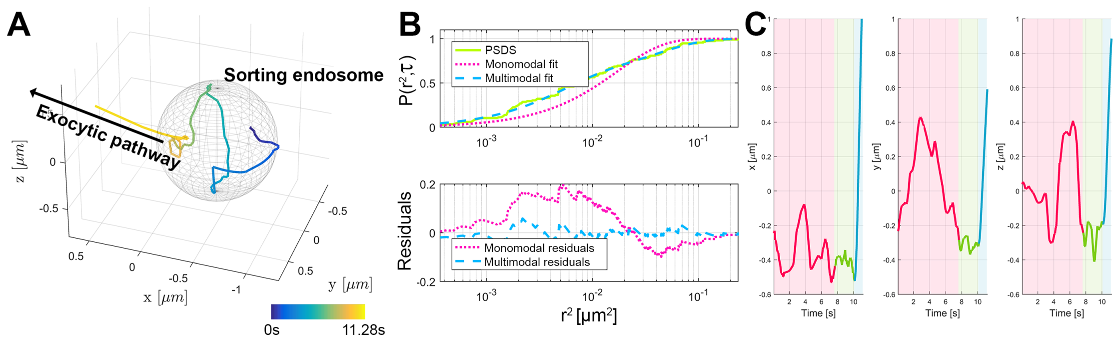

Figure 3.18: QD-αPSMA on the exocytic pathway is imaged using rMUM. (A) Segregation of QD-αPSMA from a sorting endosome is visualized. (B) The diffusive motion of (A) is analyzed using PDSD analysis. (C) QD-αPSMA on the sorting endosome diffuses along the inner leaflet of the endosomal membrane. A short constrained diffusive motion is identified followed by the directed motion of the exocytic pathway.

We also captured a recycling event of QD-αPSMA using rMUM. A QD-αPSMA segregated from the sorting endosome followed by directed diffusion towards the cell membrane (see Figure 3.18). Here, the rapid motion of the segregation event was analyzed using PDSD analysis (see Section 2.4.3 and Figure 3.18B). The time between the end of the diffusive motion and the beginning of directed motion of the exocytic pathway is short, i.e., within two seconds. The diffusion rate of QD-αPSMA during the segregation process measures 0.03 $\mu m^2/s$. The x, y and z coordinates of the trajectory are plotted over time (Figure 3.18C). Here we identified three distinct diffusive motions: directed diffusion, constrained diffusion and unconstrained diffusion. QD-αPSMA diffuses along the inner leaflet of the sorting endosome (pink). A short period of constrained diffusion appears (green) followed by directional motion (blue).

3.3.12 QD-αPSMA in multivesicular bodies and lysosomes

QD-αPSMA appears in multivesicular bodies (MVBs) and its diffusive behavior can change significantly (see Figure 3.19A). The QD-αPSMA moves along with the formation of an intraluminal vesicle (ILV) in the MVB. The QD-αPSMA moves to the center of the sorting endosome where it remains relatively stationary (see Figure 3.19D).

Using rMUM, we identified the QD-αPSMA at the sorting endosome during the later stages. The QD-αPSMA diffusion rate was changed when it moved toward the center of the sorting endosome (Figure 3.19C). We analyzed this trajectory, using PDSD analysis (see Section 2.4.3), and were able to identify two different diffusion dynamics of unconstrained diffusion (0.27 $\mu m^2/s$) at the inner leaflet followed by constrained diffusion (0.05 $\mu m^2/s$) at the center of the compartment (Figure 3.19B and D). A transmission electron micrograph of the QD-αPSMA in a MVB are localized on the outer membrane of the intraluminal vesicles (ILVs, black dots with arrows,

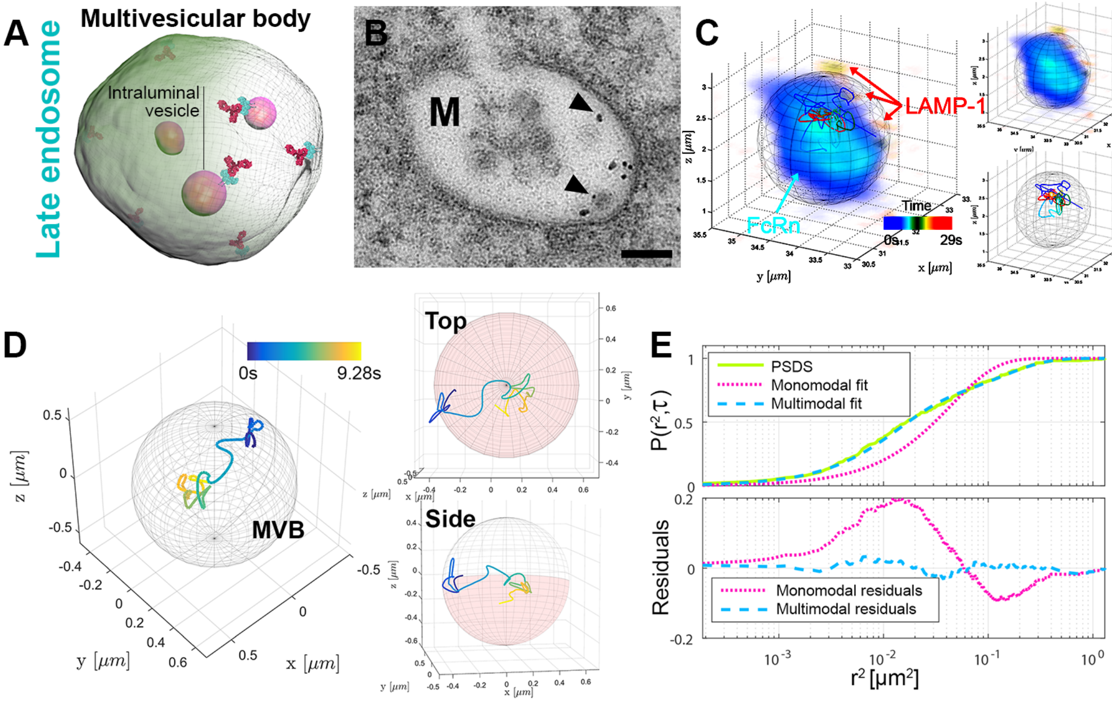

Figure 3.19: QD-αPSMA behavior in the late endosome. QD-αPSMA in late endosomes was imaged using rMUM. (A) An multivesicular body (MVB) structure is illustrated. Antibodies may be found at the intraluminal vesicles (ILVs). (B) A transmission electron micrograph of an MVB shows that QD-αPSMA is on the ILVs (black arrows) in 22Rv1 cells. (C) The diffusive motion of a QD-αPSMA on an endosomal compartment that is FcRn– and LAMP-1–positive is imaged using rMUM. (D) The moment when the QD-αPSMA enters the endosome from (C) is plotted. (E) The trajectory in (D) is analyzed using the PDSD analysis. Scale bar: (B) 100 nm.

see Figure 3.19B).

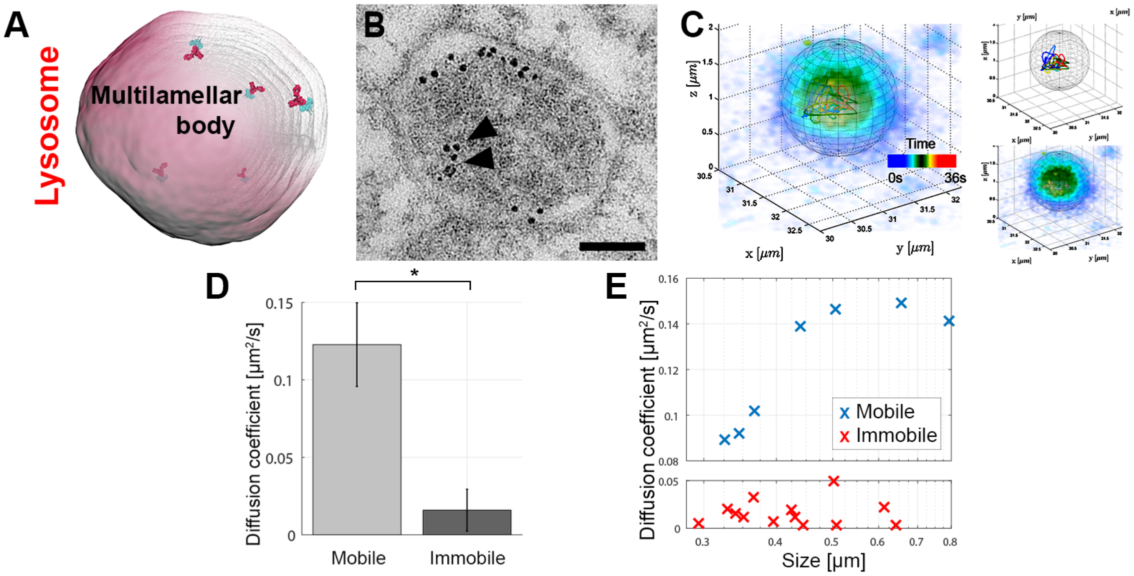

Figure 3.20: QD-αPSMA behavior in the lysosome. QD-αPSMA in lysosomes is imaged using rMUM. (A) Illustration of a lysosome depicted as a multilamellar body. (B) Transmission electron micrograph of a lysosome in a 22Rv1 cell shows QD-αPSMA in the electron dense matter, i.e. multilamellar body (black arrows). (C) The constrained diffusive motion of a QD-αPSMA in a LAMP-1–positive compartment was imaged using rMUM. (D) The diffusion rates of 20 QD-αPSMA trajectories in LAMP-1–positive compartments were measured, and their averages and standard deviations plotted. Mobile and immobile populations can be identified. There were significant differences between mobile and immobile populations (indicated by *; Welchs t–test, $p < 0.01$)(E) Diffusion rates identified in (D) plotted against the vesicle sizes in which the trajectories are found. Scale bar: (B) 100 nm.

Lysosomes have distinct internal structures such as multilamellar bodies. Such structures fill the lysosome completely (Figure 3.20). Figure 3.20C shows a transmission electron micrograph of a lysosome in which QD-αPSMA is shown to be embedded in the electron-dense lumens. Using rMUM, we visualize the QD-αPSMA dynamics in the lysosome while QD-αPSMA stays immobile inside the lysosome

(Figure 3.20B).

Here we analyzed 20 QD-αPSMA trajectories in the LAMP-1–positive compartments. Data were obtained from six independent experiments. Diffusion rates were measured as described in Section 2.4.1.2. Two groups (mobile and immobile) were identified with average diffusion rates of 0.12 ± 0.03 µm^2/s and 0.015 ± 0.013 µm^2/s, respectively (Figure 3.20D). The sizes of the LAMP-1–positive compartments were measured as 0.49 ± 0.17 µm and 0.43 ± 0.11 µm for the mobile and immobile group, respectively. There are statistically significant differences between the groups (Welchs t–test, $p < 0.01$). The diffusion rates of the QD-αPSMA trajectories are plotted against LAMP-1 compartment sizes (Figure 3.20E). The mobile group (blue) shows that the diffusion rates are in proportion to the size. We could not see such a relationship in the immobile group (red). Furthermore, the compartments of the mobile population are both LAMP-1– and FcRn–positive.

4. SUMMARY AND CONCLUSIONS

Single molecule microscopy is a powerful tool for exploring individual molecules within living specimens. A captured 3D single molecule trajectory, however, usually does not, by itself, fully explain the biological implications of the observed events. This is often due to a lack of information about the cellular context. Dynamics of individual molecules are only properly understood when information about the cellular context of these molecules is available. We have developed a novel multi-dimensional microscopy imaging modality called remote focusing-multifocal plane microscopy (rMUM). rMUM enables the observation of the dynamics of single molecules as well as information about the cellular compartments that they are associated with. Rapid movements of single molecules are imaged using the multifocal plane microscopy module, while at the same time, z-stack images of the surrounding cellular structures are obtained in three dimensions using the remote focusing technique. Analyses of these data using spatial and temporal registration and synchronization, rMUM can reveal the complex dynamics of individual proteins and molecules combined with their cellular context.

Prostate-specific membrane antigen (PSMA) is an important biomarker for prostate cancer therapeutics. Although PSMA has been recognized as an important target for therapeutic antibodies over the last decade, the trafficking behavior of PSMA-specific antibodies is not well understood. Here we use rMUM to investigate the trafficking of a PSMA-specific antibody in detail (see Section 3).

Using rMUM, the trafficking dynamics of the PSMA-specific antibodies were visualized conjugated to quantum dot. At the same time, the 3D cellular structures around the PSMA-specific antibody, such as cell membrane, clathrin coated pits,

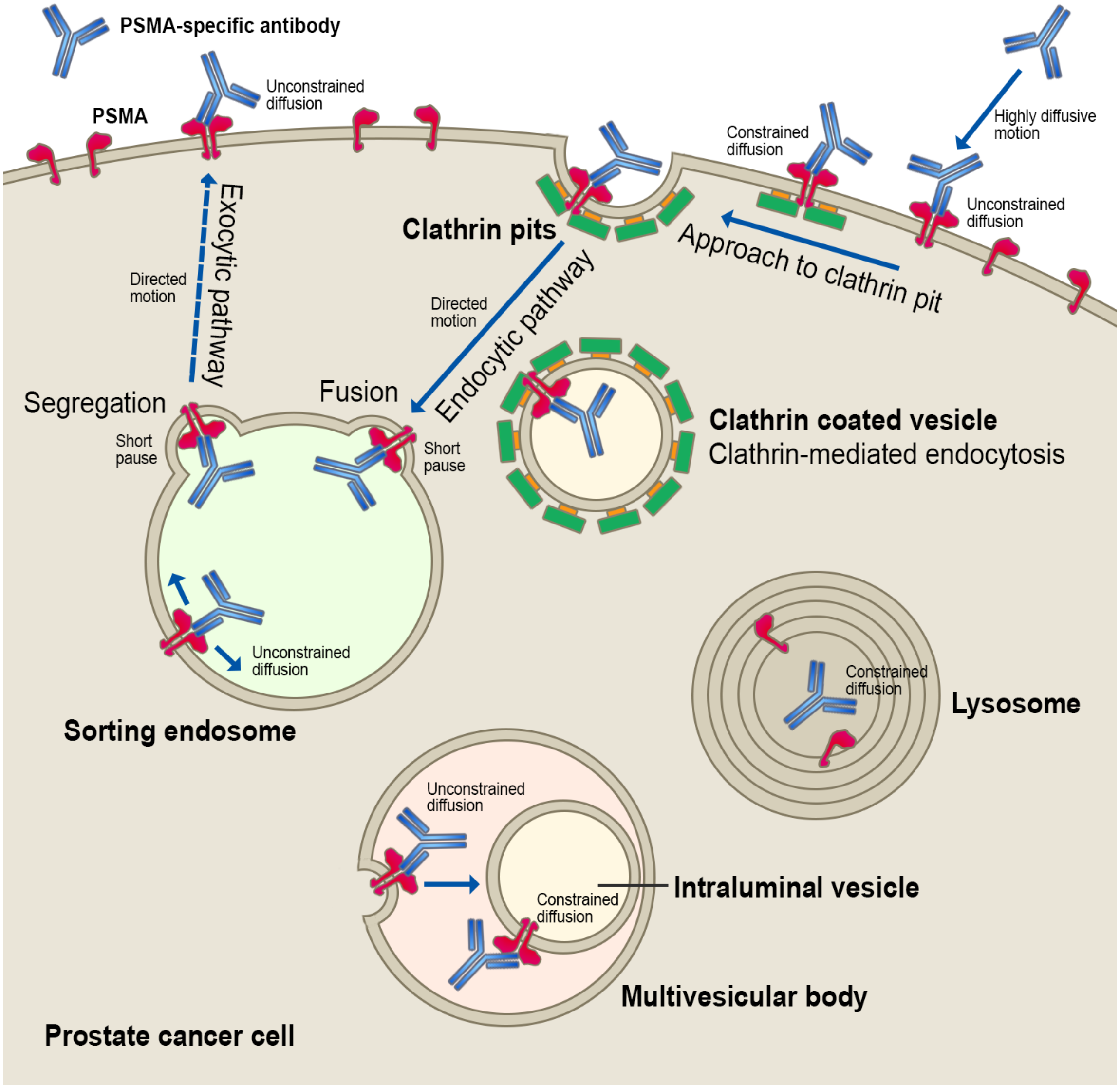

Figure 4.1: An illustration of PSMA trafficking with PSMA-specific antibody in prostate cancer cells.

sorting endosomes, late endosomes, and lysosomes, were imaged. This allows the analysis of PSMA-specific antibody trafficking in the context of the cellular environment in the prostate cancer cells. Figure 4.1 summarizes the trafficking behavior of the PSMA-specific antibody. First, the PSMA-specific antibody binds to PSMA on the cell surface (see Section 3.3.7), followed by unconstrained and constrained diffusive motions (see Section 3.3.8). The diffusive motion changes to constrained motion because of association with clathrin pits on the cell surface (see Section 3.3.10.1). The PSMA-specific antibody then undergoes clathrin-mediated endocytosis (see Section 3.3.10.2) and moves toward the sorting endosome with a highly directed motion (see Section 3.3.9). When it enters the sorting endosome, a short pause is observed, followed by the diffusion on the inner membrane leaflet of the sorting endosome (see Section 3.3.11). Here the diffusion rates are the similar to those of the unconstrained diffusion observed at the cell membrane. We also identified exocytic events in which the PSMA-specific antibody segregates the sorting endosome and moves toward the cell membrane with highly directed motion (see Figure 3.18). The average speed of the directed motion in the exocytic pathway is slower than that during the endocytic pathway. We were also able to visualize the internalization of the PSMA-specific antibody into an intraluminal vesicle within a multivesicular body (see Section 3.3.12). Finally, following entry into lysosomes, PSMA-specific antibody shows constrained diffusion (see Section 3.3.12).

REFERENCES

[1] Tomishige, M., Sako, Y. & Kusumi, A. Regulation mechanism of the lateral diffusion of band 3 in erythrocyte membranes by the membrane skeleton. *The Journal of Cell Biology* **142**, 989–1000 (1998).

[2] Smith, P. R., Morrison, I. E., Wilson, K. M., Fernández, N. & Cherry, R. J. Anomalous diffusion of major histocompatibility complex class I molecules on HeLa cells determined by single particle tracking. *Biophysical Journal* **76**, 3331–3344 (1999).

[3] Gelles, J., Schnapp, B. J. & Sheetz, M. P. Tracking kinesin-driven movements with nanometre-scale precision. *Nature* **331**, 450–453 (1988).

[4] Seisenberger, G., Ried, M. U., Endress, T., Büning, H., Hallek, M., Bräuchle, C., Endreß, T., Büning, H., Hallek, M. & Bräuchle, C. Real-time single-molecule imaging of the infection pathway of an adeno-associated virus. *Science* **294**, 1929–1932 (2001).

[5] Taguchi, H., Ueno, T., Tadakuma, H., Yoshida, M. & Funatsu, T. Single-molecule observation of protein-protein interactions in the chaperonin system. *Nature Biotechnology* **19**, 861–865 (2001).

[6] Iino, R., Koyama, I. & Kusumi, A. Single molecule imaging of green fluorescent proteins in living cells: e-cadherin forms oligomers on the free cell surface. *Biophysical Journal* **80**, 2667–2677 (2001).

[7] Yildiz, A., Forkey, J. N., McKinney, S. A., Ha, T., Goldman, Y. E. & Selvin, P. R. Myosin V walks hand-over-hand: single fluorophore imaging with 1.5-nm localization. *Science* **300**, 2061–2065 (2003).

[8] Moerner, W. E. & Kador, L. Optical detection and spectroscopy of single molecules in a solid. *Physical Review Letters* **62**, 2535–2538 (1989).

[9] Orrit, M. & Bernard, J. Single pentacene molecules detected by fluorescence excitation in a p -terphenyl crystal. *Physical Review Letters* **65**, 2716–2719 (1990).

[10] Betzig, E. & Chichester, R. J. Single molecules observed by near-field scanning optical microscopy. *Science* **262**, 1422–1425 (1993).

[11] Zlatanova, J. & Van Holde, K. Single-molecule biology: what is it and how does it work? *Molecular Cell* **24**, 317–329 (2006).

[12] Moerner, W. E. & Fromm, D. P. Methods of single-molecule fluorescence spectroscopy and microscopy. *Review of Scientific Instruments* **74**, 3597–3619 (2003).

[13] Chao, J., Ram, S., Ward, E. S. & Ober, R. J. Ultrahigh accuracy imaging modality for super-localization microscopy. *Nature Methods* **10**, 335–338 (2013).

[14] Ober, R. J., Ram, S. & Ward, E. S. Localization accuracy in single-molecule microscopy. *Biophysical Journal* **86**, 1185–1200 (2004).

[15] Ram, S., Ward, E. S. & Ober, R. J. Beyond Rayleigh's criterion: a resolution measure with application to single-molecule microscopy. *Proceedings of the National Academy of Sciences of the United States of America* **103**, 4457–4462 (2006).

[16] Shimomura, O., Johnson, F. H. & Saiga, Y. Extraction, purification and properties of aequorin, a bioluminescent protein from the luminous hydromedusan, Aequorea. *Journal of Cellular and Comparative Physiology* **59**, 223–239 (1962).

[17] Betzig, E., Patterson, G. H., Sougrat, R., Lindwasser, O. W., Olenych, S., Bonifacino, J. S., Davidson, M. W., Lippincott-Schwartz, J. & Hess, H. F. Imaging intracellular fluorescent proteins at nanometer resolution. *Science* **313**, 1642–1645 (2006).

[18] Lee, S. F. & Osborne, M. A. Brightening, blinking, bluing and bleaching in the life of a quantum dot: friend or foe? *ChemPhysChem* **10**, 2174–2191 (2009).

[19] Alivisatos, A. P., Gu, W. & Larabell, C. Quantum dots as cellular probes. *Annual Review of Biomedical Engineering* **7**, 55–76 (2005).

[20] Medintz, I. L., Uyeda, H. T., Goldman, E. R. & Mattoussi, H. Quantum dot bioconjugates for imaging, labelling and sensing. *Nature Materials* **4**, 435–446 (2005).

[21] Denvir, D. J. & Coates, C. G. Electron-multiplying CCD technology: application to ultrasensitive detection of biomolecules. *Proceedings of SPIE*, vol. 4626, 502–512 (2002).

[22] Denvir, D. J. & Conroy, E. Electron multiplying CCDs. *Proceedings of SPIE*, vol. 4877, 55–68 (2003).

[23] Saurabh, S., Maji, S. & Bruchez, M. P. Evaluation of sCMOS cameras for detection and localization of single Cy5 molecules. *Optics Express* **20**, 7338–7349 (2012).

[24] Axelrod, D. Total internal reflection fluorescence microscopy in cell biology. *Traffic* **2**, 764–774 (2001).

[25] Haustein, E. & Schwille, P. Single-molecule spectroscopic methods. *Current Opinion in Structural Biology* **14**, 531–540 (2004).

[26] Mashanov, G. I., Tacon, D., Knight, A. E., Peckham, M. & Molloy, J. E. Visualizing single molecules inside living cells using total internal reflection fluorescence microscopy. *Methods* **29**, 142–152 (2003).

[27] Ober, R. J., Martinez, C., Lai, X., Zhou, J. & Ward, E. S. Exocytosis of IgG as mediated by the receptor, FcRn: An analysis at the single-molecule level. *Proceedings of the National Academy of Sciences of the United States of America* **101**, 11076–11081 (2004).

[28] Enderlein, J. Positional and temporal accuracy of single molecule tracking. *Single Molecules* **1**, 225–230 (2000).

[29] Andersson, S. B. Tracking a single fluorescent molecule with a confocal microscope. *Applied Physics B* **80**, 809–816 (2005).

[30] Holtzer, L., Meckel, T. & Schmidt, T. Nanometric three-dimensional tracking of individual quantum dots in cells. *Applied Physics Letters* **90**, 053902 (2007).

[31] Kao, H. P. & Verkman, A. S. Tracking of single fluorescent particles in three dimensions: use of cylindrical optics to encode particle position. *Biophysical Journal* **67**, 1291–1300 (1994).

[32] Piestun, R., Schechner, Y. Y. & Shamir, J. Propagation-invariant wave fields with finite energy. *Journal of the Optical Society of America.* **17**, 294–303 (2000).

[33] Pavani, S. R. P., Thompson, M. A., Biteen, J. S., Lord, S. J., Liu, N., Twieg, R. J., Piestun, R. & Moerner, W. E. Three-dimensional, single-molecule fluorescence imaging beyond the diffraction limit by using a double-helix point spread function. *Proceedings of the National Academy of Sciences of the United States of America* **106**, 2995–2999 (2009).

[34] Ram, S., Prabhat, P., Chao, J., Ward, E. S. & Ober, R. J. High accuracy 3D quantum dot tracking with multifocal plane microscopy for the study of fast intracellular dynamics in live cells. *Biophysical Journal* **95**, 6025–6043 (2008).

[35] Ram, S., Kim, D., Ober, R. J. & Ward, E. S. 3D single molecule tracking with multifocal plane microscopy reveals rapid intercellular transferrin transport at epithelial cell barriers. *Biophysical Journal* **103**, 1594–1603 (2012).

[36] Gan, Z., Ram, S., Ober, R. J. & Ward, E. S. Using multifocal plane microscopy to reveal novel trafficking processes in the recycling pathway. *Journal of Cell Science* **126**, 1176–1188 (2013).

[37] Lidke, D. S., Nagy, P., Heintzmann, R., Arndt-Jovin, D. J., Post, J. N., Grecco, H. E., Jares-Erijman, E. a. & Jovin, T. M. Quantum dot ligands provide new insights into erbB/HER receptor-mediated signal transduction. *Nature Biotechnology* **22**, 198–203 (2004).

[38] Low-Nam, S. T., Lidke, K. A., Cutler, P. J., Roovers, R. C., van Bergen en Henegouwen, P. M. P., Wilson, B. S. & Lidke, D. S. ErbB1 dimerization is promoted by domain co-confinement and stabilized by ligand binding. *Nature Structural & Molecular Biology* **18**, 1244–1249 (2011).

[39] Cutler, P. J., Malik, M. D., Liu, S., Byars, J. M., Lidke, D. S. & Lidke, K. A. Multi-color quantum dot tracking using a high-speed hyperspectral line-scanning microscope. *PLOS ONE* **8**, 1–14 (2013).

[40] Ha, T., Enderle, T., Ogletree, D. F., Chemla, D. S., Selvin, P. R. & Weiss, S. Probing the interaction between two single molecules: fluorescence resonance energy transfer between a single donor and a single acceptor. *Proceedings of the National Academy of Sciences of the United States of America* **93**, 6264–6268 (1996).

[41] Roy, R., Hohng, S. & Ha, T. A practical guide to single-molecule FRET. *Nature Methods* **5**, 507–516 (2008).

[42] Ha, T. Single-molecule methods leap ahead. *Nature Methods* **11**, 1015–1018 (2014).

[43] Barve, A., Jin, W. & Cheng, K. Prostate cancer relevant antigens and enzymes for targeted drug delivery. *Journal of Controlled Release* **187**, 118–132 (2014).

[44] Wang, X., Ma, D., Olson, W. C. & Heston, W. D. W. In vitro and in vivo responses of advanced prostate tumors to PSMA ADC, an auristatin-conjugated antibody to prostate-specific membrane antigen. *Molecular Cancer Therapeutics* **10**, 1728–1739 (2011).

[45] Weiner, G. J. Building better monoclonal antibody-based therapeutics. *Nature Reviews Cancer* **15**, 361–370 (2015).

[46] Sievers, E. L. & Senter, P. D. Antibody-drug conjugates in cancer therapy. *Annual Review of Medicine* **64**, 15–29 (2013).

[47] Ritchie, M., Tchistiakova, L. & Scott, N. Implications of receptor-mediated endocytosis and intracellular trafficking dynamics in the development of antibody drug conjugates. *mAbs* **5**, 13–21 (2013).

[48] Sievers, E. L. & Senter, P. D. Antibody-drug conjugates in cancer therapy. *Annual Review of Medicine* **64**, 15–29 (2013).

[49] Kusumi, A., Tsunoyama, T. A., Hirosawa, K. M., Kasai, R. S. & Fujiwara, T. K. Tracking single molecules at work in living cells. *Nature Chemical Biology* **10**, 524–532 (2014).

[50] Grohmann, D., Werner, F. & Tinnefeld, P. Making connections–strategies for single molecule fluorescence biophysics. *Current Opinion in Chemical Biology* **17**, 691–698 (2013).

[51] Xia, T., Li, N. & Fang, X. Single-molecule fluorescence imaging in living cells. *Annual Review of Physical Chemistry* **64**, 459–480 (2012).

[52] Alberts, B. The cell as a collection of protein machines: preparing the next generation of molecular biologists. *Cell* **92**, 291–294 (1998).

[53] De Mey, J. R., Kessler, P., Dompierre, J., Cordelières, F. P., Dieterlen, A., Vonesch, J. & Sibarita, J. Fast 4D Microscopy. *Methods in Cell Biology* **85**, 83–112 (2008).

[54] Prabhat, P., Ram, S., Ward, E. S. & Ober, R. J. Simultaneous imaging of several focal planes in fluorescence microscopy for the study of cellular dynamics in 3D. *Proceedings of SPIE*, vol. 6090, 7 (2006).

[55] Prabhat, P., Gan, Z., Chao, J., Ram, S., Vaccaro, C., Gibbons, S., Ober, R. J. & Ward, E. S. Elucidation of intracellular recycling pathways leading to exocytosis of the Fc receptor, FcRn, by using multifocal plane microscopy. *Proceedings of the National Academy of Sciences of the United States of America* **104**, 5889–5894 (2007).

[56] Prabhat, P., Ram, S., Ward, E. S. & Ober, R. J. Simultaneous imaging of different focal planes in fluorescence microscopy for the study of cellular dynamics in three dimensions. *IEEE Transactions on Nanobioscience* **3**, 237–242 (2004).

[57] Smith, C. W., Botcherby, E. J. & Wilson, T. Resolution of oblique-plane images in sectioning microscopy. *Optics Express* **19**, 2662–2669 (2011).

[58] Botcherby, E. J., Juškaitis, R., Booth, M. J. & Wilson, T. An optical technique for remote focusing in microscopy. *Optics Communications* **281**, 880–887 (2008).

[59] Botcherby, E. J., Smith, C. W., Kohl, M. M., Débarre, D., Booth, M. J., Juškaitis, R., Paulsen, O. & Wilson, T. Aberration-free three-dimensional multiphoton imaging of neuronal activity at kHz rates. *Proceedings of the National Academy of Sciences of the United States of America* **109**, 2919–2924 (2012).

[60] Dunsby, C. Optically sectioned imaging by oblique plane microscopy. *Optics Express* **16**, 20306–20316 (2008).

[61] Ober, R. J., Martinez, C., Vaccaro, C., Zhou, J. & Ward, E. S. Visualizing the site and dynamics of IgG salvage by the MHC class I-related receptor, FcRn. *The Journal of Immunology* **172**, 2021–2029 (2004).

[62] Gan, Z., Ram, S., Vaccaro, C., Ober, R. J. & Ward, E. S. Analyses of the recycling receptor, FcRn, in live cells reveal novel pathways for lysosomal delivery. *Traffic* **10**, 600–614 (2009).

[63] Tahmasbi, A., Ram, S., Chao, J., Abraham, A. V., Tang, F. W., Sally Ward, E. & Ober, R. J. Designing the focal plane spacing for multifocal plane microscopy. *Optics Express* **22**, 16706–16721 (2014).

[64] Born, M., Wolf, E., Bhatia, A. B., Clemmow, P. C., Gabor, D., Stokes, A. R., Taylor, A. M., Wayman, P. A. & Wilcock, W. L. *Principles of optics.* (Cambridge University Press, 1999).

[65] Ram, S., Prabhat, P., Chao, J., Ward, E. S. & Ober, R. J. Three-dimensional single molecule tracking of quantum-dot labeled antibody molecules using mul-

tifocal plane microscopy. *International Society for Optics and Photonics*, vol. 7575, 7 (2010).

[66] Huang, F., Schwartz, S. L., Byars, J. M. & Lidke, K. a. Simultaneous multiple-emitter fitting for single molecule super-resolution imaging. *Biomedical Optics Express* **2**, 1377–1393 (2011).

[67] Cohen, E. A. K. & Ober, R. J. Analysis of point based image registration errors with applications in single molecule microscopy. *IEEE Transactions on Signal Processing* **61**, 6291–6306 (2013).

[68] Cohen, E. A. K., Kim, D. & Ober, R. J. Cramér-rao lower bound for point based image registration with heteroscedastic error model for application in single molecule microscopy. *IEEE Transactions on Medical Imaging* **34**, 2632–2644 (2015).

[69] Unser, M., Aldroubi, A. & Eden, M. B-spline signal processing. I. Theory. *IEEE Transactions on Signal Processing* **41**, 821–833 (1993).

[70] Biggs, D. S. C. & Andrews, M. Acceleration of iterative image restoration algorithms. *Applied Optics* **36**, 1766–1775 (1997).

[71] Richardson, M. Deconvolution of images and spectra. *Optical Engineering* **36**, 3224–3225 (1997).

[72] Bruce, M. A. & Butte, M. J. Real-time GPU-based 3D deconvolution. *Optics Express* **21**, 4766–4773 (2013).

[73] Saxton, M. J. & Jacobson, K. Single-particle tracking: applications to membrane dynamics. *Annual Review of Biophysics and Biomolecular Structure* **26**, 373–399 (1997).

[74] Jaqaman, K., Loerke, D., Mettlen, M., Kuwata, H., Grinstein, S., Schmid, S. L. & Danuser, G. Robust single-particle tracking in live-cell time-lapse sequences. *Nature Methods* **5**, 695–702 (2008).

[75] Munkres, J. Algorithms for the assignment and transportation problems. *Journal of the Society for Industrial and Applied Mathematics* **5**, 32–38 (1957).

[76] Kusumi, A., Sako, Y. & Yamamoto, M. Confined lateral diffusion of membrane receptors as studied by single particle tracking (nanovid microscopy). Effects of calcium-induced differentiation in cultured epithelial cells. *Biophysical Journal* **65**, 2021–2040 (1993).

[77] Wang, Y. M., Austin, R. H. & Cox, E. C. Single molecule measurements of repressor protein 1D diffusion on DNA. *Physical Review Letters* **97**, 048302 (2006).

[78] Ernst, D. & Köhler, J. Measuring a diffusion coefficient by single-particle tracking: statistical analysis of experimental mean squared displacement curves. *Physical Chemistry Chemical Physics* **15**, 845–849 (2013).

[79] Schütz, G., Schindler, H. & Schmidt, T. Single-molecule microscopy on model membranes reveals anomalous diffusion. *Biophysical Journal* **73**, 1073–1080 (1997).

[80] Pinaud, F., Michalet, X., Iyer, G., Margeat, E., Moore, H.-P. & Weiss, S. Dynamic partitioning of a glycosyl-phosphatidylinositol-anchored protein in glycosphingolipid-rich microdomains imaged by single-quantum dot tracking. *Traffic* **10**, 691–712 (2009).

[81] Chao, J., Lee, T., Ward, E. S. & Ober, R. J. Fluorescent microspheres as point sources: a localization study. *PLOS ONE* **10**, 1–29 (2015).

[82] Atherton, T. & Kerbyson, D. Size invariant circle detection. *Image and Vision Computing* **17**, 795–803 (1999).

[83] Arthur, D. & Vassilvitskii, S. K-means++: the advantages of careful seeding. *Proceedings of the Eighteenth Annual ACM-SIAM Symposium on Discrete Algorithms* **8**, 1027–1035 (2007).

[84] Tibshirani, R., Walther, G. & Hastie, T. Estimating the number of clusters in a data set via the gap statistic. *Journal of the Royal Statistical Society: Series B* **63**, 411–423 (2001).

[85] Levoy, M. Display of surfaces from volume data. *IEEE Computer Graphics and Applications* **8**, 29–37 (1988).

[86] Rosin, P. L. Unimodal thresholding. *Pattern Recognition* **34**, 2083–2096 (2001).

[87] Drebin, R. A., Carpenter, L. & Hanrahan, P. Volume rendering. *ACM Siggraph Computer Graphics* **22**, 65–74 (1988).

[88] Chang, S. S. Overview of prostate-specific membrane antigen. *Reviews in Urology* **6**, 13–18 (2004).

[89] Rajasekaran, A. K., Anilkumar, G. & Christiansen, J. J. Is prostate-specific membrane antigen a multifunctional protein? *American Journal of Physiology. Cell Physiology* **288**, 975–981 (2005).

[90] Ghosh, A. & Heston, W. D. W. Tumor target prostate specific membrane antigen (PSMA) and its regulation in prostate cancer. *Journal of Cellular Biochemistry* **91**, 528–539 (2004).

[91] Campbell, R. E., Campbell, R. E., Tour, O., Tour, O., Palmer, A. E., Palmer, A. E., Steinbach, P. a., Steinbach, P. a., Baird, G. S., Baird, G. S., Zacharias, D. a., Zacharias, D. a., Tsien, R. Y. & Tsien, R. Y. A monomeric red fluorescent

protein. *Proceedings of the National Academy of Sciences of the United States of America* **99**, 7877–7882 (2002).

[92] Ram, S., Chao, J., Prabhat, P., Ward, E. S. & Ober, R. J. A novel approach to determining the three-dimensional location of microscopic objects with applications to 3D particle tracking. *Proceedings of SPIE*, vol. 6443, 7 (2007).

[93] Lai, X., Lin, Z., Ward, E. S. & Ober, R. J. Noise suppression of point spread functions and its influence on deconvolution of three-dimensional fluorescence microscopy image sets. *Journal of Microscopy* **217**, 93–108 (2005).

[94] Firan, M., Bawdon, R., Radu, C., Ober, R. J., Eaken, D., Antohe, F., Ghetie, V. & Ward, E. S. The MHC class I-related receptor, FcRn, plays an essential role in the maternofetal transfer of gamma-globulin in humans. *International Immunology* **13**, 993–1002 (2001).

[95] Chao, J., Ward, E. S. & Ober, R. J. A software framework for the analysis of complex microscopy image data. *IEEE Transactions on Information Technology in Biomedicine* **14**, 1075–1087 (2010).

[96] Ward, E. S., Martinez, C., Vaccaro, C., Zhou, J., Tang, Q. & Ober, R. J. From sorting endosomes to exocytosis: association of Rab4 and Rab11 GTPases with the Fc receptor, FcRn, during recycling. *Molecular Biology of the Cell* **16**, 2028–2038 (2005).

[97] Gruenberg, J. & Van der Goot, F. G. Mechanisms of pathogen entry through the endosomal compartments. *Nature Reviews Molecular Cell Biology* **7**, 495–504 (2006).

[98] Qiao, S. W., Kobayashi, K., Johansen, F. E., Sollid, L. M., Andersen, J. T., Milford, E., Roopenian, D. C., Lencer, W. I. & Blumberg, R. S. Dependence

of antibody-mediated presentation of antigen on FcRn. *Proceedings of the National Academy of Sciences of the United States of America* **105**, 9337–9342 (2008).

[99] Vanlandingham, P. A. & Ceresa, B. P. Rab7 regulates late endocytic trafficking downstream of multivesicular body biogenesis and cargo sequestration. *The Journal of Biological Chemistry* **284**, 12110–12124 (2009).

[100] Mastro, A. M., Babich, M. A., Taylor, W. D. & Keith, A. D. Diffusion of a small molecule in the cytoplasm of mammalian cells. *Proceedings of the National Academy of Sciences of the United States of America* **81**, 3414–3418 (1984).

[101] Ambrose, E. J. A surface contact microscope for the study of cell movements. *Nature* **178**, 1194–1194 (1956).

[102] Douglass, A. D. & Vale, R. D. Single-molecule microscopy reveals plasma membrane microdomains created by protein-protein networks that exclude or trap signaling molecules in T cells. *Cell* **121**, 937–950 (2005).

[103] Maxfield, F. R. & McGraw, T. E. Endocytic recycling. *Nature Reviews Molecular Cell Biology* **5**, 121–132 (2004).

[104] Le Roy, C. & Wrana, J. L. Clathrin- and non-clathrin-mediated endocytic regulation of cell signalling. *Nature Reviews Molecular Cell Biology* **6**, 112–126 (2005).

[105] Edeling, M. A., Smith, C. & Owen, D. Life of a clathrin coat: insights from clathrin and AP structures. *Nature Reviews Molecular Cell Biology* **7**, 32–44 (2006).

[106] Boettner, D. R., Chi, R. J. & Lemmon, S. K. Lessons from yeast for clathrin-mediated endocytosis. *Nature Cell Biology* **14**, 2–10 (2012).

[107] Waterman, H. & Yarden, Y. Molecular mechanisms underlying endocytosis and sorting of ErbB receptor tyrosine kinases. *FEBS letters* **490**, 142–152 (2001).

[108] Hicke, L. & Dunn, R. Regulation of membrane protein transport by ubiquitin and ubiquitin-binding proteins. *Annual Review of Cell and Developmental Biology* **19**, 141–172 (2003).

[109] Doherty, G. J. & McMahon, H. T. Mechanisms of endocytosis. *Annual Review of Biochemistry* **78**, 857–902 (2009).

[110] Li, Y., Shang, L. & Nienhaus, G. U. Super-resolution imaging-based single particle tracking reveals dynamics of nanoparticle internalization by live cells. *Nanoscale* **8**, 7423–7429 (2016).

[111] Shang, L., Nienhaus, K. & Nienhaus, G. U. Engineered nanoparticles interacting with cells: size matters. *Journal of Nanobiotechnology* **12**, 1–11 (2014).

[112] Rajasekaran, S. A., Anilkumar, G., Oshima, E., Bowie, J. U., Liu, H., Heston, W., Bander, N. H. & Rajasekaran, A. K. A novel cytoplasmic tail MXXXL motif mediates the internalization of prostate-specific membrane antigen. *Molecular Biology of the Cell* **14**, 4835–4845 (2003).

[113] Schulke, N., Varlamova, O. A., Donovan, G. P., Ma, D., Gardner, J. P., Morrissey, D. M., Arrigale, R. R., Zhan, C., Chodera, A. J., Surowitz, K. G., Maddon, P. J., Heston, W. D. W. & Olson, W. C. The homodimer of prostate-specific membrane antigen is a functional target for cancer therapy. *Proceedings of the*

National Academy of Sciences of the United States of America **100**, 12590–12595 (2003).

[114] Liu, J., Kopecková, P., Bühler, P., Wolf, P., Pan, H., Bauer, H., Elsässer-Beile, U. & Kopecek, J. Biorecognition and subcellular trafficking of HPMA copolymer-anti-PSMA antibody conjugates by prostate cancer cells. *Molecular Pharmaceutics* **6**, 959–970 (2009).

[115] Rajasekaran, S. A., Christiansen, J. J., Schmid, I., Oshima, E., Ryazantsev, S., Sakamoto, K., Weinstein, J., Rao, N. P. & Rajasekaran, A. K. Prostate-specific membrane antigen associates with anaphase-promoting complex and induces chromosomal instability. *Molecular Cancer Therapeutics* **7**, 2142–2151 (2008).